NASA CR-54147
4137-6018-SU-000

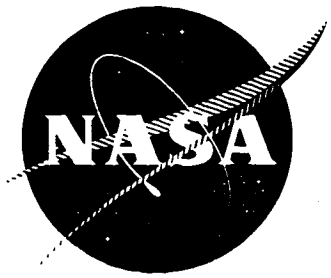

INVESTIGATION OF ION BEAM DIAGNOSTICS

by

J. M. Sellen, Jr., and Robert F. Kemp

prepared for

NATIONAL AERONAUTICS AND SPACE ADMINISTRATION

CONTRACT NAS 3-4114

TRW SPACE TECHNOLOGY LABORATORIES
THOMPSON RAMO WOOLDRIDGE INC.

NASA CR-54147
4137-6018-SU-000

FINAL REPORT

INVESTIGATION OF ION BEAM DIAGNOSTICS

by

J. M. Sellen, Jr., and Robert F. Kemp

prepared for

NATIONAL AERONAUTICS AND SPACE ADMINISTRATION

April 15, 1965

CONTRACT NAS 3-4114

Technical Management
NASA Lewis Research Center
Cleveland, Ohio 44135
Electric Propulsion Office
Sanford Jones
Ross H. Hieber

PHYSICAL ELECTRONICS LABORATORY
Physical Research Division

TRW Space Technology Laboratories
Thompson Ramo Wooldridge Inc.
One Space Park, Redondo Beach, California

TABLE OF CONTENTS

SECTION I.

INTRODUCTION

INVESTIGATIONS OF ION BEAM DIAGNOSTICS

by J. M. Sellen, Jr., and Robert F. Kemp
TRW Space Technology Laboratories

I. INTRODUCTION

The results of the research program conducted under Contract NAS3-4114, Investigation of Ion Beam Diagnostics, are presented in the four technical documents in the sections which follow. These manuscripts describe the studies of plasma wind tunnel techniques, the experiments on the in-line mercury optical resonance probe, the analysis of flight test data from the SERT-I spacecraft, and the sensitivity tests of the flight model E-field meter from that spacecraft.

The first manuscript, "Generation and Characteristics of Plasma Wind Tunnel Streams," given in Section II.A., describes the adaptation of the Kaufman ion source to the formation of plasma streams for plasma wind tunnel studies. The gases used in the ion source include H_2, O_2, N_2, He, Ne, A, and CO_2. The densities and streaming velocities of these plasma beams simulate those conditions which a spacecraft would encounter in moving through the earth's ionosphere. The methods of generating both the "longitudinal" and "transverse" ion thermal velocity components have been developed, and are described in that manuscript. This description of the plasma wind tunnel studies has been accepted for publication in the AIAA Journal and will supplement the earlier work, "Plasma-Vehicle Interaction in a Plasma Stream," AIAA Journal 2, 1032, (1963), which was supported by Lewis Research Center under Contract NAS8-1560.

The discussion of the in-line mercury optical resonance probe is given in Section II.B. This work continues the earlier studies described in "Ion Beam Neutral Component Determination by Resonance Radiation Absorption" AIAA Journal 3, 263, (February 1965),

(also supported under Contract NAS8-1560). This later effort extends the optical probe technique to an in-line geometry which provides a reduction in the optical path length and in the number of optical surfaces relative to that geometry utilized earlier. The emphasis in the program effort was upon stability in the probe's operation, the precision control of the various components in the probe and the elimination of background optical signals from the discharge region in the ion engine. The instrument which resulted from this program effort provided a sensitive and reliable laboratory measurement of propellant utilization.

The remaining portions of the program effort are presented in Sections II.C. and II.D. Section II.C. contains the manuscript, "Environmental Effects on Laboratory and In-Flight Performance of Neutralization Systems," which was presented at the 2nd Aerospace Sciences Meeting of the AIAA. This study examines both laboratory and space flight test data on the performance of the neutralization system of the SERT-I mercury electron bombardment engine. The laboratory experiments on the beam neutralization system were conducted at TRW/STL under an earlier program in collaboration with NASA Lewis Research Center (NAS3-2199). The flight test data examined was provided by the SERT-I space test of the electron bombardment engine. The conclusion in the discussion in Section II.C. is that effective neutralization of ion thrust beams has been demonstrated in both controlled laboratory experiments and in the SERT-I test. The discussion further concludes that the interpretation of vehicle potential from the surface field strength E-field meter requires significant corrections because of the ambient plasma in the near neighborhood of the earth.

In an attempt to arrive at quantitative measurements of the magnitudes and nature of these corrections, a series of

tests was conducted with the SERT-I rotating-vane E-meter. These are described in the concluding section, II.D. The tests included the response of the meter to both steady-state and time-varying electric fields, to ultraviolet radiation and to dilute streaming plasmas. The response of the E-field meter to these plasma streams is corroborative evidence that the ambient plasmas in the ionosphere possessed sufficient density to have provided the strong, spin-dependent signals which were recorded from the E-meter during the flight of the SERT-I spacecraft. The tests for the sensitivity of the E-meter to ultraviolet radiation could not be interpreted rigorously in terms of the possible behavior of the instrument during the flight. While the E-meter did provide a response to the incident laboratory UV radiation, this radiation is not a match to the solar ultraviolet, particularly in the high energy, short wavelength portion of the solar spectrum.

In summary, the manuscripts in the following sections describe the results of the research program conducted under Contract NAS3-4114. As a result of that program, the generation and diagnostic techniques for plasma wind tunnel streams have been advanced, the improved effectiveness of the in-line optical probe for measurements of propellant utilization has been demonstrated, the performance of neutralization systems and the environmental effects upon the performance of these systems and associated diagnostic instruments have been examined, and the sensitivity of the surface field strength meters to various possible environmental effects has been determined. These several aspects of the program constitute an advance in the technology of ion thrustor systems and in the diagnostic tools by which the performance of these thrustor systems may be determined.

SECTION II.

TECHNICAL MANUSCRIPTS AND PUBLISHED PAPERS

SECTION II.A.

GENERATION AND CHARACTERISTICS OF PLASMA WIND TUNNEL STREAMS

4137-6012-KU-000

GENERATION AND CHARACTERISTICS OF PLASMA WIND TUNNEL STREAMS*

by

David F. Hall, Robert F. Kemp

and J. M. Sellen, Jr.

*Submitted to the AIAA Journal

PHYSICAL ELECTRONICS LABORATORY
Physical Research Division

TRW Space Technology Laboratories
Thompson Ramo Wooldridge Inc.
One Space Park, Redondo Beach, California

GENERATION AND CHARACTERISTICS OF PLASMA WIND TUNNEL STREAMS†

by

David F. Hall*, Robert F. Kemp*, and J. M. Sellen, Jr.*

TRW Space Technology Laboratories, Redondo Beach, California

ABSTRACT

The plasma wind tunnel permits the laboratory study of the interaction of material bodies moving through a dilute plasma, such as the ionosphere, and the laboratory calibration of spacecraft plasma diagnostic instrumentation. Plasma streams, with uniform density cross sections ~ 30 cm diameter of H_2, He, N_2, O_2, Ne, A, CO_2, and Cs, and some mixtures thereof, have been produced at 1.6 m from an 11 cm electron bombardment and a 2.5 cm contact ion source. Except for H_2 and He, velocities and densities appropriate for simulation of satellite orbiting below the heliosphere ($\leq$ 8 Km/sec, $\leq 10^6$ ions/cm^3) are included in their range of operation.

The ion velocity spread in the longitudinal direction apparent from a satellite due to the ion thermal motion has been simulated through the variation of plasma source accelerating potential. Simulation of transverse velocity components due to thermal motion has been achieved through the use of electrostatic scattering fields imposed on the stream.

---

†This work supported by National Aeronautics and Space Administration, Lewis Research Center (Contract NAS3-4114).

*Member of the Technical Staff. Member of AIAA.

NOMENCLATURE

ρ = plasma density, ions/cm^3

v_+ = ion velocity, Km/sec

j_+ = ion current density, amp/cm^2

V = potential, V

$\tilde{V}$ = maximum value of perturbation potential, V

q = electric charge, coul

ΔW = width of energy distribution, eV

N = total number of particles in system

k = Boltzmann's constant, 1.38×10^{-23} joules/°K

T = Kelvin temperature

M = mass, Kg

r = radius, radial distance, cm

Λ = klystron bunching length, m

L = axial length of the divergence analyzer, cm

ℓ = source to object distance, m

Subscripts

+ = ion

e = electron

s = spacecraft

p = plasma

pr = probe

o = average beam value

1 = perturbation value

is = ion source

th = average thermal

I. INTRODUCTION

A previous paper[1] has introduced the concept of simulating spacecraft travel through ionized media by directing a low density streaming plasma toward a stationary vehicle or model thereof. This paper will detail later techniques and refinements which enable a rather complete simulation of spacecraft travel through the ionosphere and the calibration of instruments on board for the diagnosis of the space plasma.

The facility used for these studies is pictured in Figure 1. One of two plasma sources is fitted in the end door of the 4' x 8' vacuum chamber. The chamber is pumped by a 3000 liter/sec oil diffusion pump to a background pressure of $\sim 2 \times 10^{-6}$ Torr, corresponding to a neutral density of 6×10^{10} particles/cm^3 and a mean free path of the order of 10^3 m. In the far end of the tank is a model vehicle and various beam diagnostic devices.

Section II of this paper briefly reviews the constituents of the ionosphere and typical orbital velocities to indicate the required characteristics of the plasma beams which simulate satellite travel through the ionosphere. Section III describes the diagnostic instruments and techniques used in assuring that the synthesized beams have these properties. Section IV discusses the ion sources and the beams which have been produced to date. Some refinements of simulation are presented in Section V.

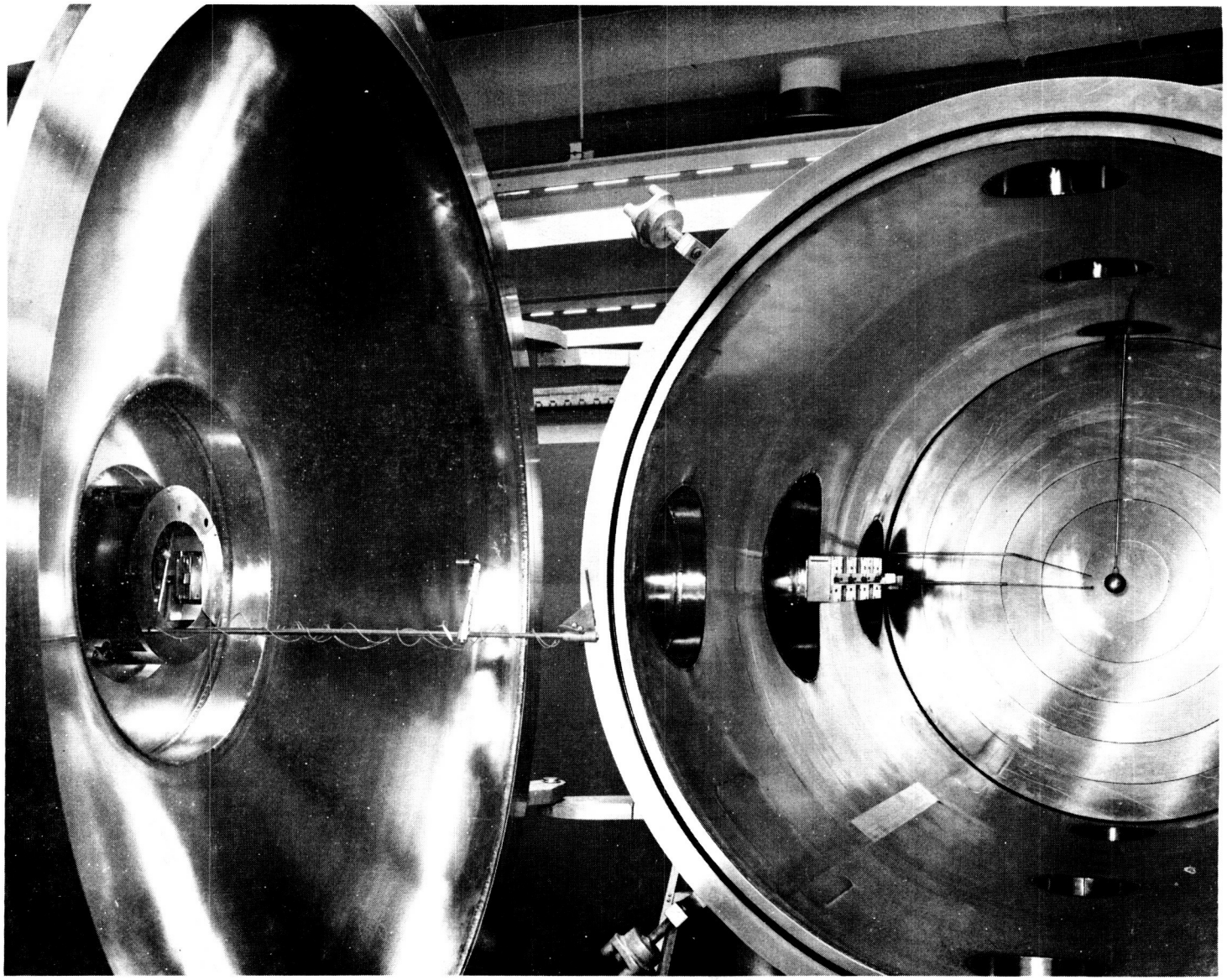

Figure 1. Four-ft by eight-ft vacuum enclosure used for plasma wind tunnel studies.

II. THE IONOSPHERE AND ORBITAL VELOCITIES

Probably the most characteristic feature of the ionosphere is its fluctuations. The sunspot cycle, the latitude, and the time of day are among the independent variables which have been identified. It is possible, however, to indicate typical magnitudes of mass number, ion density, and ion temperature which occur[2,3,4,5] and these, plus typical orbital velocities, will indicate the properties required of a plasma beam which is to simulate vehicle motion through the ionosphere.

For convenience, data obtained from References 2 and 4 are reproduced in Table I. Values of ion concentration, ρ, listed represent the approximate maxima which occur for geomagnetic latitudes near 35 degrees. (In simulation, it is always easier to produce lower values of ρ.) Temperatures used to calculate average ion thermal velocity $v_+|_{th}$ are those of neutrals in the region. Values of v_s, the spacecraft velocity, are those for circular orbits. Higher velocities can be attained by elliptical orbits and space probes, and lower velocities obtain during portions of probe shots which return to the earth.

Values of $v_e|_{th}$, the average electron thermal velocity exceed 100 Km/sec and therefore will appear quite random to all orbiting spacecraft.

In general, then, simulation will require ions of mass numbers between 14 and 32, ion densities not exceeding

Table I. Typical Values of Ionosphere Variables Important to Simulation

Altitude (Km)	Designation	Constituents	ρ_{max} (ions/cm^3)	$v_+\|_{th}$ Km/sec	v_s Km/sec
60-85	D	NO^+(?)	1×10^3	0.4	7.9
85-140	E	O_2^+,NO^+	1.5×10^5	0.4	7.9
140-200	F_1	NO^+,O_2^+,O^+	3×10^5	0.9	7.8
200-1200	F_2	O^+,N^+	1.5×10^6	1.4	7.5
1200-3400	Heliosphere	He^+	1×10^4	3.7	7.3-6.4
3400-	Protonosphere	H^+	1×10^3	5.6	6.4-

3×10^6 ions/cm^3, and directed velocities between 7 and 8 Km/sec. Electron velocities should be random and at least an order of magnitude greater. Simulation of the ion velocity distribution encountered during circular orbiting in the upper heliosphere and the protonosphere will not be appropriate with the plasma wind tunnel because at that elevation, $v_+|_{th} \simeq v_s$, i.e., the ion motion with respect to the vehicle is not well ordered.

III. MEASUREMENT OF BEAM CHARACTERISTICS

Some of the elements of a typical plasma wind tunnel are depicted in the sketch, Figure 2 (cf. Figure 1). Shown there, in addition to the plasma source and the vehicle or instrument under test, are a number of diagnostic devices for

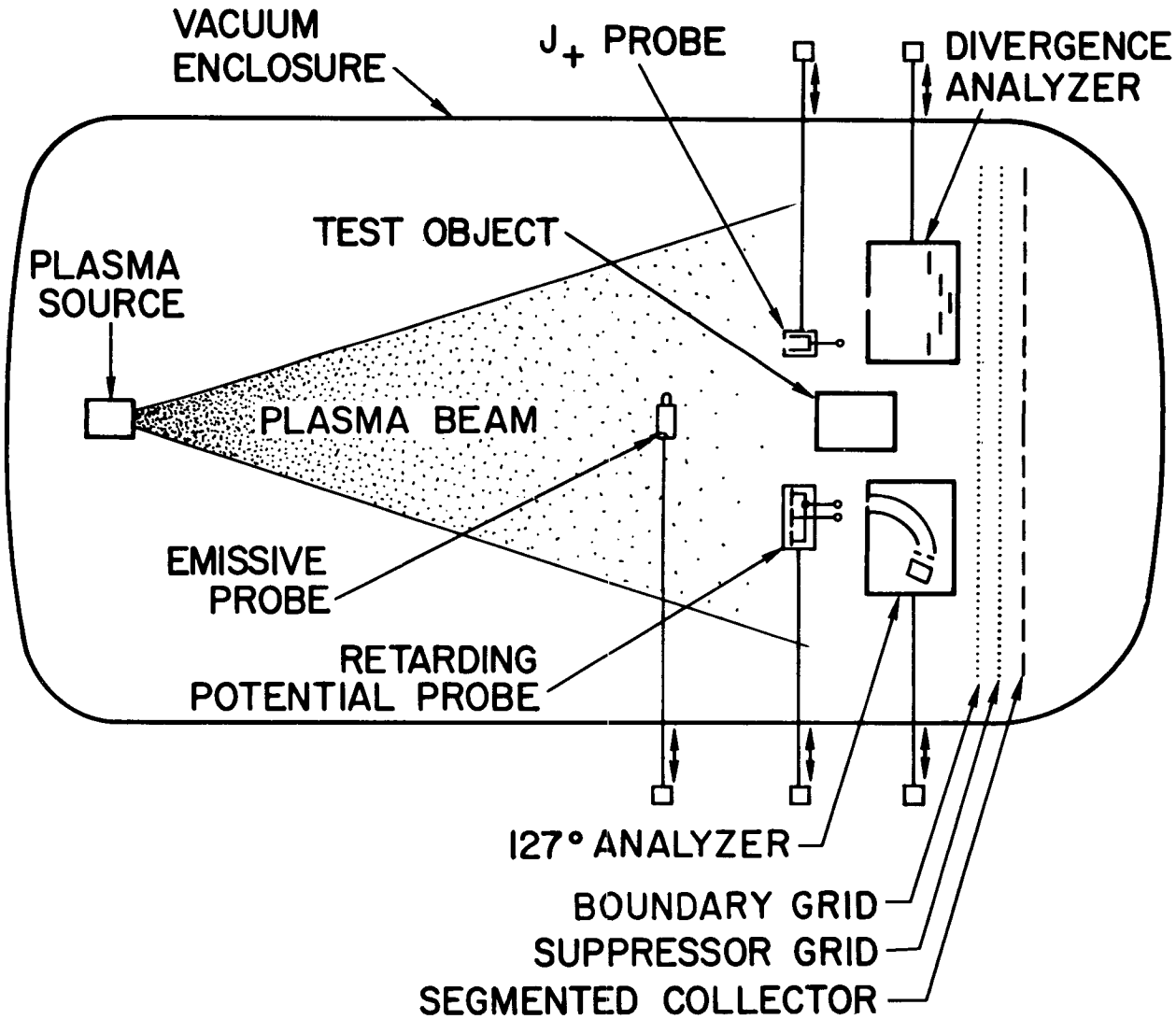

Figure 2. Schematic diagram of the plasma wind tunnel. Diagnostic instruments and object under test may be moved from outside the vacuum enclosure.

determining the measurable characteristics of plasma beams. These beams are well neutralized and their plasma potentials, V_p, are typically a few volts positive with respect to ground.[6,7,8]

A. Beam Current, Current Density

Total beam current at the farthest downstream location may be determined from the sum of ion currents arriving at the various elements of the collector. Segmentation allows for rough measurements of radial distribution of beam current. The accuracy of the measurement is improved by placing two grids in front of the collector. The boundary grid, maintained at the potential of the vacuum enclosure (ground), electrically shields the suppressor grid which is sufficiently negative to reflect both plasma electrons and secondaries. When beam current measurements are not being made, the collector and its grids are connected only to each other, so that they assume the "floating potential," which corresponds to collection of equal ion and electron currents from the beam. Thus, they introduce a plane unipotential surface into the beam, but otherwise offer a minimum electrical interference.

Detailed mapping of beam current density is done with "Faraday-cup" probes (abbreviated j_+ probes), ranging in size from 1/16" to several inches in diameter, which can be moved about within the beam. The small probes consist of two concentric cylinders, the outer containing a gridded entrance aperture biased to reject electrons, and an inner collection

cup.[7] Shown along the vacuum tank wall in Figure 1 is a boom on which are mounted four similar but large and rectangular j_+ probes. This boom may be swung into the beam so that the end probe is on the tank axis. These probes have equal areas and are used to quickly ascertain the uniformity of number density, ρ, through the relation $\rho = j_+/v_+$.

B. Plasma Potential

It is important to be able to determine V_p, the space potential within the plasma, because ion velocity is related to the difference between V_p and the ion source potential, V_+. Also, the difference between V_p and the spacecraft potential, V_s, is a controlling factor in the electrical plasma-vehicle interaction.

Indicators of V_p include the potentials of immersed neutralizer, floating collector, floating emissive probes, and Langmuir probe data. Precise measurements of local values are obtained from the emission characteristic of the emissive probe.[1,6]

In general, outside the "injection region" of the neutralizer, along any radius V_p is nearly constant in the central, uniform-density region of the beam, and decreases uniformly from there out to the chamber walls. Along the axis, it gradually decreases from the source to the floating collector.[7]

C. Electron Temperature in the Plasma Beam

The kinetic energy distribution of neutralizing electrons is Maxwellian for well-neutralized beams, with a characteristic temperature, T_e, approximately equal to that of the electron emitter. In the absence of magnetic fields, T_e in downstream portions of the beam may drop well below this value. On the other hand, T_e may be increased by injecting the electrons through an abnormally large potential, as is done with neutralizers withdrawn from the beam.[9]

The collection characteristic of 1 to 5 mil tungsten wire probes provides a measure of T_e. These Langmuir probes should have a constant work function, especially if T_e is low. Therefore, they are held just below thermionic emission temperature. Experiments demonstrate that corrections for the directed motion of the plasma to standard data analysis are not required to obtain the desired accuracy.

D. Ion Velocity

Measurements of v_+ demonstrate that the correct average velocity and velocity profile have been achieved for simulation. They also identify the major particle species in the beam.

1. Ion Time of Flight

The ion source potential has a 60 cps rectangular waveform. Current collected by a large downstream j_+ probe provides a time-of-flight (q/M_+) spectrometer signal. From it,

for example, continuous information of the relative abundances of N^+ and N_2^+ in a nitrogen plasma beam is available. Resolution of this mass measurement is complicated by the rise time of V_+, by dispersion in the plasma beam front, by displacement currents from the approaching plasma front (reduced when a j_+ grid is used), by uncertainty in V_p, and by noise signals.[8] Nevertheless, agreement within 5 percent is common between time-of-flight measurements and calculations from net acceleration potential corrected for rise time.

2. Retarding Potential Analyzer

The large Faraday-cup type probe used for retarding-potential measurements of ion energy indicated in Figure 2 is detailed in Figure 3. It has a guard ring around the collector and a grid over the entrance aperture maintained sufficiently negative to reflect electrons. The collector and guard ring are swept through a range of positive voltages, and collected ion current is plotted against this potential. The derivative of this function is the net acceleration potential

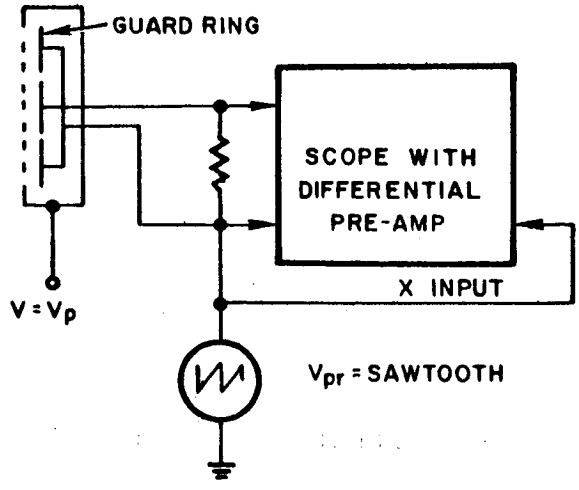

Figure 3. Detail of retarding potential measurement

spectrum. Again particles of different q/M_+ are not distinguished. This instrument is only used for low density beams as it is less accurate and convenient than the following one.

3. 127° Electrostatic Analyzer

Figure 4 is a diagram of a 127° electrostatic analyzer used to measure ion velocity distributions. It also measures the net acceleration potential of a charged particle, and cannot distinguish between charge-to-mass ratios. Unlike the retarding-potential probe, its direct measurement is useful where the ion energy is a rapidly varying function of time. The small apertures necessary to produce 5 percent energy resolution, result in small detected currents. Consequently, a driven-shield cathode follower at the ion cup reduces impedance and maximizes the frequency response of the output. Details of an experiment using the 127° analyzer to study time-varying ion velocity distributions are discussed in Section V.C.

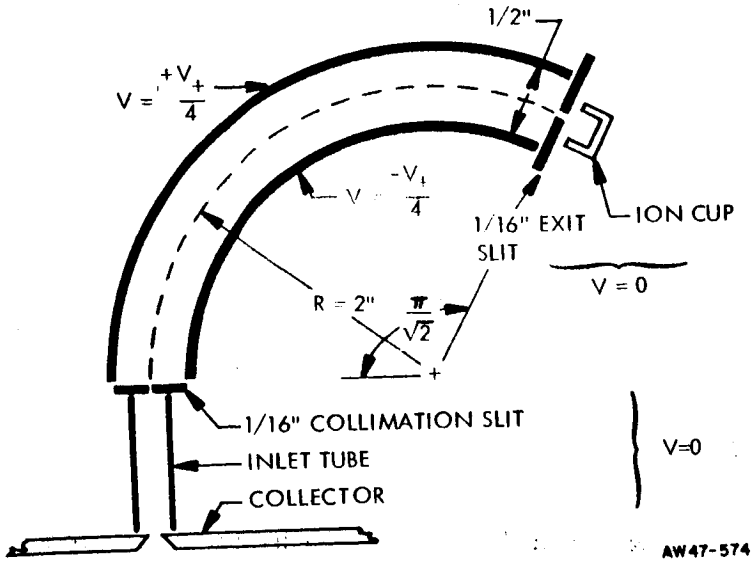

Figure 4. Schematic of 127° analyzer

E. Ion Divergence Analyzer

This instrument measures the angular distribution of ions arriving at the test location. Normally they will be virtually paraxial, but, as will be discussed in Section V, it is sometimes desirable to introduce an angular spread in their flow. As shown in Figure 5, the device consists of a rectangular aluminum box with an entrance aperture in one end and six collection rings at the other. In front of the rings is wire screen of 2 mil tungsten with 1/8 inch spacing.

In operation, the box itself is at or near V_p, the rings are held near ground potential by 100 KΩ resistors, and the screen bias is $\sim$ -20 V. Since V_p is typically 15 or 20 volts, the screen both repells plasma electrons and suppresses any secondaries from the rings. A multi-trace oscilloscope across the 100 KΩ resistors allows a continuous measurement of the ring currents.

Three basic factors limit the analyzer performance. Each is sufficiently small to be neglected in the experiments of Section V-E provided the beam has a uniform j_+ in the region of interest and a smooth angular distribution over a range of $\sim$ 8° or more from the axis. The former is always obtained near the beam center, and the sources of ion divergence discussed in Section V may be expected to produce a smooth distribution of angles. The following remarks note the effects of these factors when the range of angular divergence is less than $\sim$ 8°.

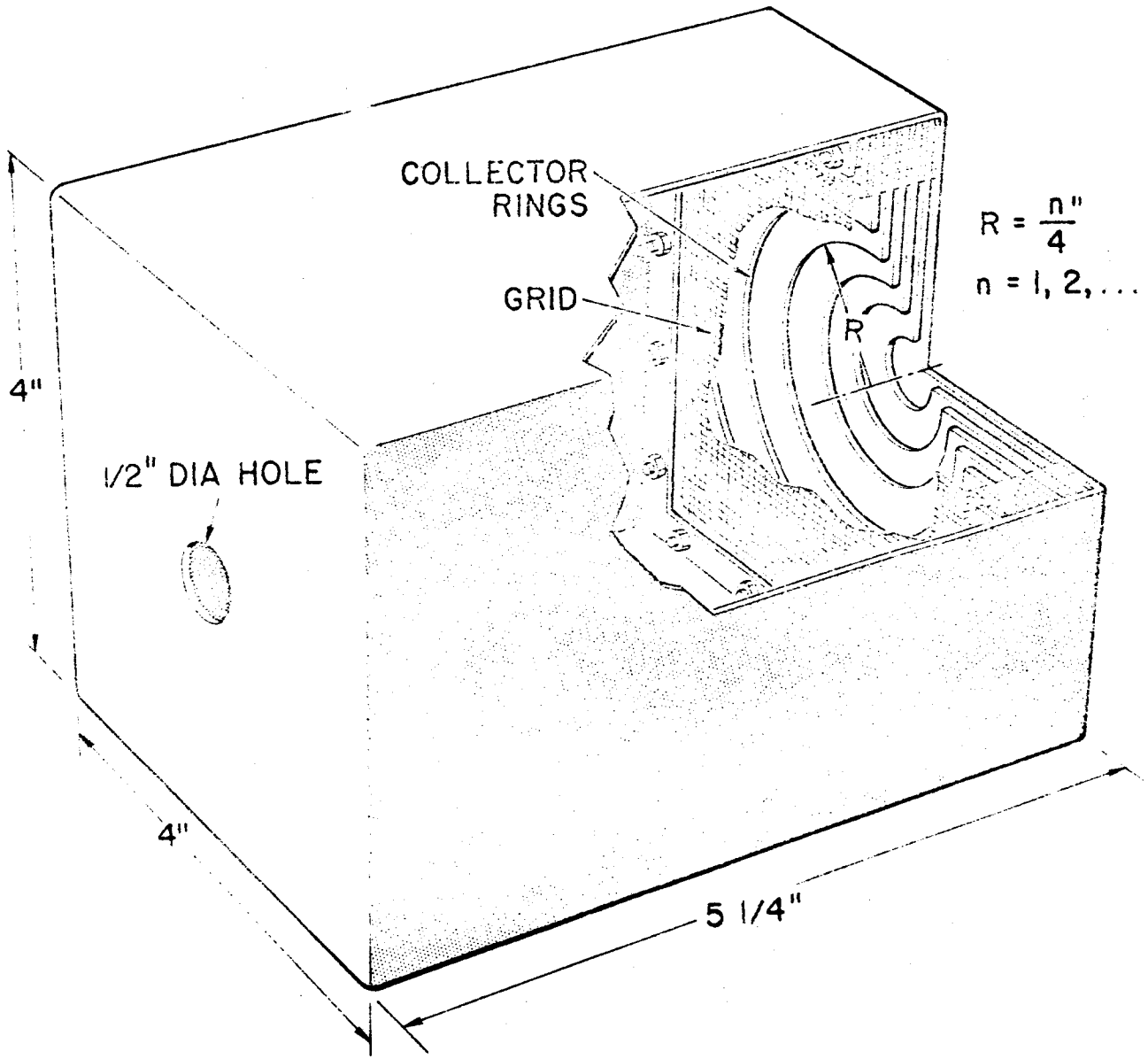

Figure 5. Perspective of ion divergence analyzer.

The discrete width of the individual rings requires that an ion passing through the center of the aperture have an angle in excess of 2-3/4 degrees to be recorded as other than paraxial. When the total spread of ions entering at the aperture center is $< 8°$, only three rings measure current.

The diameter of the entrance aperture, if large enough to obtain measurable ring currents, allows off axis ions to be collected on inappropriate rings. Under the assumptions of uniformity, it is possible to calculate this ring current distribution "broadening" from a particular source of diverging ions.

The "electrostatic lens" effects created by plasma sheaths in and around the aperture are perhaps the most involved. Experiments show that, as expected, biasing the box below V_p increases ion divergence while biasing the box above V_p produces an inward focusing effect. Small changes in aperture potential produce observable shifts in ring currents. Therefore work function patchiness near the aperture could be detrimental, if present. In the data given in Section V.E., the box was biased $\sim$1 to 2 volts above V_p, and an inward focusing effect on the ion trajectories was evidenced by a small maximum in central ring current from a beam of small divergence. This eliminated beam spreading forces due to poor charge neutrality inside the analyzer. A second condition, employed in other experiments, allowed the box to assume its floating potential, which is $\sim 2kT_e/q$ negative with respect to

the plasma if surface patch and wake effects[1] are disregarded. The additional noise signals encountered in this condition were reduced by capacitively coupling the box to ground. For over-all experimental convenience, the floating condition would be recommended.

In summary, these aspects of analyzer performance should be placed in perspective by noting that angular divergence in plasma wind tunnel streams represents a second order refinement. As such, construction of a more elaborate instrument would not, in general, be justified.

IV. BEAMS PRODUCED AND THEIR PROPERTIES

A. Ion Sources

Two types of ion source have been used in plasma wind tunnel studies--a 2.5 cm diameter contact ionization source and an 11 cm electron-bombardment source. The contact source[1,7,8,9] was used with Cs. The bombardment source was a flight model of the NASA, Lewis Research Center, Kaufman ion rocket[10,11,6] modified with a gas inlet tube and variable leak so that beams of various gas ions could be produced. Normal divergence of these beams is ~8 and ~25 degrees, half-angle, respectively.

B. Properties of Beams Produced

In general, there are six parameters which specify a plasma beam for simulation purposes:

1. average ion velocity, $\langle v_+ \rangle$
2. ion density at test location, ρ
3. diameter of uniform ion density at test location, D_b
4. ion mass constituents, M_+
5. ion velocity profile, $v_+|_{th}$, T_+ or ΔW
6. electron temperature, T_e

Most of these parameters are inter-related, and sometimes a compromise between desired values of two or more of them must be made.[7] The contact and bombardment sources behave differently, so they will be discussed in turn.

1. Contact Ion Source Beams

Because of the relatively large mass of cesium (133), velocities in the neighborhood of 8 Km/sec are attained with convenient acceleration voltages ($\sim$ 41 V). The ion current accelerated is, of course, a function of this voltage, but it is even more strongly dependent on accelerator-grid to plug spacing and the quality and temperature of plug itself. Without difficulty, D_b of 28 cm is obtained at 8 Km/sec with $\rho \sim 10^7 \text{ions/cm}^3$, and this density may be increased if required.

When Cs is used for ionospheric simulation, the required densities are $\sim$ 10 greater than ionospheric densities because of mass number scaling from 13 to 133. A discussion of scaling relationships between vehicle size, ion velocity, ion density, ion mass, and vehicle potential appears in Reference 1.

The cesium beam contains only Cs^+, and has virtually a line spectrum of velocity. Increasing T_e increases D_b, and it is usually set between 0.25 eV and several eV.[7]

2. Electron-Bombardment Ion Source Beams

The electron bombardment ion source does not have provision for varying the accelerator spacing and therefore the ion current produced is a function only of discharge conditions and acceleration voltages. Discharge conditions depend on the gas in use, discharge voltage, magnetic field, and cathode temperature. Figure 6 shows maximum densities obtained with various gases as a function of ion velocity. If less than the maximum density is required at a particular velocity, the discharge intensity is reduced. A typical value of D_b is 30 cm and a 30% reduction in ρ occurs at $\sim$58 cm diameter.

In addition to the A, N_2, Ne, He, and H_2, which appear in Figure 6, beams of O_2 and mixtures of CO_2 and A have been produced. Cathode lifetime is about one hour when O_2 is used (as compared to tens of hours with other gases) so that experiments with O_2^+ beams are limited in duration.

Table II lists beam constituents and width of ion energy distribution, $\Delta W'$, for various gases. This width is the difference between energies at which 0.1 peak value is attained, at beam energy qV_o.

The values of V_o shown produced sufficiently dense beams to allow convenient use of the 127° analyzer, and

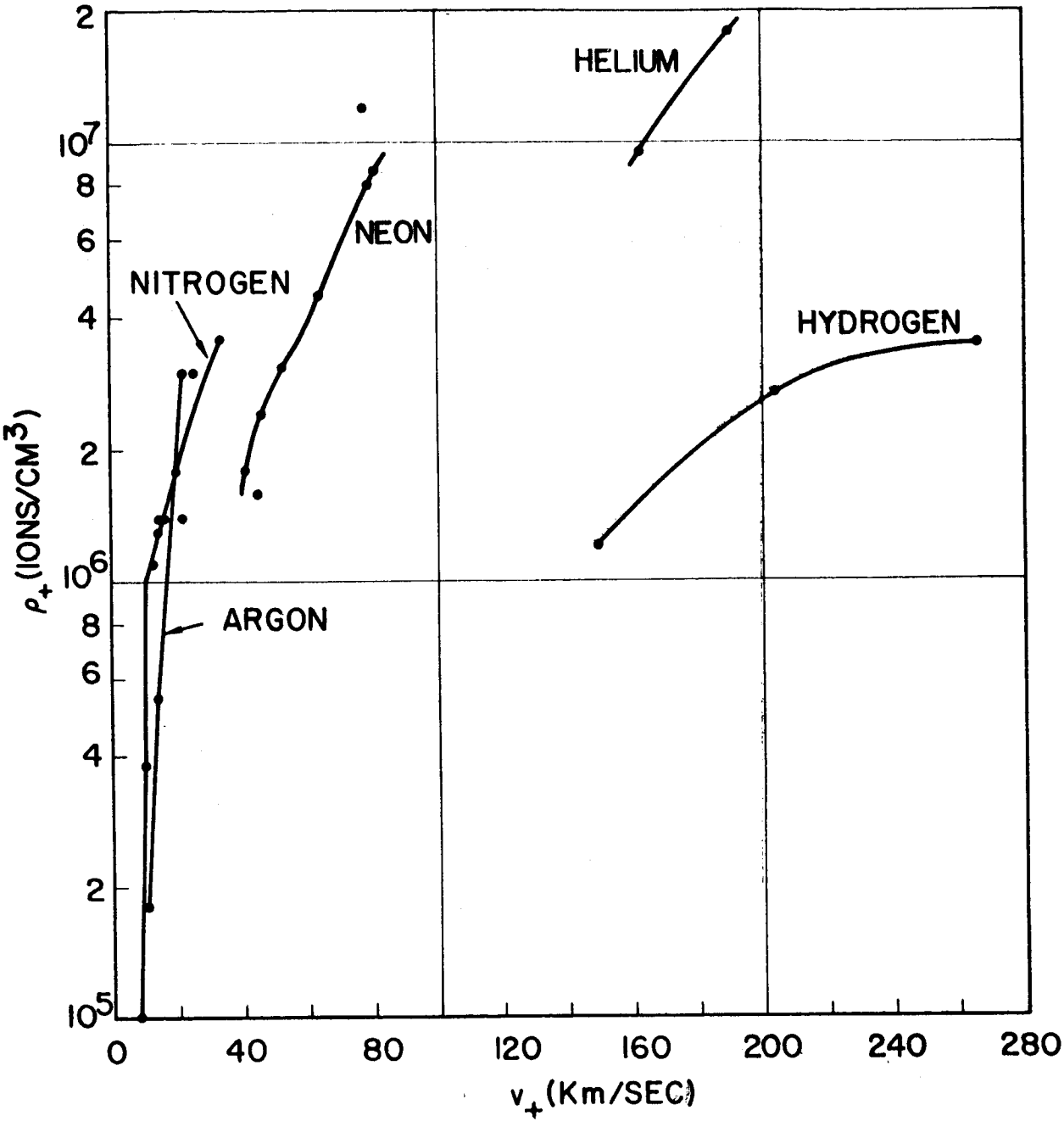

Figure 6. Maximum uniform plasma density available over 30 cm diameter area at 1.6 m from the electron bombardment source versus ion velocity for several gases.

Table II. Beam Constituents and Ion Energy Spread of Various Input Gases

Gas	Ions	$\Delta W'$(ev)	V_o(volts)
Hydrogen	12% H^+, 88% H_2^+	--	--
Helium	5% He^{++}, 95% He^+	--	--
Nitrogen	28% N^+, 72% N_2^+	10	68
Oxygen	~14% O^+, ~86% O_2^+ (tentative)	--	--
Neon	3% Ne^{++}, 97% Ne^+	14	181
Argon	4% A^{++}, 96% A^+	8	86

do not represent specific simulation conditions. Smaller values of $\Delta W'$ occur as V_o is decreased.

Production of 10 Km/sec beams from H_2 and He requires acceleration potentials of ~1 volt. The energy spread from the discharge is several times this value, so the present source is not suitable for these beams. A new source is under development which will be useful with H_2, He, and O_2.

In all of these beams, an immersed neutralizer was used, so $T_e \leq 0.25$ eV.

V. SIMULATION OF ION TEMPERATURE

The relative motion between a vehicle moving through the ionosphere and a particular ion or electron is the resultant of both the vehicle velocity and the thermal velocity of

the particle. As discussed in Section II, below the heliosphere the relationship

$$v_e\Big|_{th} >> v_s >> v_+\Big|_{th} \tag{1}$$

obtains. Therefore the relative velocities between the vehicle and the ions in the plasma are essentially v_s with a small randomizing ion thermal component, while the relative velocities between the vehicle and the electrons are almost totally randomized in direction and have magnitudes of $\sim v_e\Big|_{th}$. It follows that simulation of this small randomized ion velocity represents a refinement which may be omitted in many experiments. However it is interesting to first calculate $v_+\Big|_{th}$ as seen from a vehicle and then examine experimental techniques for its simulation.

A. Thermal Velocities From A Moving Frame Of Reference

For an assumed Maxwellian distribution of the ions in the laboratory frame the velocity distribution of the ions is given by

$$d^3N_{v_x v_y v_z} = N\left(\frac{M_+}{2\pi kT_+}\right)^{3/2} e^{-\frac{M_+}{2kT_+}(v_x^2 + v_y^2 + v_z^2)} dv_x\, dv_y\, dv_z \tag{2}$$

where M_+ is the ion mass, N is the total number of ions in the system, and T_+ is the ion temperature. If v_s is assumed to be in the negative z direction, and if the primed coordinates

denote the vehicle reference frame, then the ion velocity distribution, as seen by an observer moving with the vehicle is

$$d^3N_{v_x'v_y'v_z'} = N\left(\frac{M_+}{2\pi kT_+}\right)^{3/2} e^{-\frac{M_+}{2kT_+}\left[v_x'^2 + v_y'^2 + (v_z' - |v_s|)^2\right]} dv_x'\, dv_y'\, dv_z' \tag{3}$$

where

$$v_z' = v_z + |v_s| \,.$$

The first considerations will be directed temperature simulation in the "longitudinal" or z direction with the x and y components of the velocity neglected. That distribution is given by

$$dN_{v_z'} = N\left(\frac{M_+}{2\pi kT_+}\right)^{1/2} e^{-\frac{M_+}{2kT_+}(v_z' - |v_s|)^2} dv_z'. \tag{4}$$

Denoting the following

$$E_o = M_+ v_s^2/2 \text{ and } E_z' = M_+ v_z'^2/2 \,, \tag{5}$$

the distribution becomes

$$dN_{E_z'} = N\left(\frac{M_+}{2\pi kT_+}\right)^{1/2} e^{-\frac{1}{kT_+}\left[(E_z')^{1/2} - (E_o)^{1/2}\right]^2} \frac{dE'_z}{(2M_+E_z')^{1/2}} \,. \tag{6}$$

The energy "width" of this distribution is roughly described by the points at which $\left[\left(E_z'\right)^{1/2} - \left(E_o\right)^{1/2}\right]^2 = kT_+$, since $\left(2M_+E_z'\right)^{-1/2}$ is only slowly varying through this interval:

$$\Delta W' \cong 4(E_o kT_+)^{1/2} \quad . \tag{7}$$

As before, kT_+ is the thermal energy of the ions in the laboratory frame. It is seen that the energy spread of oncoming ions apparent from a vehicle moving with v_s is generally larger than $\Delta W \cong 2\ kT_+$, the energy spread in the fixed frame. Thus the simulation of "longitudinal" ion temperature requires larger velocity perturbations than Eq. (1) suggests.

For example, to simulate the motion of a vehicle at 10 Km/sec through a N_2^+ plasma at 1500°K ($2kT_+ = 0.26$ ev) the N_2^+ stream in the plasma wind tunnel should have a total width in the acceleration potential of ~ 5.5 volts centered about a mean acceleration potential of 14.5 volts.

B. Theory of Longitudinal Thermal Velocity Simulation

The simulation of T_+ in a plasma wind tunnel requires, in the longitudinal direction, an energy distribution whose width is given by Eq. (7). In the case of the electron bombardment source, a significant part of this $\Delta W'$ may arise from the fact that ions are formed in a region in which potential gradients exist. Furthermore, these gradients are, to some extent, influenced by the magnitude of the discharge potential and magnetic field, thereby allowing some control of the energy spread. Typical values of $\Delta W'$ are listed in Table II.

The natural energy spread of ions from the contact ionization source is, on the other hand, negligible. It arises primarily from the emitter surface temperature. When a constant amount of kinetic energy is added to each ion formed, the accelerated group has the same energy spread as before: $\Delta W = \Delta W'$. Equation 7, therefore, will indicate the approximate temperature of ions in the stationary frame which is simulated by their thermal spread at the contact source, namely

$$T_+ = \frac{(\Delta W')^2}{16\ k\ E_o} \quad . \tag{8}$$

As a typical example, consider an $\langle v_+ \rangle$ of 10 Km/sec (E_o = 69 eV for Cs) and an emitter surface temperature of 1500°K ($\Delta W'$ = 0.15 eV). The simulated temperature in the accelerated flow is then $\sim$ 0.1°K!

To increase the simulated longitudinal ion temperature of either source type, a periodic perturbation potential, V_1, may be superimposed on the accelerating potential, V_o which is otherwise constant during its periods of positive value:

$$V_+ = V_o + V_1 \tag{9}$$

Then ions exhausted at various times undergo differing amounts of acceleration. The following discussion will first treat the choice of frequency and then the choice of waveform for V_1.

The question of frequency is to assure that the velocity distribution of ions arriving at the object under test

is time invariant. Analysis is simplified by assuming a sinusoidal waveform: $V_1 = \tilde{V} \sin \omega t$. If $V_p = 0$ and

$$\tilde{V} << V_o, \tag{10}$$

then the velocity of ions emerging at time t is

$$v_+ \approx v_s \left(1 + \frac{\tilde{V}}{2V_o} \sin \omega t\right) \tag{11}$$

where

$$v_s = \left(2qV_o/M_+\right)^{1/2} .$$

As the ions move downstream, the velocity modulation introduced at the source will create "bunching" in the stream. Indeed, the present configuration may be termed an "ion klystron," and the conventional large signal klystron analysis applied.[12] The point downstream at which bunching first occurs is

$$\Lambda \simeq \frac{v_s}{\omega} \left(\frac{2V_o}{\tilde{V}}\right) . \tag{12}$$

The desired condition is that the plasma stream possess no such bunching but rather a density invariant in time. Clearly this will be achieved if the distance separating the plasma source from the vehicle, ℓ, is much greater than Λ. Experimental verification is presented in Section V.C.

The frequency requirements have been developed using a sinusoidal V_1. As indicated later, this waveform, while producing a spread in the ion energies, does not produce the

accelerated Maxwellian required for an ideal longitudinal temperature simulation. The required waveform is obtained from rewriting Eq. (6)

$$dN_{E_z'} = N \left(\frac{q}{4\pi k T_+} \right)^{1/2} e^{-\frac{q}{kT_+}\left[V_+ + V_o - 2(V_+ V_o)^{1/2}\right]} \frac{dV_+}{V_+^{1/2}} \quad , \tag{13}$$

where

$$V_+ = E_z'/q \quad , \qquad V_o = E_o/q \quad .$$

Use of Eqs. (9) and (10) permits simplification of the exponent and the denominator:

$$dN_{E_z'} \simeq N \left(\frac{q}{4\pi k T_+} \right)^{1/2} e^{-\frac{q}{kT_+}\frac{V_1^2}{4V_o}} \frac{dV_1}{V_o^{1/2}} \quad . \tag{14}$$

If Eq. (10) holds, or if the source is running emission limited, $dN/dt = i_+$ is constant. Thus

$$(dN/dV_1)\ (dV_1/dt) = i_+ \quad , \tag{15}$$

or

$$dt/dV_1 = \frac{N}{i_+} c\, e^{-c^2 V_1^2} \quad ,$$

where

$$c = \left(\frac{q}{4\pi V_o k T_+} \right)^{1/2} \quad . \tag{16}$$

Integrating,

$$t = \frac{N}{2i_+} \operatorname{erf}(cV_1) \quad . \tag{17}$$

Thus the required waveform is the error function, plotted in Figure 7 in the dimensionless units of the problem. Of course, the choice of t = 0 is arbitrary. The inequality Eq. (13) begins to fail near time values of plus and minus unity, and from the problem it is known that V_1 reaches some maximum absolute value. As a matter of electronic convenience successive waveforms would probably be reflected about the vertical axis of symmetry to produce a continuous periodic wavetrain. As discussed previously, its maximum period is determined by the requirement that $\ell \gg \Lambda$. Figure 8 shows this waveform and the velocity distributions produced by two more convenient waveforms. In the case of these non-Maxwellians, "temperature" may be defined by equating $\left\langle \left| v_+ - v_{+,o} \right|^2 \right\rangle$ of the distribution to $\left\langle v_z^2 \right\rangle$ of a Maxwellian.

C. Longitudinal Thermal Velocity Simulation Experiment

To demonstrate that time invariant temperature simulation could be achieved through the rapid variation of the source potential, the experimental configuration in Figure 9 was assembled. The perturbation potential V_1 was $\tilde{V}$ sin ωt and V_o, $\tilde{V}$, and ω could be varied. The output of the 127° analyzer was used as the vertical input to an oscilloscope; the horizontal sweep was derived from the analyzer deflection voltage, V_d. The scope beam was blanked so that the trace was only visible during a 1-μsec sampling pulse which was delayed from the zero crossing of V_1. Each of the scope face photographs, Figure 10, represents a single sweep of V_d through the range

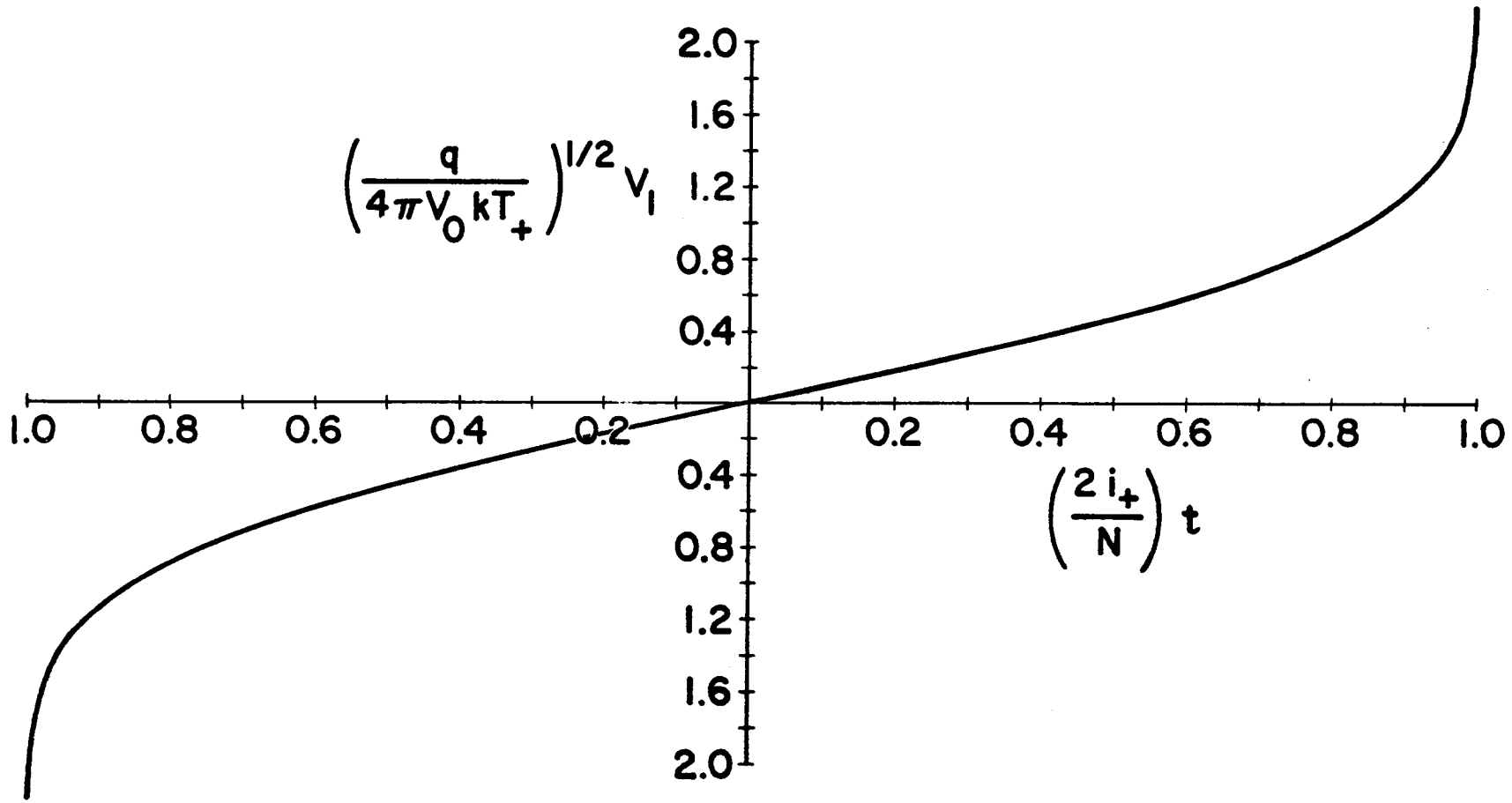

Figure 7. Waveform of perturbation potential V_1 required to simulate a Maxwellian "longitudinal" energy distribution.

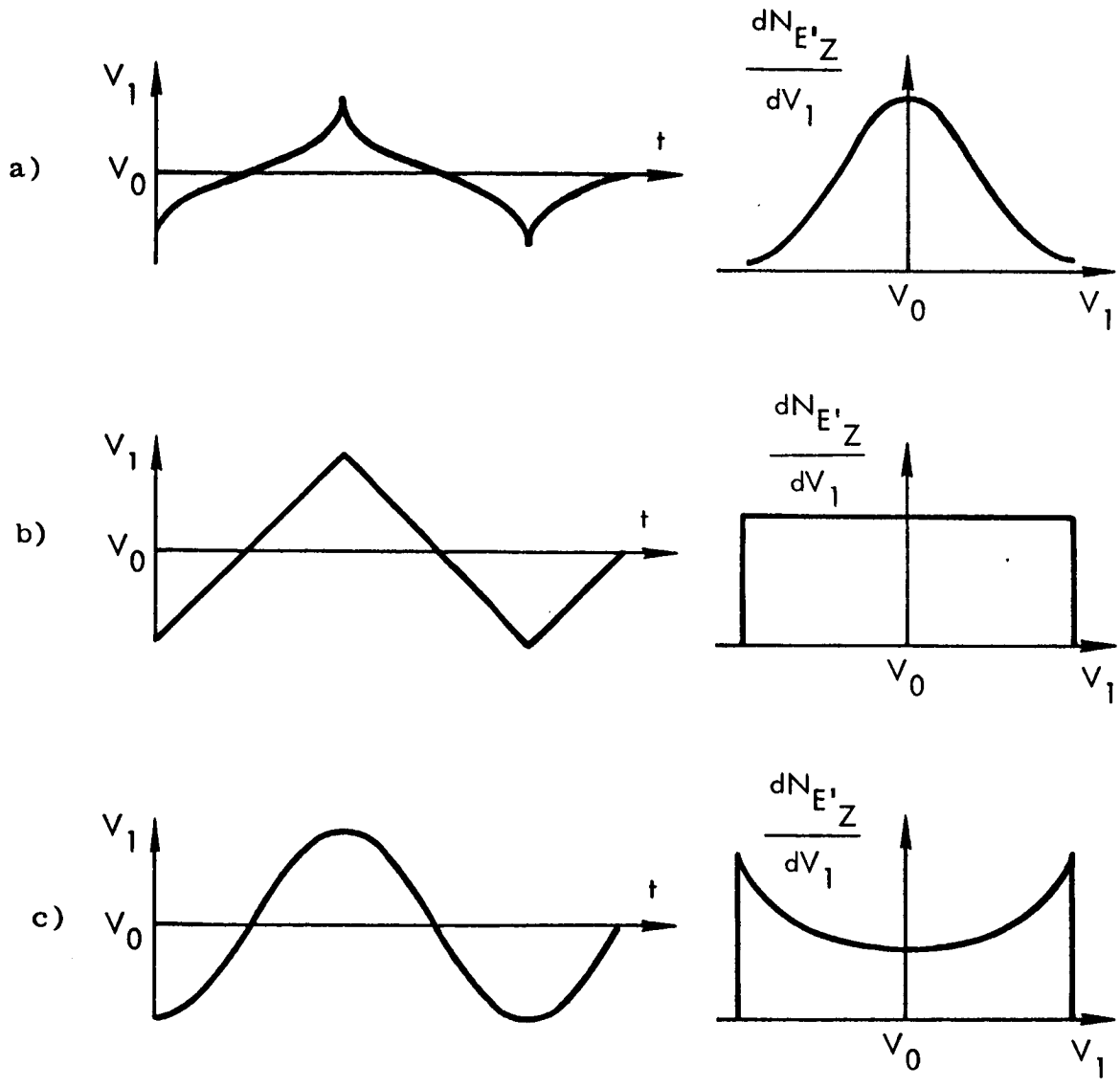

Figure 8. "Longitudinal" energy distributions produced by various perturbation potential waveforms.

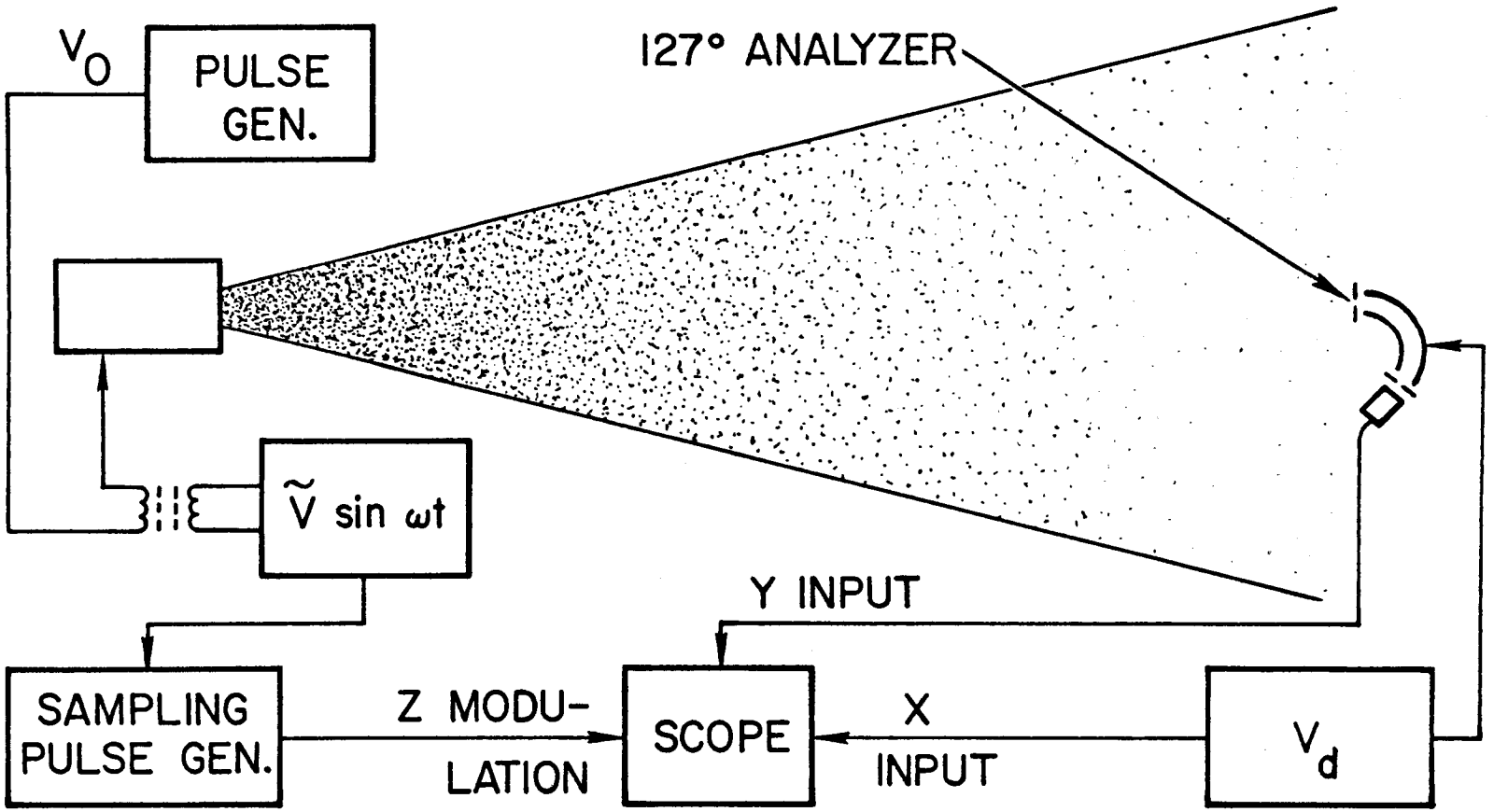

Figure 9. Schematic diagram of longitudinal thermal velocity simulation experiment.

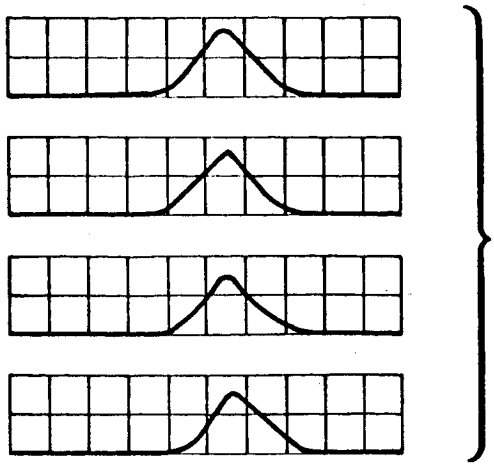

Figure 10c. $V_1 = 9 \sin (2\pi \cdot 250$ Kc t). Shots at several times t in the range $nT \leq t \leq nT+1$. Good temperature simulation obtains.

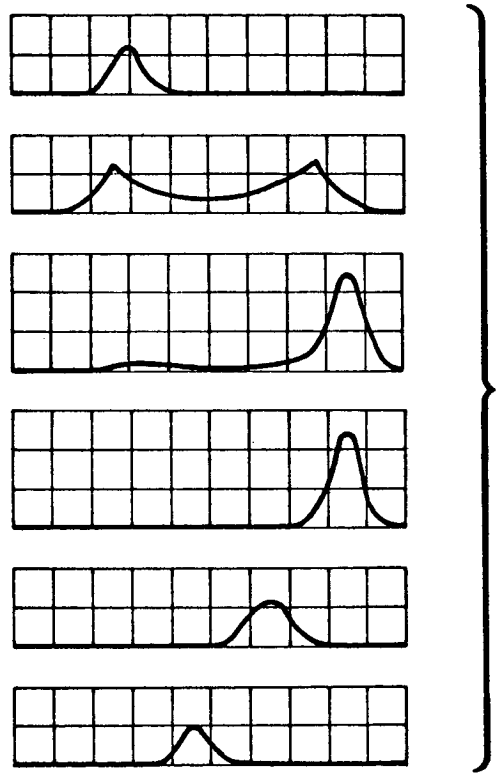

Figure 10b. $V_1 = 32 \sin (2\pi \cdot 25$ Kc t). Shots at several times t in the range $nT \leq t \leq nT+1$. Poor temperature simulation obtains.

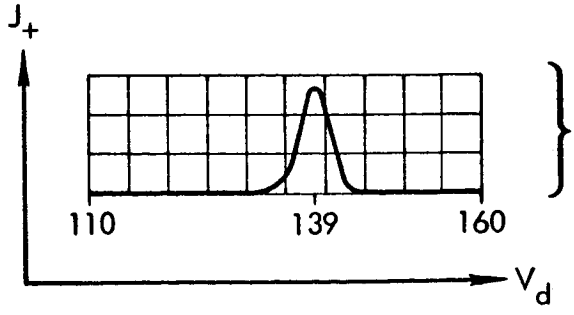

Figure 10a. Output of 127° analyzer. Perturbation voltage $V_1 = 0$.

of interest with a fixed value of time delay. Therefore they are plots of the ion energy spectrum at different phases of V_1. The horizontal scale begins at 110 V and each division represents 5 V. The physical parameters of the analyzer are such that $V_+ = 2\ V_d$.

Figure 10a was taken with $V_1 = 0$, and the peak occurred at $V_d = 139$. Such values of V_d, corresponding to $\langle V_+ \rangle$ of an unperturbed beam, will agree within 3% with time-of-flight measurements which have been carefully corrected for the error sources mentioned in Section III.D.1. However, the shape of the energy spectrum in Figure 10a is more representative of the analyzer "window" than of the energy spectrum of the unperturbed Cs^+ beam. Nevertheless, the analyzer is very useful in observing the effect of a perturbation voltage, as comparison of Figure 10b and Figure 10c to Figure 10a will show.

In Figure 10b, a 25 Kc, 32 V peak signal has been added to V_o. The distance ℓ is 191 cm. Starting at the top of the group, each photograph was taken with a longer delay time from the zero crossing of V_1, and the bottom trace, almost one period of V_1 later. At first only ions which have been slowed down are present (compare to Figure 10a). Then a mixture of energies appears, followed by a single group of "fast" ions (the maximum attained). As time progresses, this group becomes less and less energetic until the minimum energy, which began the sequence is attained.

To relate these spectra in detail to the phase of the V_1 is complicated. But this is not necessary to see that

these values of ω, $\tilde{V}$ and V_o did not lead to a time invariant mixture of energies which could be regarded as a simulated ion temperature. Nor should they be expected to, since ℓ/Λ is 0.87 in this case. Notice that if all six traces are added, the shape of the resulting energy distribution is similar to that of Figure 8c.

When the frequency was increased to 250 Kc, even though V_1 was reduced to 9 V peak, $\ell/\Lambda = 2.4$. Again photographs were taken at different times throughout a period of V_1 and representatives are shown in Figure 10c. Now the peak energy occurs at ~ 139 volts (just as with $V_1 = 0$ in Figure 10a) regardless of the phase of V_1. The effect of V_1 has been to broaden the energy distribution and simulate an ion temperature. However, the natural line width of the analyzer is important at this small amplitude of V_1.

D. Theory of Transverse Thermal Velocity Simulation

As indicated in Eq. (3), the radial ion velocity, $v_r = \left(v_x^2 + v_y^2\right)^{1/2}$, is unaffected by the relative motion of plasma and the spacecraft. Therefore a perfect simulation of the ion temperature in the transverse direction would produce

$$dN_{v_r} = N \frac{M_+}{kT_+} v_r \, e^{-\frac{M_+ v_r^2}{2kT_+}} \, dv_r \qquad (18)$$

As in the longitudinal case, something short of the ideal may be satisfactory for an experiment and more easily produced.

In fact, the use of an ion source of finite extent provides some transverse velocity. In both source types which have been described, each element of accelerator grid acts as a separate plasma source. Owing to the electrostatic lens action of this grid and the effects of energetic neutralizing electrons, the angular velocity distribution from each sub-beam is essentially uniform up to an angle θ.

However, the maximum v_r of a particle arriving at an on-axis point downstream can not be greater than $\sim v_+ r_{is}/\ell$. Therefore

$$v_r\Big|_{max} = \frac{v_+ r_{is}}{\ell} \quad \text{or} \quad v_+ \sin\theta \tag{19}$$

whichever is the smaller.

The $\langle v_r \rangle$ of this uniform angular distribution from the source is $(2/3)\, v_r\Big|_{max}$. To define an effective temperature for the residual transverse velocity spectrum of a source-object configuration, this average value of radial velocity is equated to that of Eq. (18):

$$T_{eff} = 8\, M_+\, v_r^2\Big|_{max} (9\pi k)^{-1} \tag{20}$$

where $v_r\Big|_{max}$ is given by Eq. (19).

Whether this temperature is sufficient in a given experiment depends on the values θ, ℓ, r_{is}, and v_+. The choice of r_{is} and ℓ in turn depends on the size of the object under test. The value of θ depends on the magnitudes of acceleration

voltages, grid spacing, grid hole size, and T_e. In general, it is $\sim 3°$ for the contact ionization source and $\sim 10°$ for the electron bombardment source.

Often values of the parameters appropriate for simulation of ionospheric travel lead to a residual transverse temperature of a few hundred degrees Kelvin or less. Since a value in the range 1000-2000°K (relative to $v_+ \approx 8$ Km/sec) is usually desired, some artifical technique to increase the range of v_r must be employed.

The technique investigated consisted of placing a large, coarse grid in the beam between the source and object. With a suitable negative potential on the grid, the ion flow interacted with these electric field centers, increasing their transverse momentum distribution. The design of such a grid -- mesh size, mesh shape and thickness, downstream location, and potential -- is involved since space charge calculations are required. After preliminary calculations, the configuration described in the next section was used to demonstrate the technique.

E. Transverse Thermal Velocity Simulation Experiment

The natural transverse thermal velocity distribution of 180 volt N_2^+ plasma from the 11 cm electron bombardment source was measured with the ion divergence analyzer. Its distance from the source was 1.6 m. The ratio of currents ring 1/ring 2 was 1.6. Because this configuration represented an angular distribution of less than 6°, the analyzer entrance

aperture size could not be neglected. Using the previously discussed uniformity assumptions, an expression was derived for the ring currents due to an off axis source point, using the actual areas of collector rings and aperture. This expression integrated over the entire source area predicted $R_2 = 2.0$. Agreement within 20% for the measurement of low divergence beams is satisfactory.

This source to object configuration corresponded to a residual transverse temperature of 1450°K at the value of v_+ used (35 Km/sec). However, transverse temperature scales as v_+^2, so at 8 Km/sec the temperature would have been 74°K. The experiment was done with the high value of v_+ to provide a more convenient signal level from the analyzer. ($\rho_o \simeq 2 \times 10^6$ ions/cm^3 at the analyzer location.)

To enhance this transverse velocity distribution, a 1-meter square cross grid of 10 mil wire spaced 2.5 cm was placed in the vacuum tank 53 cm upstream of the analyzer. This location was convenient and met the following two conditions: If the scattering grid is too close to the analyzer ($\lesssim \sim 10$ wire spacings), the beam at the entrance aperture may not be homogeneous; if the grid is too far, the maximum transverse velocity of particles entering the analyzer becomes small as in the case of the distant ion source.

Figure 11 shows the ratios of ring 1 current to the currents of rings 2, 3 and 4, with scattering grid potential as the parameter. The currents to rings 3 and 4 for the -20V case include a large percentage of noise.

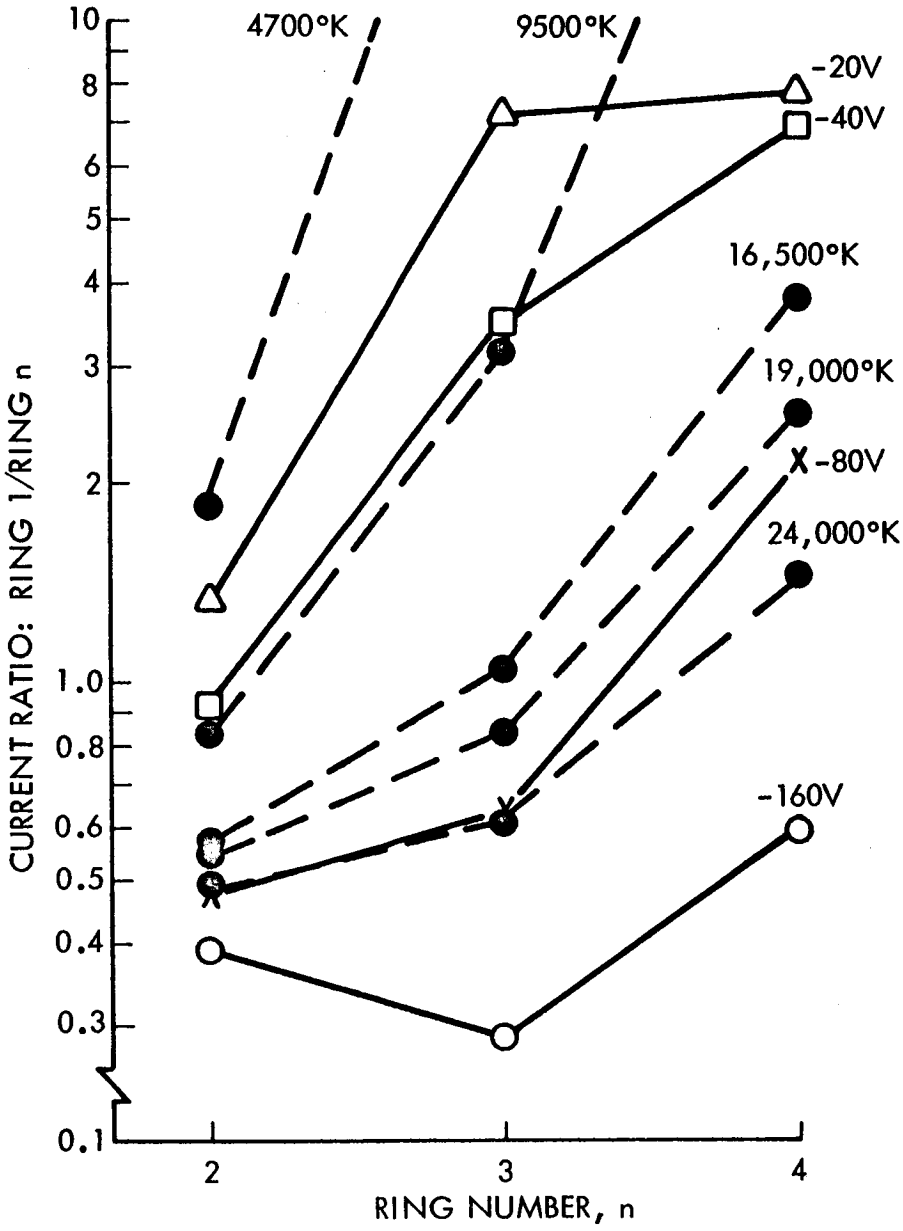

Figure 11. Solid lines: Measured ratios of ring 1 currents to currents of rings 2, 3, and 4 for various scattering grid potentials. Broken lines: Calculated values of these ratios for various transverse temperatures.

To interpret this data in terms of a Maxwellian distribution, calculations of ring currents were made which assumed transverse Maxwellians of various temperatures at the entrance aperture (now assumed infinitely small in area). Under the latter assumption,

$$v_r = v_+ r\, L^{-1} \tag{21}$$

where L is the axial length of the divergence analyzer and r is the radial location of the point at which the ion is collected. Substituting this expression into Eq. (18) and integrating between values of r which represent the dimensions of each collector ring yields the current ratios also shown in Figure 11. Apparently -80V on the grid approximates 20,000°K rather well at $v_+ = 35$ Km/sec. Were this same distribution of ring currents observed with a v_+ of 8 Km/sec, it would correspond to $\sim$ 1000°K. Thus the scattering grid is capable of an effective simulation of the transverse thermal velocity distribution which an orbiting spacecraft would encounter in the ionosphere.

VI. SUMMARY

Spacecraft travel through the region of the ionosphere below the heliosphere may be simulated in vacuum chambers by directing a moving plasma stream against a stationary vehicle. For this purpose streaming plasmas of H_2, He, N_2, O_2, Ne, A, CO_2 and mixtures thereof have been synthesized with an electron bombardment ion source. A contact ion source produced

cesium beams, useful when line velocity spectra were required. Pertinent properties of the ionosphere have been reviewed and diagnostic instruments for determining these same properties in the synthesized streams described.

The extent to which ion thermal velocity in the ionosphere effects the relative motion between the ions and a vehicle has been calculated. As a simulation refinement, criteria for generating these effects in the plasma wind tunnel have been derived and experimentally demonstrated.

The controlled operation of these plasma sources over a wide range of parameters permits laboratory study of the interaction of material bodies moving through dilute plasmas, and the calibration of on-board instrumentation for the diagnosis of the dilute plasmas of space.

REFERENCES

1. Hall, D. F., Kemp, R. F., and Sellen, J. M., Jr., "Plasma-vehicle interaction in a plasma stream," AIAA J. 2, 1032-1039 (1964).
2. Hanson, W. B., "Structure of the ionosphere," Satellite Environment Handbook, edited by Francis S. Johnson (Stanford University Press, Stanford, California, 1961), pp. 27-46.
3. van de Hulst, H. C., de Jager, C., and Moore, A. F., editors, Space Research II, Part VIII (North-Holland Publishing Company, Amsterdam, 1961), pp. 889-1017.
4. Hanson, W. B., "Upper-atmosphere He ions," J. of Geophysical Research, 67, 183-188, (January 1962).
5. Bourdeau, R. E., Whipple, E. C. Jr., Donley, J. L., and Bauer, S. J., "Experimental evidence for the presence of He^+ based on Explorer VIII satellite data," J. of Geophysical Research, 67, 467-475, (1962).
6. Kemp, R. F., Sellen, J. M., Jr., and Pawlik, E. V., "Neutralizer tests on a flight-model electron-bombardment ion thrustor," NASA TN D-1733 (July 1963).
7. Sellen, J. M., Jr., Bernstein, W., and Kemp, R. F., "The generation and diagnosis of synthesized plasma streams," Submitted to Rev. Sci. Instr., 17 August 1964.
8. Sellen, J. M., Jr. and Kemp, R. F., "Cesium ion beam neutralization in vehicular simulation" ARS Preprint 61-84-1778 (June 1961).

9. Bernstein, W. and Sellen, J. M., Jr., "Oscillations in synthetic plasma streams," Phys. Fluids, Vol. 6, No. 7 (July 1963).

10. Kaufman, H. R., "An ion rocket with an electron-bombardment ion source," NASA TW D-585, January 1961.

11. Reader, P. D., "Experimental effects of scaling on the performance of ion rockets employing electron-bombardment ion sources," ARS Journal 32, 711-714 (1962).

12. Field, L. M., "Generation of high-frequency energy," Foundations of Future Electronics, edited by D. B. Langmuir and W. D. Hershberger (McGraw-Hill Book Co., Inc., New York 1961).

SECTION II.B.

MERCURY OPTICAL RESONANCE PROBE

MERCURY OPTICAL RESONANCE PROBE

I. INTRODUCTION

The detection of atoms by means of optical resonance absorption has been a laboratory tool for many years. Techniques making use of resonance absorption have proved to be sensitive, highly selective, and very successful. Recently, the absorption technique has been proposed as a practical way of studying the propellant utilization of an ion engine by the detection of neutral atoms within the exhaust plasma of the engine.

A theoretical discussion of resonance absorption may be found in Ref. 1. This report treats the problems of hyperfine line structure, line width, and source self absorption. An expression for the absorption as a function of atom density was derived taking into consideration the structure of the spectral lines from the light source. The experimental mercury absorption curve was in excellent agreement with this theoretical expression. Ref. 1 also describes a mercury optical resonance probe which was installed on a mercury electron bombardment ion thrustor developed by NASA, Lewis Research Center.[2,3] The propellant utilization of the engine was determined from optical measurements of the neutral atom density of the exhaust plasma with the engine operating at moderate thrust.

In order to extend measurements of the propellant utilization to ion engines of high thrust, an in-line mercury optical resonance absorption probe was developed. This probe was installed on the electron bombardment ion thrustor, and results of its optical measurements are given below. The results of optical measurements are in good agreement with gravimetric measurements.

II. RESONANCE PROBE OPTICAL SYSTEM PHYSICAL DESCRIPTION

The resonance probe consists of three basic items: a source of light, a collimator system to define the absorption region, and a detector assembly. The light source is a small mercury lamp. Radiation from the lamp is coded by a light chopper wheel before it enters the vacuum chamber. The vacuum chamber contains the ion engine and the light collimating system. The detector assembly consists of an absorption cell, a reflection grating, and a photomultiplier tube. This assembly is outside the vacuum chamber for convenience. Figure 1 illustrates the essential features of the probe. Figures 2 and 3 show the probe mounted on the vacuum tank with the ion engine removed.

The mercury lamp is a quartz bulb one inch long and one quarter inch in diameter. It contains a droplet of mercury, and a buffer gas of neon at a pressure of 5 mm Hg. The discharge is excited at 25 MC. The bulb is protected from air currents and changes in the ambient air temperature by an aluminum enclosure which serves as the mounting bracket to the vacuum chamber. The aluminum box also contains the first optical collimator.

Formation of the light emitted by the mercury lamp into pulses by a light chopping wheel permits the separation of the phototube signal produced by the lamp from that arising from other light, e.g., light coming from the engine. The light chopper is an aluminum disc 1/16 inch thick and 9 inches in diameter. Eight slots, equally spaced, are cut into the disc near the outer edge. When the disc is driven at 1800 RPM, the light from the lamp consists of pulses 2 milliseconds long every 4 milliseconds. Both the size and shape and the number of holes were varied at times during this study to change the pulse length, rise time, and the repetition rate.

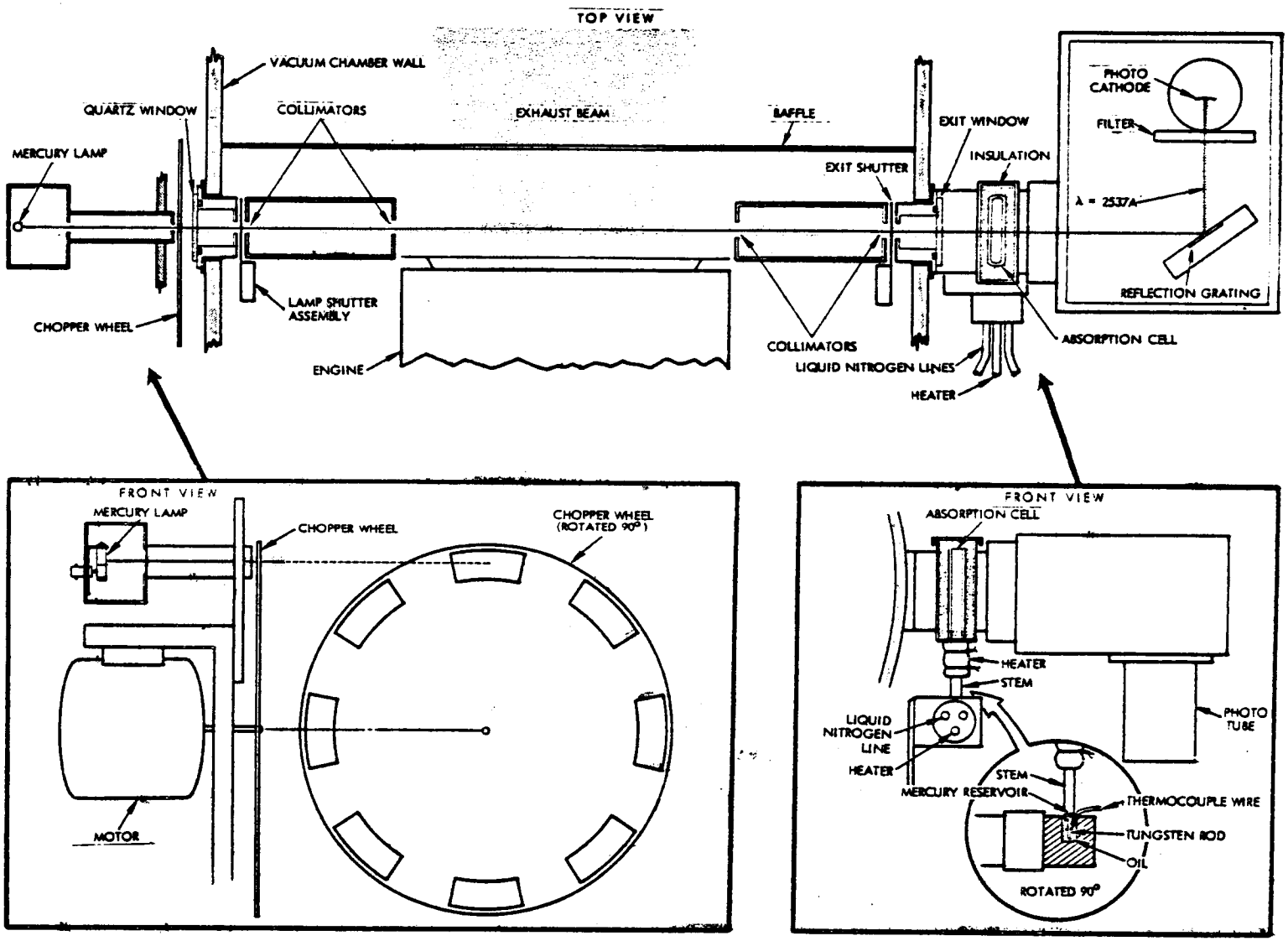

Fig. 1. The inline mercury probe optical system. The main features of the mercury probe are illustrated with mercury lamp, chopper wheel, and the absorption cell shown in greater detail. Light from the mercury lamp is first formed into pulses by the rotating chopper wheel and collimated before passing through the exhaust beam of an ion engine. The transmitted light is then analyzed spectrally by a reflection grating and filter before it strikes the photocathode of a photomultiplier tube. An absorption cell is included to permit calibration of the probe.

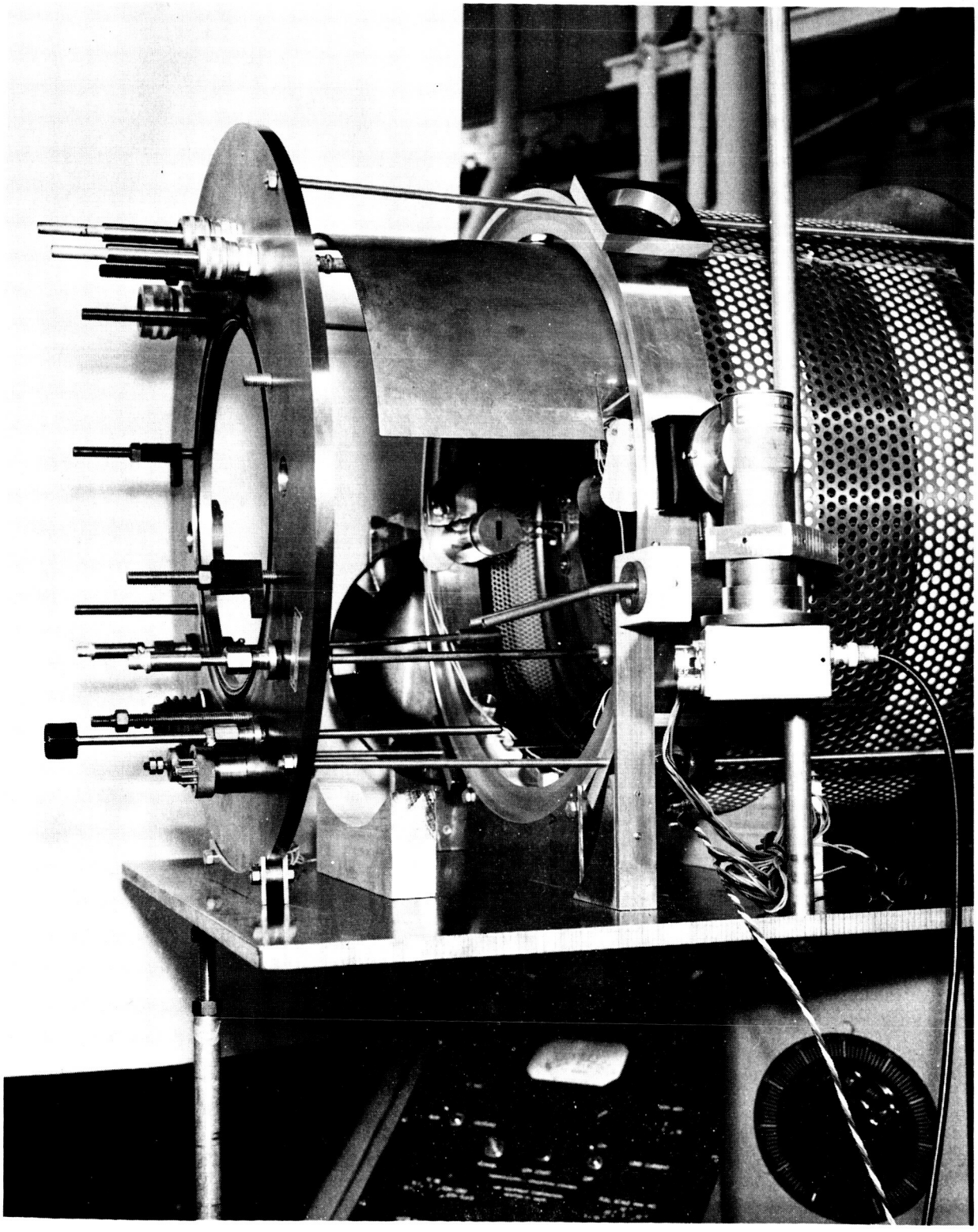

Fig. 2. Side view of probe installed in vacuum tank. The ion engine has been removed. The mercury lamp housing, chopping wheel, collimators, baffles, window shutters, and absorption cell housing are visible. The reflection grating and the filter are not installed.

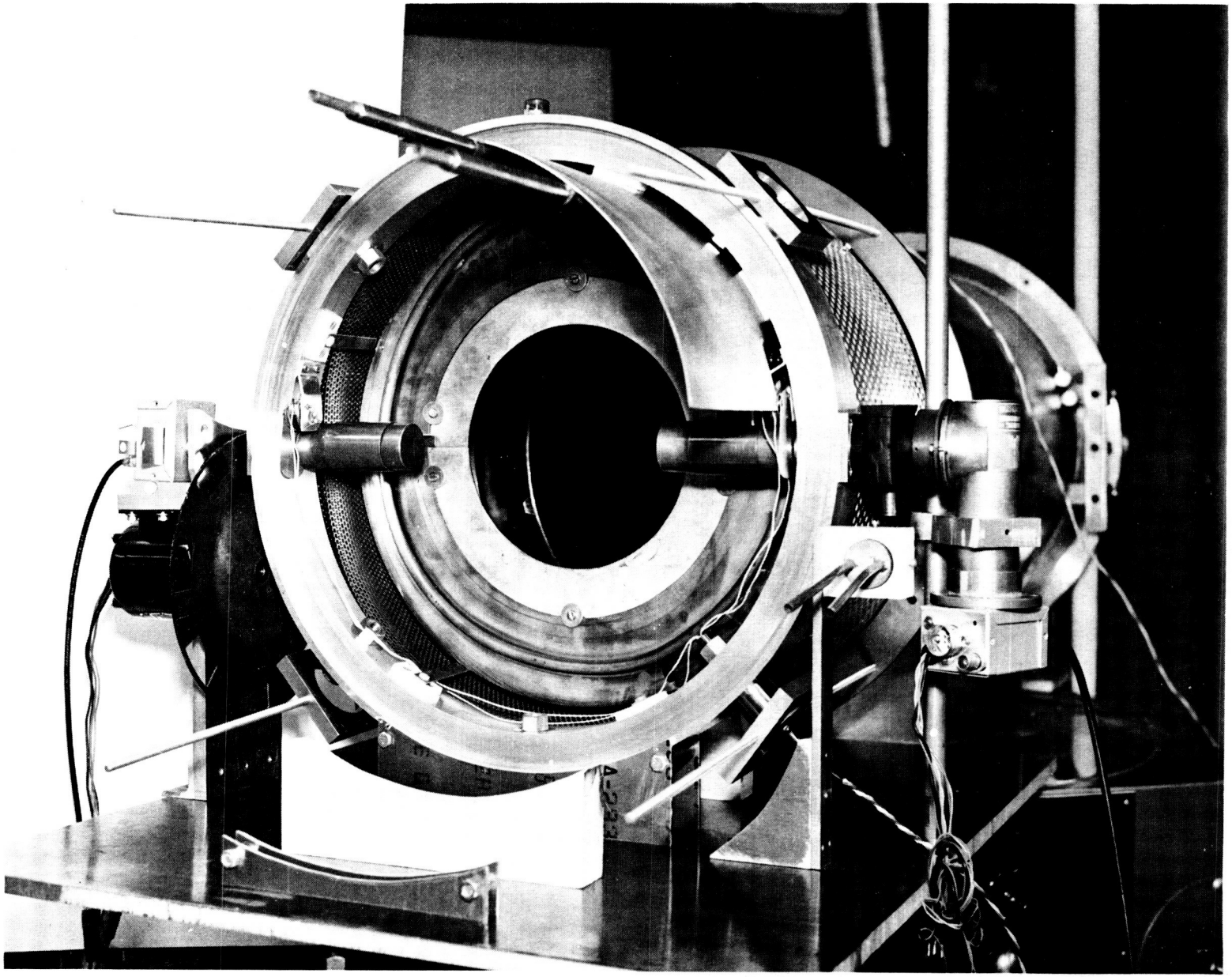

Fig. 3. Front view of the probe on the vacuum tank before installation of the ion engine. The reflection grating and filter are not included.

The light enters the vacuum system by means of a quartz window. It then passes through several collimators which define the optical path through the engine exhaust. A second quartz window provides the exit from the vacuum.

The collimator system is designed so that the 2537A line from the lamp will just illuminate all of the photocathode of the photomultiplier tube after analysis by the reflection grating. Consequently the collimator apertures vary in size from 3/16 inch by 5/8 inch at the entrance window to 5/16 inch by 11/16 inch at the exit window. This collimator system provides maximum protection for the windows. At the same time the collimators minimize the exposure of the photocathode to light generated in the engine. Two remotely controlled shutters are placed next to the inside surface of the quartz windows. With the shutters closed, the windows are protected from being coated by residual mercury vapor and particles from the engine and its exhaust plasma. The shutters are opened just long enough to take a measurement of the transmitted light intensity (from about 1 second to less than 10 seconds). In addition, baffles are placed to prevent backstreaming of mercury atoms. The baffles and the collimator system are mounted so that they do not intercept the exhaust plasma. Both the baffles and the collimators are cooled to liquid nitrogen temperature for cryogenic pumping of all mercury atoms that strike their surfaces.

An absorption cell is placed in the optical path between the exit window of the vacuum chamber and the detector. The inclusion of an absorption cell permits a calibration of the optical system to be made at any time. Except during such calibration runs, the absorption cell is maintained near liquid nitrogen temperature. The cell itself consists of a thin quartz cylinder with a hollow tube attached to the side of the cylinder. The entrance and exit windows are two flat parallel

quartz discs 1-1/4 inch in diameter. The inner surfaces of the discs are 3 mm apart. A cylindrical stem of thermally graded glass is attached at a point along the edge of the cell. The inside diameter of the stem is slightly larger than the window separation. A tungsten rod intrudes through the bottom of the stem and makes thermal contact with a small pool of distilled mercury. In operation, the cylindrical part of the cell and the stem are heated to a considerably higher temperature than that of the mercury reservoir. Thus, the mercury vapor pressure inside the cell is controlled by the temperature of the tungsten rod. The equivalent area density of the cell in the optical path is then easily calculated from published vapor pressure tables.[4]

The light transmitted through the collimating system and through the absorption cell is reflected from a front surface diffraction grating so that the 2537A line of mercury falls on the center of the photocathode after passing through a filter transparent in a small region about 2537A. Both a grating and a filter are used since it was found that the filter by itself transmits significant quantities of light outside its transmission band, especially at the longer wave lengths, and the space available does not permit the long moment arm needed to obtain high spectral resolution with the grating only. In addition, a long moment arm would reduce the light intensity on the photocathode and result in a less sensitive system. The combination of a reflection grating and a narrow pass band filter effectively shields the photocathode from light of wavelength other than 2537A with a high transparency to 2537A radiation.

The optical detector is a type 7200 photomultiplier tube. This is a nine-stage side-window tube with a maximum response near 3300A. The signal from the anode of the phototube is

displayed on an oscilloscope with a differential comparator preamplifier. The signal can then be directly measured with the differential comparator or the scope trace simply photographed. By photographing the oscilloscope trace, the time that the window shutters are open is reduced to about one second for each measurement.

III. OPTICAL RESONANCE PROBE -- OPERATION

The optical measurement of the propellant utilization of an operating ion engine is straightforward. After the lamp has become stable, the optical system is calibrated by means of the absorption cell. The transmission of the absorption cell as a function of the cell temperature is measured. From these measurements the absorption versus mercury density curve is obtained (see Fig. 4). The absorption cell reservoir is then frozen to liquid nitrogen temperature and maintained at this temperature for the rest of the experiment. The ion engine is turned on and stabilized at the desired boiler temperature and arc current. The transmission through the exhaust plasma is measured. The arc is momentarily turned off and the transmission again measured. Figure 5 illustrates three scope traces with an engine boiler temperature of 300°F. Trace A shows the background light generated when the engine is on. Trace B is the lamp signal transmitted through the exhaust plasma superimposed on the background from the engine. Trace C is the transmitted signal with the boiler hot but the arc off.

The in-line mercury optical resonance probe is a reliable instrument. Straight-line design permits a short optical path and a minimum number of optical surfaces resulting in an instrument of high sensitivity. However, a few precautions must be heeded. The stability and the spectral line shape of the light source must be known before a proper interpretation of the absorption may be made. All optical surfaces must be protected to prevent the build up of light-attenuating films. The response of the photodetector should be carefully checked since most photosensitive devices exhibit both short term and long term saturation effects and sensitivity changes.

The intensity of the mercury lamp used for these measurements shows large fluctuations when first turned on or whenever

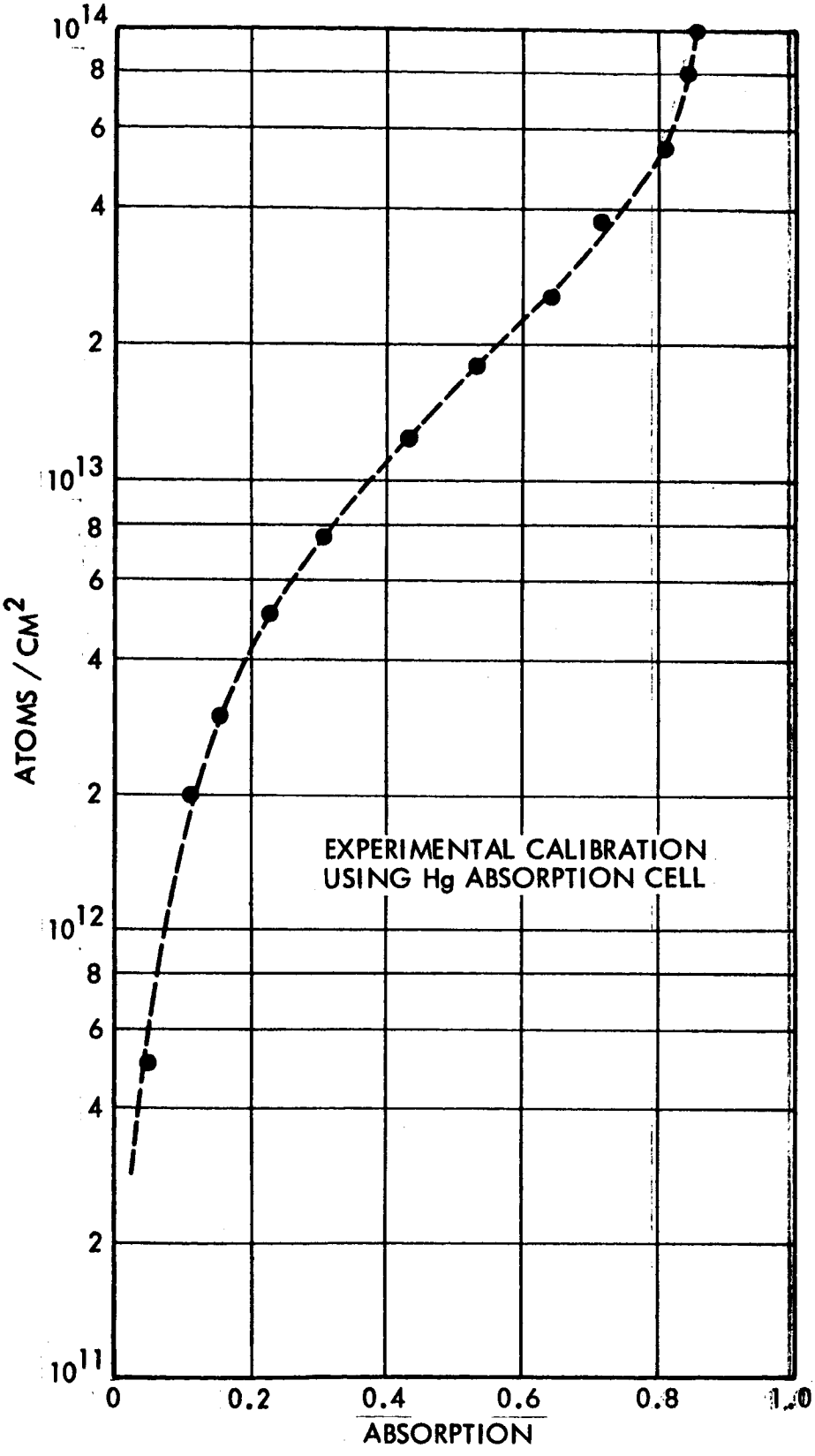

Fig. 4. The mercury calibration curve for the optical probe.

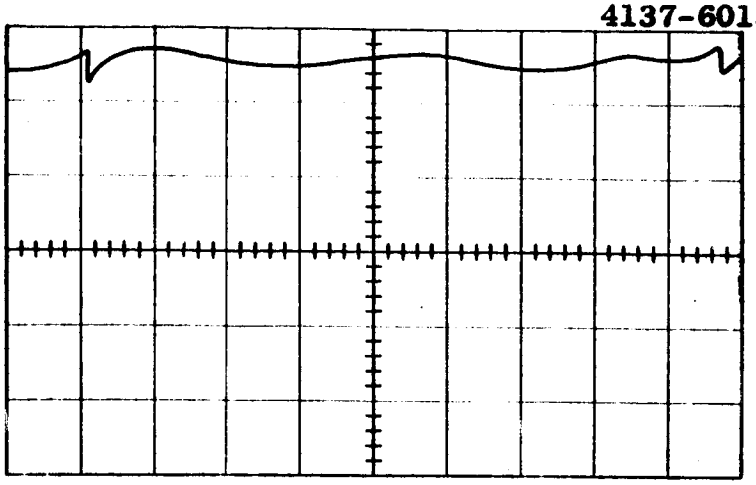

(A) ARC ON - LAMP SHUTTER CLOSED

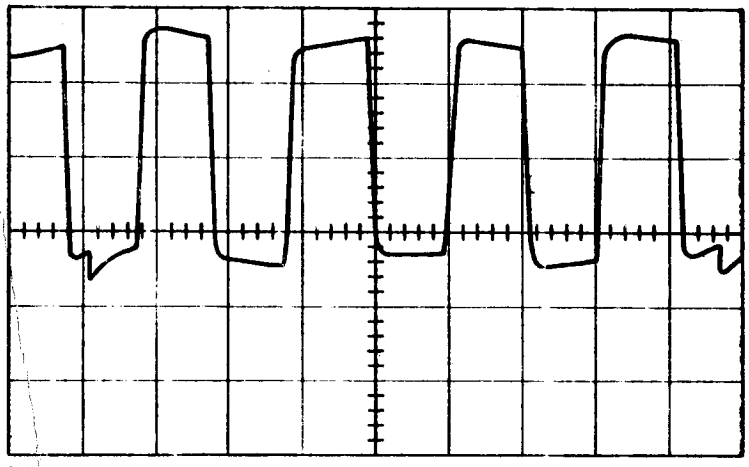

(B) ARC ON - LAMP SHUTTER OPEN

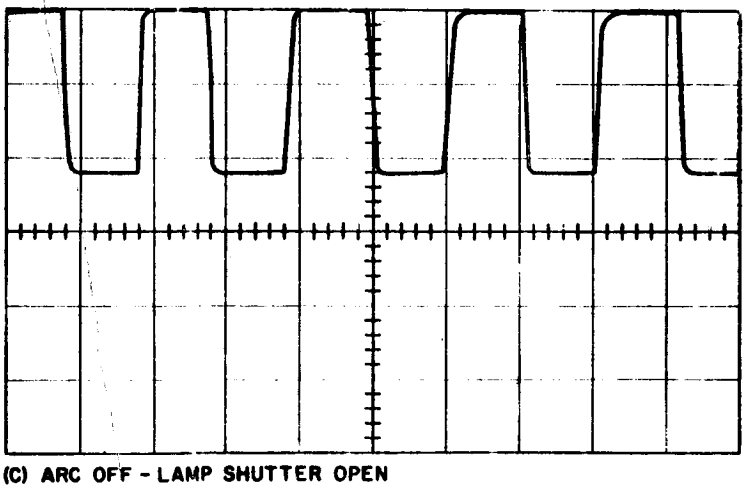

(C) ARC OFF - LAMP SHUTTER OPEN

Fig. 5. Scope traces of probe signals.

(A) The lamp shutter is closed. This signal represents background light from the operating engine.

(B) The lamp shutter is open. The lamp signal transmitted through the exhaust plasma is added to the background light.

(C) The arc is off. This signal represents the light transmitted through the exhaust of the engine with a hot boiler and no arc voltage.

the ambient temperature of the bulb changes. However, the lamp intensity becomes relatively stable after a few hours if the bulb is maintained at constant temperature. After operating about one day the lamp still has a small downward drift in intensity of approximately one percent per hour. This is relatively constant and can be easily measured so that a suitable correction can be applied to all intensity readings.

The coating of the vacuum chamber windows by material associated with the operation of the engine poses a more serious problem. The windows are protected from direct exposure to the engine by the collimator and baffle systems. In addition, shutters are installed next to the inner surfaces of the windows. The shutters are opened only long enough to make a measurement. No noticeable film develops on the windows when these precautions are observed. With the shutters left open a film becomes noticeable after a few minutes of engine operation.

The exhaust of the engine appears as a strong source of radiation of the mercury resonance lines. An appreciable fraction of the light in the exhaust along the optical axis of the probe is able to pass through the slit system and strike the photocathode of the detector producing a background signal. The pulsed lamp signal is seen superimposed on this background. With the engine running at high power level this background light can be very intense and may produce a saturation effect on the phototube. The result is a non-linear response of the phototube to light intensity. The phototube was tested by using the black body radiation from a tungsten filament as a source of background light. A pulsed light signal of constant amplitude from the lamp was superimposed on this background light. These tests have shown that the response of the phototube is quite linear up to light intensities corresponding to a 0.3 mA signal from the anode of the photomultiplier tube if

the photocathode is illuminated for a few seconds or less each 3 minute period. At twice this light level, the deviation of the phototube's response from linearity is less than 10%. (A 0.062 mA background signal is produced by the background light from the electron bombardment ion engine operating with a boiler temperature of 350°F and with a 225 mA beam current.) However, if the photocathode is exposed to intense illumination for times of the order of several minutes the sensitivity of the photocathode changes. In all instances the sensitivity slowly returns to normal if the photocathode is kept dark.

Because of the problems of the coating of the windows and over-exposure of the photocathode it was decided to make all measurements as quickly as possible by photographing the oscilloscope display of the photomultiplier signal. The photographic method does not permit the precision that could be obtained by using the differential comparator. It does, however, permit many measurements with a short exposure time for the windows.

IV. PROPELLANT UTILIZATION MEASUREMENTS

The propellant utilization is determined by measuring the transmission of the 2537A line through the engine exhaust, first with the engine running normally and then with the ionizing and accelerating voltages off. To prevent trapping of mercury vapor the body of the engine is maintained at a higher temperature than that of the boiler. In addition a baffle system has been installed to prevent the backstreaming of mercury atoms from the ion beam collector. The baffles are maintained at liquid nitrogen temperature during the experiment.

The propellant utilization efficiency is given by

$$E = \frac{N_1 - N_2}{N_1}$$

with

N_1 = density of neutral atoms emitted by the engine with the arc and accelerating voltages off

N_2 = density of neutral atoms in operating engines exhaust.

The term density as used here means the area density along the optic line of the probe. This line passes through the center of the exhaust of the engine and perpendicular to the symmetry axis of the engine. It is assumed that the probe makes a representative sampling of the engine's exhaust. This should be true as long as the structure of the exhaust is relatively independent of the arc voltage. The agreement between the optically measured propellant utilization and the gravimetrically determined utilization indicates that this assumption is valid. In any case, this could be checked easily by moving the optic axis of the probe off the center line to give greater weight to the outer regions of the exhaust

beam. The experimental results are given in Table I.

TABLE 1

Boiler Temp.	Plasma Current	Equivalent Single Ion Current	Propellant Utilization Optically Measured	Propellant Utilization Gravimetrically Measured
255°F	50 mA	42 mA	0.69	
270°F	90 mA	77 mA	0.81	
280°F	120 mA	102 mA	0.81	
300°F	115 mA	100 mA	0.95	0.89
302°F	190 mA	165 mA	0.87	
325°F	190 mA	165 mA	0.80	0.83
330°F	170 mA	145 mA	0.40	
342°F	250 mA	212 mA	0.96	

The gravimetric measurement of propellant utilization is obtained by running the engine at a constant boiler temperature for several hours. The mass lost by the boiler divided by the running time is the average rate of emission of atoms. A comparison of this rate to the plasma equivalent single ion current yields the average utilization efficiency.

The boiler temperatures and engine operating voltages were chosen to yield a wide range of absorption values. Consequently, the propellant utilizations shown in Table 1 are not to be considered as optimum or even typical for the boiler temperatures indicated. The reproducibility of a given absorption measurement was better than 5% when the scope display was photographed. This yields an overall uncertainty of about 7% for the propellant

utilization measurement when the transmission of the 2537A line through the exhaust plasma is 0.7 or larger. For the results quoted in Table 1, only one measurement had a transmission below this. With a boiler temperature of 330°F and a low plasma current, transmissions as low as 0.52 were obtained. These poor propellant utilization conditions led to larger percentage uncertainties (12% for the example quoted). More precise measurements may be obtained by using a differential comparator instead of photographing the scope trace.

V. CONCLUSION

The in-line mercury optical resonance probe is a sensitive and reliable instrument for the measurement of the propellant utilization under laboratory conditions. A careful experimenter heeding the precautions mentioned in Section III may obtain reliable and accurate measurements of the propellant utilization even with large plasma fluxes and relatively high background engine light. In addition to permitting accurate measurements to be made quickly, the optical probe may be used to survey the propellant utilization of an ion engine over a wide range of operating conditions. This survey may be made in a short time compared to the gravimetric techniques and with comparable accuracy.

The prospects of using an optical probe similar to the probe discussed in this report on an operating vehicle over extended periods of time do not look promising. The problems of the coating of optical surfaces, of long term stability of the lamp, and of constant sensitivity of the photo sensitive device for a wide range of light intensities over an extended period of time must first be overcome. The solution of these technical problems appears difficult and would probably result in a much more complicated instrument. Therefore the present optical probe appears to be primarily a laboratory instrument.

REFERENCES

1. Cole, R. K., Hall, D. F., Kemp, R. F., and Sellen, J. M., Jr., "Ion Beam Neutral Component Determination by Resonance Radiation Absorption," AIAA Preprint No. 64-9 (January 1964). (Shortened version to be published in AIAA Journal.)

2. Kaufman, H. R. and Reader, P. D., "Experimental Performance of Ion Rockets Employing Electron-Bombardment Ion Sources," ARS Preprint No. 1374-60 (November 1960).

3. Kemp, R. F., Sellen, J. M., Jr., and Pawlik, E. V., "Neutralizer Tests on a Flight Model Electron Bombardment Thrustor," NASA TN D-1733 (1963).

4. Handbook of Chemistry and Physics, (Chemical Rubber Publishing Company, Cleveland, Ohio).

SECTION II.C.

ENVIRONMENTAL EFFECTS ON LABORATORY AND IN-FLIGHT PERFORMANCE OF NEUTRALIZATION SYSTEMS

4137-6016-KU-000

ENVIRONMENTAL EFFECTS ON LABORATORY AND IN-FLIGHT PERFORMANCE OF NEUTRALIZATION SYSTEMS

by

J. M. Sellen, Jr.
TRW Space Technology Laboratories, Redondo Beach, California

and

Ronald J. Cybulski
NASA Lewis Research Center, Cleveland, Ohio

26 January 1965

PHYSICAL ELECTRONICS LABORATORY
Physical Research Division

TRW Space Technology Laboratories
Thompson Ramo Wooldridge Inc.
One Space Park, Redondo Beach, California

4137-6016-KU-000

ENVIRONMENTAL EFFECTS ON LABORATORY AND IN-FLIGHT PERFORMANCE OF NEUTRALIZATION SYSTEMS*

J. M. Sellen, Jr.
TRW Space Technology Laboratories, Redondo Beach, California

and

Ronald J. Cybulski
NASA Lewis Research Center, Cleveland, Ohio

I. INTRODUCTION

The neutralization of the high perveance ion beams required for electrically propelled spacecraft has been a subject of continuing interest in the development of these ion thrustors. This neutralization has been examined in laboratory environments in the earlier experiments, and, more recently, in the first space flight test of an ion thrustor. Effective neutralization of the ion stream has been demonstrated in this latter testing condition as well as in the laboratory experiments. This paper will review environmental effects as they have influenced experiments on ion thrust beams in three particular environmental configurations. These configurations are the small chamber (four-meter) neutralization experiments with the electron bombardment mercury ion thrustor, the large chamber (twenty-five meter) experiments with the contact ionization cesium ion thrustor, and the flight test of the electron bombardment engine on the NASA, SERT-I spacecraft. The discussion will also review some of the diagnostic techniques that have been employed, and will consider further diagnostic techniques, particularly those applicable for space flight tests of ion thrustors.

*This work supported by NASA Lewis Research Center, Cleveland, Ohio, under Contract NAS3-4114.

II. SMALL CHAMBER NEUTRALIZATION EXPERIMENTS: ELECTRON-BOMBARDMENT ION THRUSTOR

The results of the neutralization tests of this electron bombardment thrustor have been described in detail in References 1 and 2, and the discussion here will be primarily concerned with environmental differences between this laboratory testing array and the true space condition. Two of the more obvious features present in the laboratory, and absent in the vehicular space environment, are the conducting boundaries to the vacuum testing chamber and the residual gas within. The conducting boundaries support electric fields through induced surface charges, absorb particles from the plasma stream, and, to some measure, emit secondary particles. The residual gas may interact with the ions and electrons in the thrust beam, with ion-atom charge exchange and electron-atom elastic and inelastic scattering being the principal interaction mechanisms.

The neutralization experiments with the mercury electron bombardment ion thrustor (Kaufman engine) were carried out in a vacuum chamber approximately four meters in length and two meters in diameter. The test configuration is shown in Figure 1. The designation of a "small" chamber is to distinguish this experimental array from the "large" chamber (eight meters in diameter, twenty-five meters in length) configuration to be discussed in Section III. Both the diameter and the length of the vacuum chamber are of interest. The diameter of the chamber provides the radial withdrawal of the chamber boundaries from the plasma beam, with a coupling between the plasma beam and the boundaries which diminishes for an increased chamber diameter. The length of the vacuum chamber, in turn, provides the axial withdrawal of the collecting boundaries from the ion source, and, for increased chamber lengths, increases the time during which the plasma is isolated from the collecting boundaries in the pulsed-beam tests of the neutralization system.

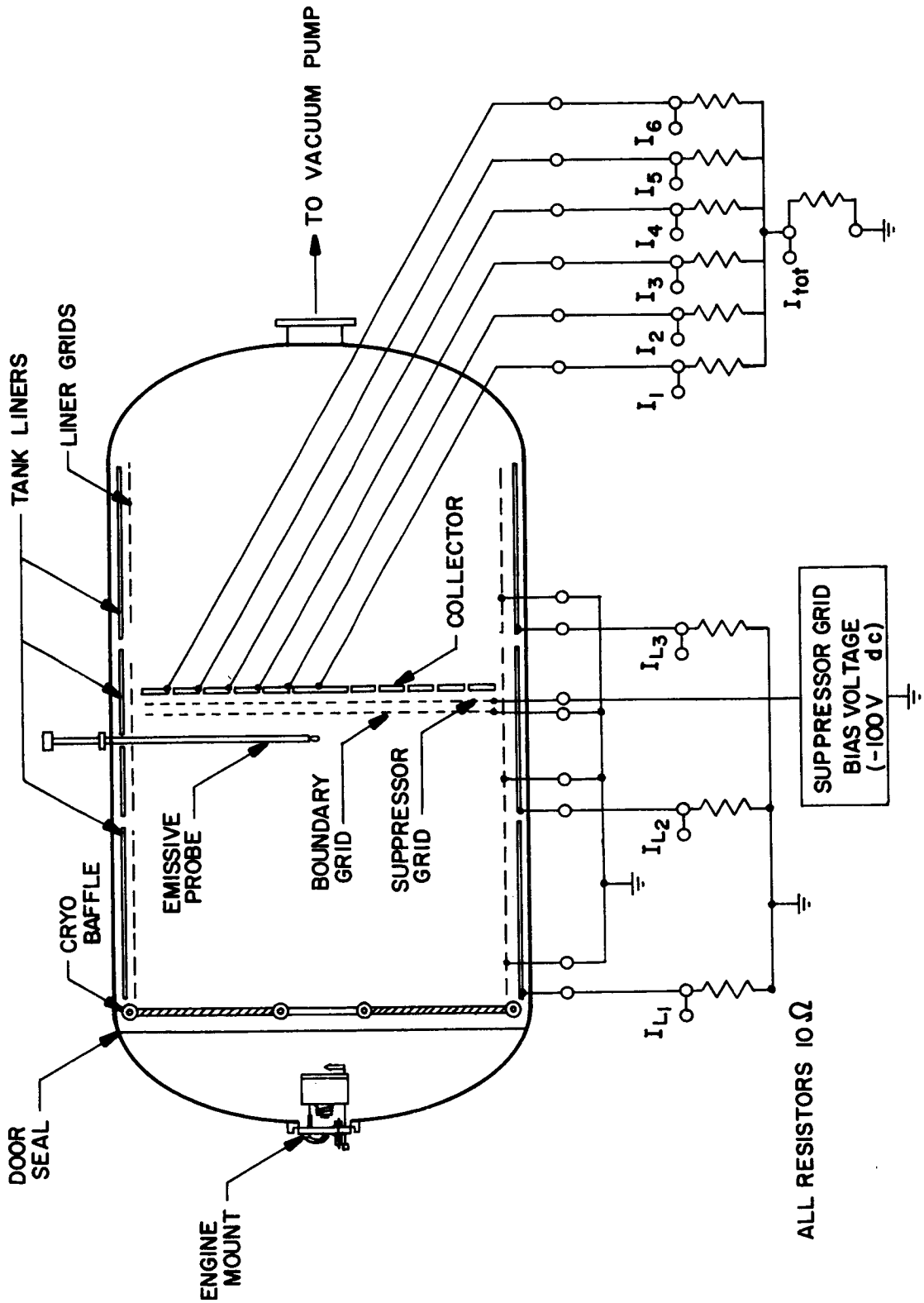

Figure 1. Schematic diagram of 2- by 4-meter vacuum chamber.

The pulsed-beam technique is a method of isolating the plasma thrust beam from its near environment, thereby minimizing the role of the boundaries to the testing chamber. Its initial use is described in Reference 3. A further use of this technique is given in Reference 4. In the pulsed beam studies, the ion acceleration voltage is pulsed on rapidly, and the neutralization of the ion stream is studied during the initial time-of-flight of the ions across the source to collector interspace. During this period there is no direct absorption of particles by the boundaries, so that the role of the surfaces is reduced to, at most, the termination of electrical lines of force from the plasma stream. This "displacement current" contribution is monitored, in turn, by induction grids which line the testing chamber.

The role of the residual gas in the testing chamber may be minimized, or eliminated, through the maintenance of the chamber below the "critical" pressures. The critical pressure in terms of the charge exchange interaction is that at which the mean free path for charge exchange between the ions in the thrust beam and the residual atoms becomes comparable to the source-to-collector spacing. For the charge exchange of mercury ions on mercury atoms, this mean free path is of the order of 4 meters at pressures of 2×10^{-5} Torr, and for lower chamber pressures than this, the charge exchange interaction is of diminishing importance. The "critical" pressure in terms of electron-atom elastic scattering interactions is that at which the mean free path for large angle scatterings becomes of the order of the dimensions of the plasma stream. For scattering cross sections of the order of 10^{-16} cm^2, this mean free path is of the order of 1 meter at 3×10^{-3} Torr. The critical pressure in terms of electron-atom inelastic collisions is somewhat

less well defined but would, presumably, be that pressure at which energy loss rates for electrons in these collisions become comparable with the rates of energy losses (or gains) from ion-electron interactions in the plasma stream. There has not been, however, a thorough experimental examination of the energy interchange mechanisms between ions and electrons in these plasma thrust beams. In the experiments to be discussed in Section III, the electron-ion interaction appears to lead to a rapid cooling of the electrons after their injection into the ion stream. If this condition should hold true generally, then the pressure requirements in terms of these inelastic interactions are less stringent than those of charge exchange and elastic scattering.

In the experiments detailed in References 1 and 2, the chamber pressure was maintained at 1×10^{-5} Torr or less. At full beam currents of $\sim$ 400 milliamperes, the use of large liquid nitrogen cooled cryopumping surfaces was required to hold the chamber pressure in the range below this figure of 1×10^{-5} Torr. From this, it may be seen that any substantive interaction between the plasma stream and the residual gas has been eliminated, and the reduction of the pressure to the residual backgrounds in space should not produce any significant variations in the observed behavior of the thrust beam.

The electrical interaction between the plasma beam and the chamber boundaries was similarly small and may be neglected. For those sections of the plasma column near the ion source, the capacitance per unit length between the plasma beam and the chamber walls is $\sim$ 20 $\mu\mu$F/meter, leading to an induced charge of 20 $\mu\mu$-coulombs/meter/volt of potential difference between the plasma column and the boundaries. For a full beam current of 400 milliamperes at 2500 eV ion energy, the positive charge per unit length in the plasma beam is 8×10^{6} $\mu\mu$-coulombs/meter. By

proper adjustment of the plasma potential, it is possible, thus for the induced charge along the boundaries to become $\sim 10^{-5}$ of the magnitude of the ion and electron charge colonies in the plasma stream. In the regions downstream from the ion source, this isolation is less complete, because of the outward divergence of the plasma column (from electrostatic lens effects in the ion acceleration region). This radial spreading of the ion beam diminishes the separation from the plasma to the boundaries with a corresponding increase in the capacitance between the thrust beam and the vacuum chamber walls. However, by using a chamber of moderate diameter, the induced charge per unit length remains less than 10^{-3} of the ions and electrons per unit length in the plasma column, even in these downstream, diverged beam regions.

The results of the neutralization tests with the mercury electron bombardment thrustor, taken from Reference 2, are shown again in Figure 2. For the neutralizer configuration which was later used in the space flight test, the plasma potential, measured at a downstream point, was $\sim$ 9 volts positive with respect to the neutralizer. These potential differences are taken from emissive probe data, with an accuracy of measurement of $\sim$ 0.5 volt in that experimental condition. Significantly, there were no observable differences between the pulsed beam operation of the neutralizer and the steady-state condition which one obtained when the plasma beam was directed against a floating collector. For neutralizers that are withdrawn from the plasma column, observable differences do occur between these two periods, but for totally immersed (and thus, tightly coupled) neutralizers, the behavior is identical in the two testing conditions. This is further evidence, then, of a neutralization system which is well-coupled to the plasma stream.

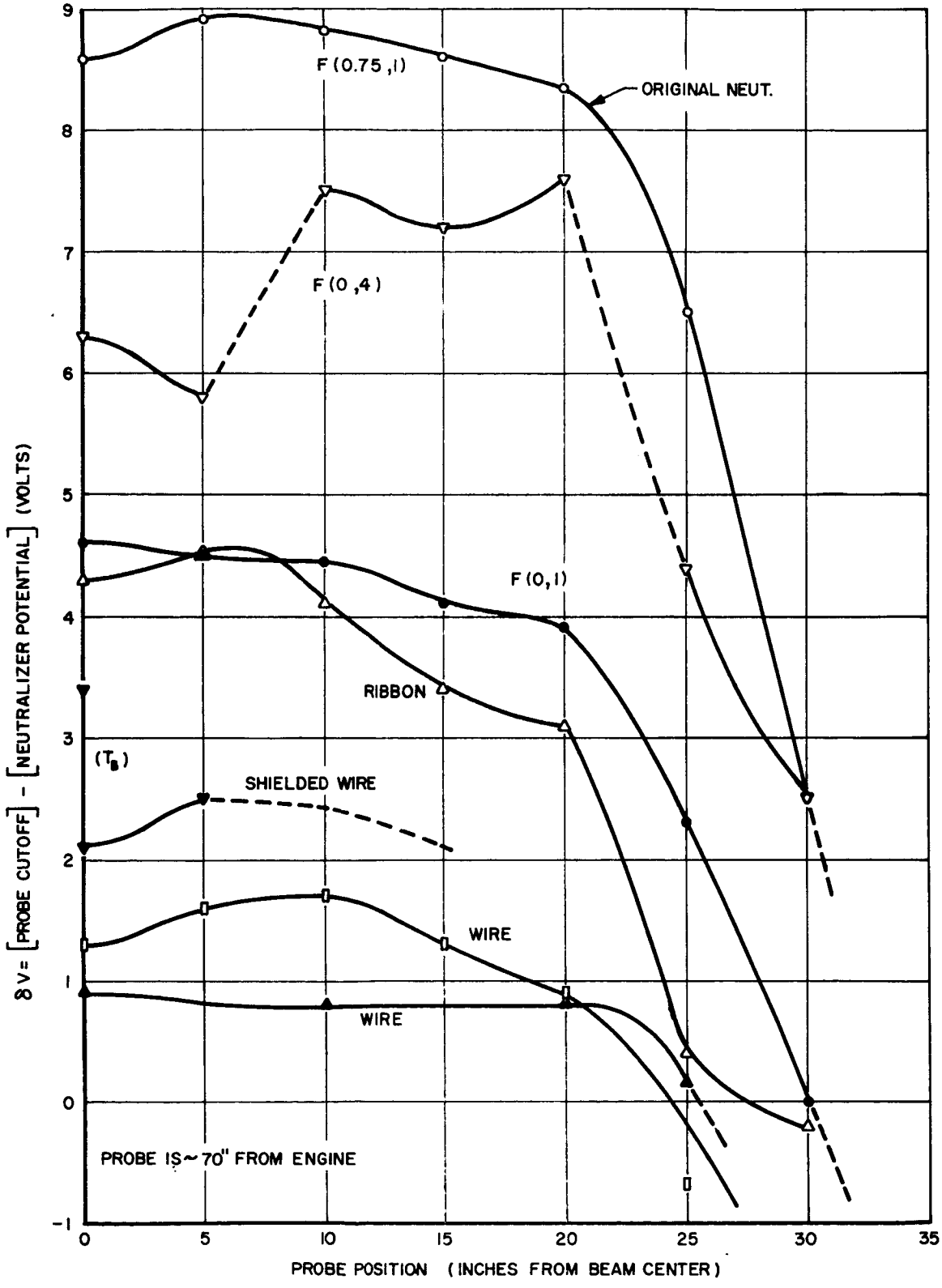

Figure 2a. Emissive probe measurements of plasma potential relative to that of the neutralizer as a function of the variable position neutralizer. The probe is on the axis of the beam, 70" downstream.

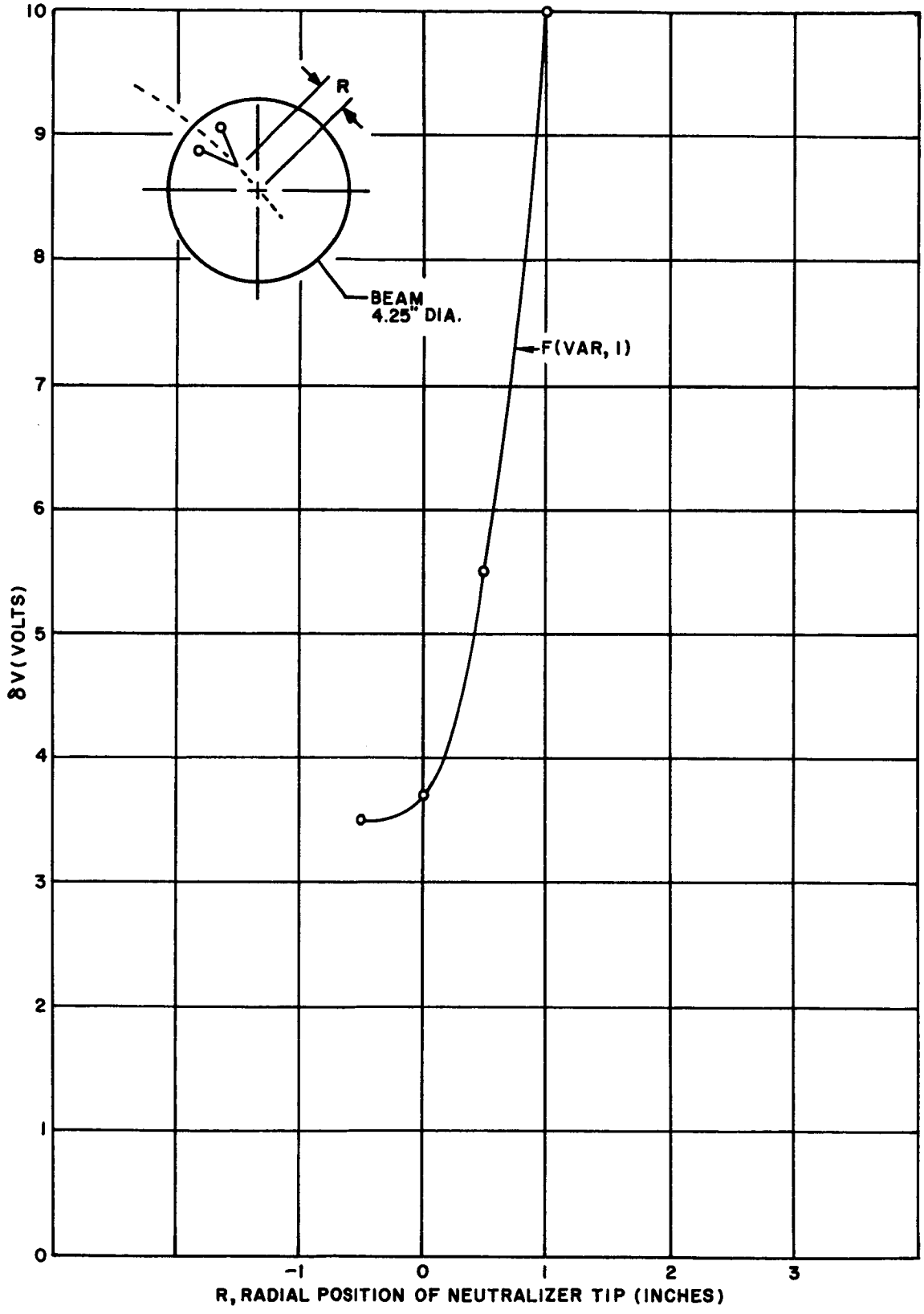

Figure 2b. Emissive probe measurements of plasma potential relative to that of the neutralizer as a function of position of the variable position neutralizer. The probe is on the axis of the beam, 70" downstream.

In view of the intimate coupling between the neutralizer and the plasma beam, and in view of the very minor involvement of the chamber boundaries and the residual gas in the behavior of the plasma beam, there is no a priori reason to consider that the neutralization of the thrust beam would be affected if the chamber walls were removed to infinity and the chamber residual gases reduced to the almost total vacua of space. There are, however, limitations in this small chamber experiment relative to a true space test. The most notable is that the plasma column is isolated from its laboratory environment for periods of the order of 200 μsec or less, and, if some particular relaxation processes do occur over longer periods, they would not have been observable in this four-meter geometry. Beyond this, there are other factors such as the absence, in the testing chamber, of the dilute residual plasmas which exist in the near regions of the earth, and the more complicated general interaction between the plasma thrust beam and the magnetic field of the earth, when the thrust beam is exhausted from a moving vehicle. While these latter factors are not easily amenable to laboratory simulation, the extension of the isolation time of the plasma column from its vacuum testing chamber may be carried out through the use of larger testing facilities. These experiments, in the large testing chamber at Lewis Research Center, were carried out subsequently and their results are discussed in Section III.

III. LARGE CHAMBER NEUTRALIZATION EXPERIMENTS: CONTACT IONIZATION CESIUM ION THRUSTOR

The large testing chamber at NASA Lewis Research Center, Cleveland, Ohio has a diameter of ~ 8 meters and a length of ~ 25 meters. For a pulsed beam experiment, this chamber length

would provide, for nominal ion accelerating voltages, an isolation time almost an order of magnitude larger than that attained in the smaller chamber experiments discussed in Section II. Relaxation processes in the millisecond range would be observable, if, indeed, processes with these long time constants should exist in these plasma columns.

Because the diagnosis would be directed at the possible existence of second-order variations in the plasma column behavior as functions of the plasma column length, a contact ionization source was selected for the ion beam generation. The experiments are an extension of the earlier tests described in Reference 3. The plasma produced by the contact ionization source is highly quiescent, and measurements of plasma potential and electron temperature may be performed with an accuracy which is subject only to the inherent limitations of the diagnostic instruments. For potential measurements with emissive probes, this accuracy is of the order of 0.01 to 0.03 volts in the plasma density region above 10^7 ions/cm^3 (Reference 5), while the Langmuir probe accuracy in the measurement of electron temperatures is estimated at $\sim$ 200°K. The ion source perveance was $\sim$2000 nanopervs, so that the neutralization experiments were conducted with a "broad" beam, high perveance thrustor. Neutralization was by an immersed hot wire.

The experimental array used in these large chamber experiments is shown in Figures 3 and 4. These figures are drawn from Reference 6, which presents, in detail, the results of the experiments. The important aspect of these tests, applied to the present discussion, was the invariance in the plasma behavior through these longer isolation periods. The potential, the density, and the electron temperature at a fixed probe location in the plasma column exhibited no observable timewise

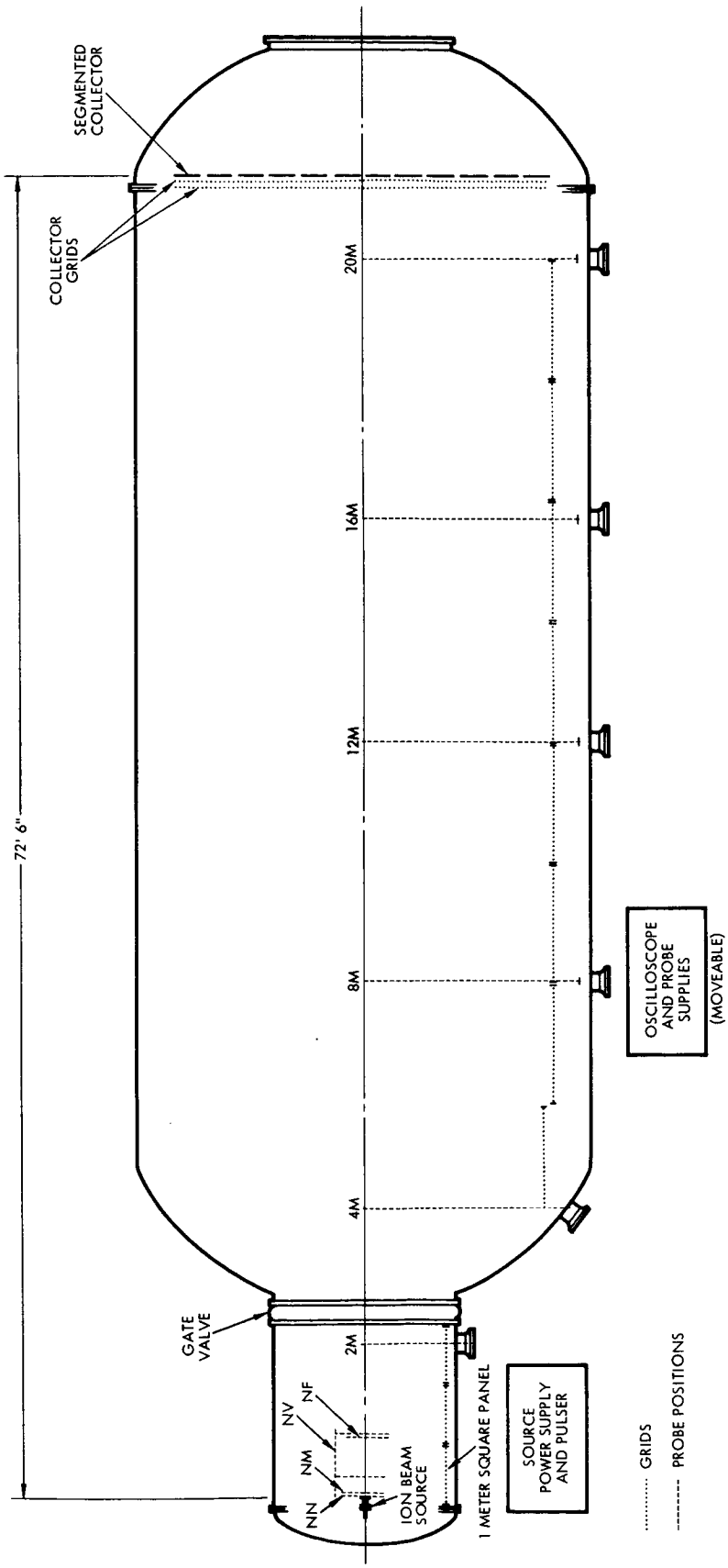

Figure 3. A sketch of the chamber showing the locations of the source, collectors, grids, and probe packages. Probe locations comprise two groups -- a near group, (NN, NM, NF, and NV) and a downstream group identified by nominal distances from the source in meters. Actual measured distances are given in the table below.

Probe	Distance (meters)
NM	0.011
NM	0.114
NF	0.984
NV	0.01 to 1.07
2M	2.48

Probe	Distance (meters)
4M	4.81
8M	8.22
12M	12.21
16M	16.02
20M	20.30

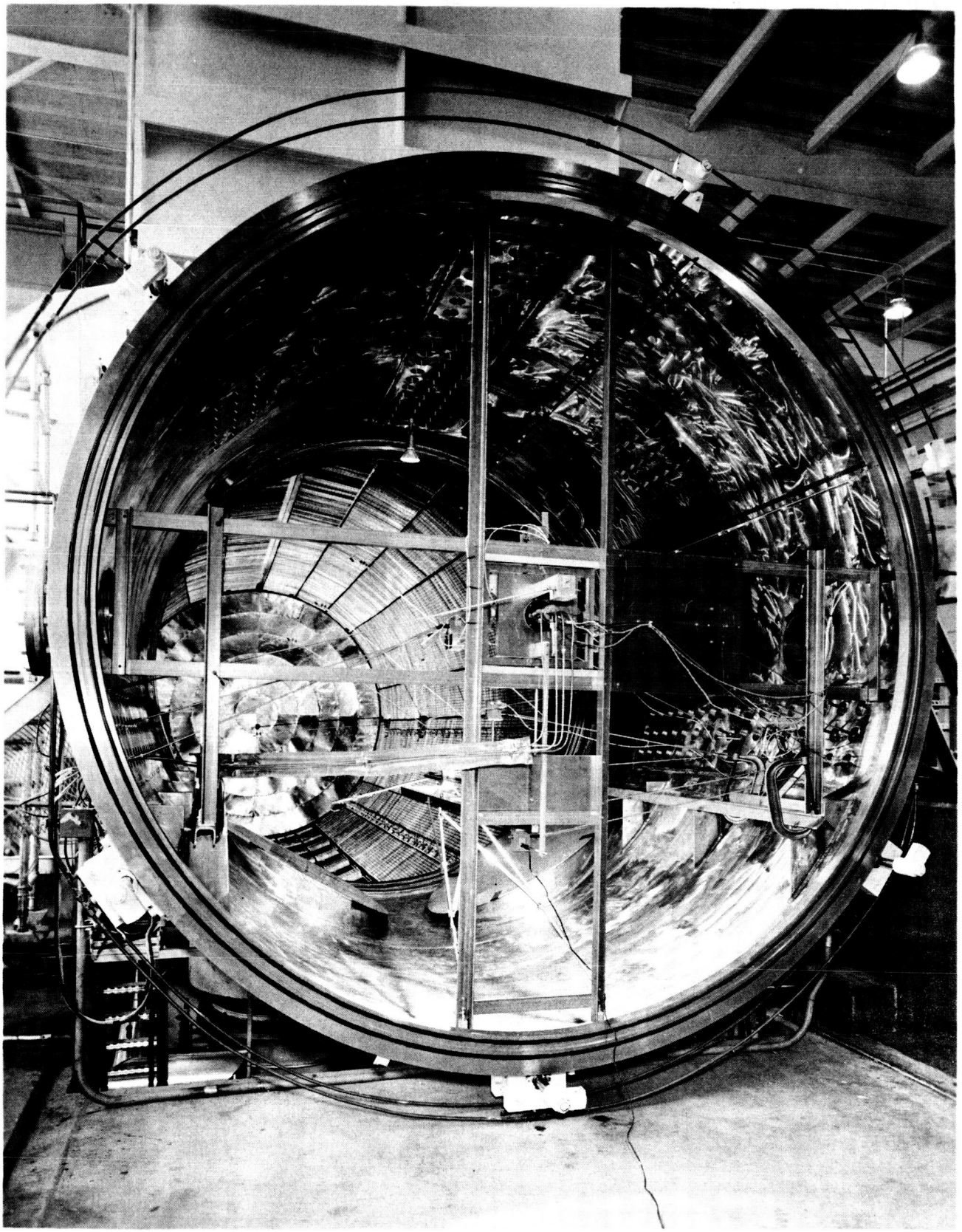

Figure 4. A view through the "bell-jar" section into the interior of the testing chamber. Downstream probe packages are mounted at the end of booms which are swung from side ports. In the foreground center is the source mounting plate.

variations as the plasma front moved further downstream from the probe. For those probe locations near the ion source, the time interval from the arrival of the plasma front at the probe until the plasma arrived at the collector at the far end of the chamber is > 1 millisecond. This result then confirms that there are no significant relaxation processes with characteristic times of the order of a millisecond.

The plasma columns obtainable even in this testing configuration are not, of course, those infinitely long columns that will be obtained in the vehicular space environment. They are of great enough length, however, for the ion density within the plasma column to have diminished to values comparable to the ambient plasma densities in the ionosphere. For the average ion beam divergence angle of $\sim 3°$ in these cesium ion beams, the plasma density diminishes from $\sim 10^{10}$ ions/cm^3 in the source region to $\sim 10^6$ ions/cm^3 at points of the order of 20 to 25 meters downstream. Such a beam, then, would have almost merged into the ambient plasma of the F2 layer (Reference 7). For regions of greater altitude, this ambient plasma density diminishes, requiring a longer column length for the thrust beam plasma to merge with the space plasma. These merging points, however, would differ by only an order of magnitude for a wide range of vehicle altitudes, and the existence of very effectively neutralized plasma columns in this present testing geometry is strong evidence that the effectiveness of the neutralization would not be, in any way, diminished in the infinite geometries of space. The conclusive evidence, of course, would be supplied through a vehicular space test of an ion engine.

IV. NEUTRALIZATION EXPERIMENTS IN SPACE: SERT-I ION ENGINE TEST

The SERT-I spacecraft was launched on July 20, 1964 from Wallops Island, Virginia. This flight test was under the direction of NASA, Lewis Research Center. The four stage Scout launch vehicle boosted the payload into a ballistic trajectory with a peak altitude of ~ 2100 nautical miles and with a total flight time of ~ 40 minutes above 250 nautical miles. The spacecraft possessed both a cesium contact ionization thrustor and an electron bombardment mercury ion thrustor. The electron bombardment thrustor was identical to that thrustor which was tested in the experiments described in Section II, and it is the neutralization behavior of this thrustor that will be discussed in this section.

A detailed treament of the flight package and of the space flight results is given in References 8 and 9. The discussion here will review briefly the methods by which the thrust and the beam power were determined, and will then consider, in more detail, the information furnished by the rotating-vane electric field strength meter.

IV.A. THRUST AND BEAM POWER MEASUREMENTS

The SERT-I spacecraft is shown in Figure 5. The payload was spin stabilized with the spin induced by the fourth stage rocket. After the deployment of the ion thrustors, the spin rate of the vehicle was ~ 90 revolutions per minute about the spin axis. This spin rate was measured by two separate solar detectors. The initial precession angle was small, and further damping occurred during the flight period.

The thrust of the electron bombardment engine acted to increase the spin rate of the vehicle. The measured change in

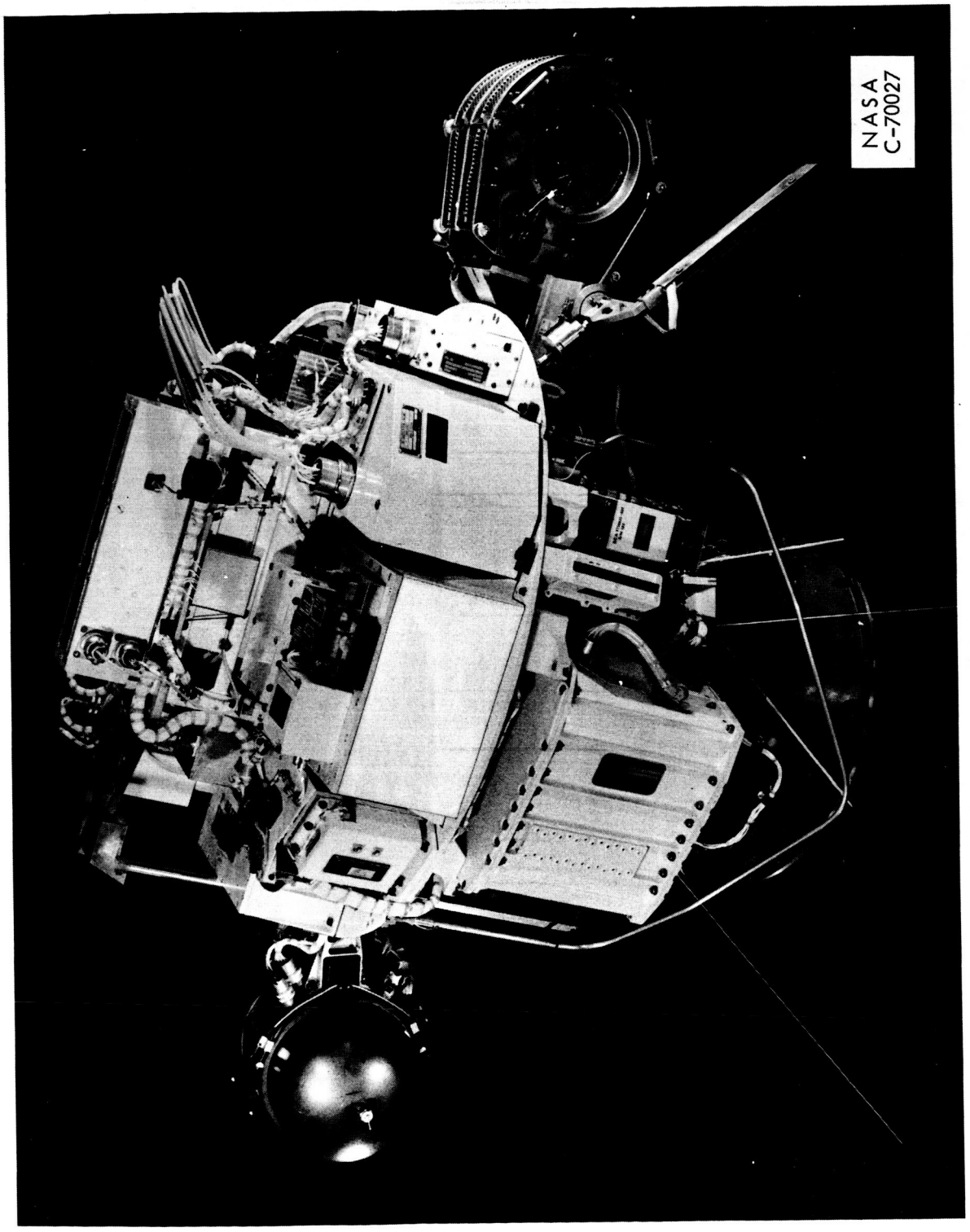

Figure 5. Free flight configuration of the SERT-I spacecraft.

the spin period of the vehicle from the solar detectors, together with the known moment of inertia of the vehicle about the spin axis and the known moment arm of the thrust beam about the spin axis were used in the calculation of the engine thrust. A further measure of the angular acceleration of the vehicle from a radial accelerometer allows an additional determination of the engine thrust. The peak value of this delivered thrust was 6 millipounds, and the total increment in the vehicle spin was 10 rpm.

The measured parameters of the ion thrustor include discharge current and discharge potential in the electron bombardment chamber, arc chamber magnetic field current, ion acceleration voltage, total ion source current, accelerator drain current, and neutralizer current. From these measured currents and voltages, the deliverable thrust from the ion engine, assuming perfect neutralization, may be calculated. With suitable corrections for the fraction of doubly charged ions, the average divergence angle of the accelerated ions, and spurious drain currents from the neutralizer to the ion source region (Reference 9), this calculated thrust, assuming perfect neutralization, is in agreement with the measured values of the thrust within 5%.

This close agreement between the calculated and measured values of thrust is conclusive evidence that ion beams can be effectively neutralized in the infinite geometries of space. The quantity which is specifically determined by this experiment is illustrated in Figure 6, and is the net ion acceleration velocity, $\left(\frac{2e(V_o-V_p)}{M_+}\right)^{1/2}$ where V_o is the ion source voltage and V_p is the potential in the plasma thrust beam. The

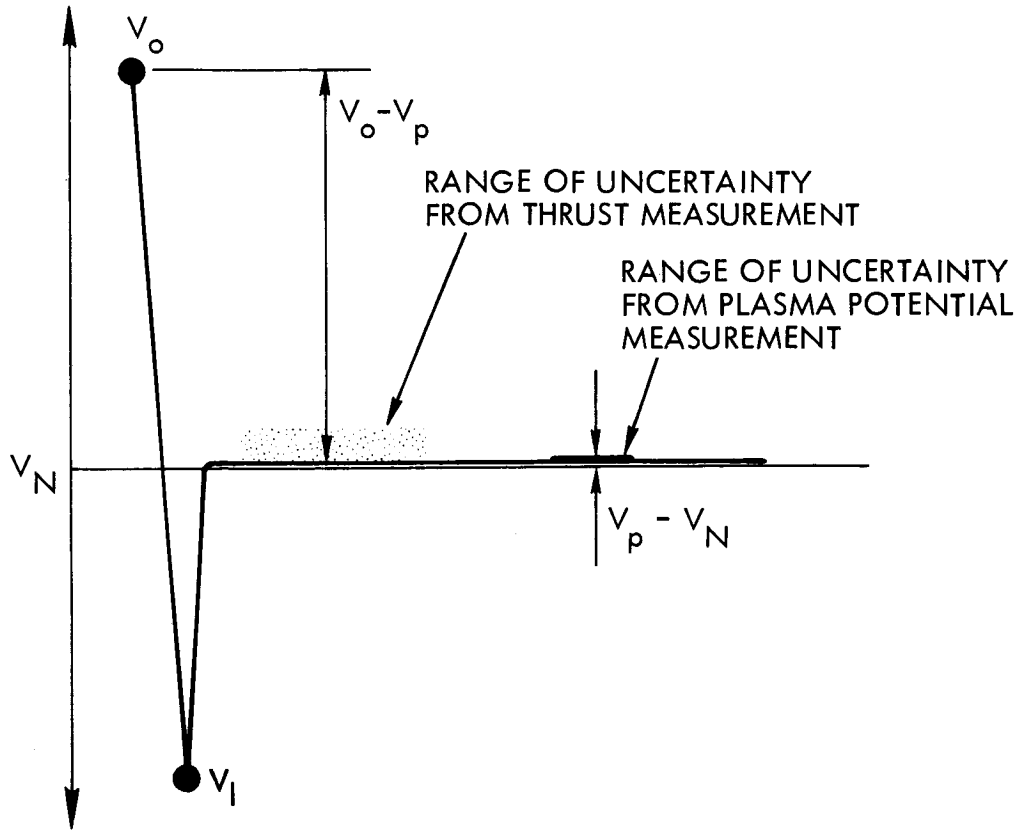

Figure 6. Flight test measurements of thrust determine ion acceleration velocity $\left[2e(V_o - V_p)/M_+\right]^{1/2}$ from which $(V_o - V_p)$ is derived. Laboratory plasma potential measurements determine $(V_p - V_N)$.

possible 5% difference in measured and calculated thrust leads to a possible range of $\sim$ 10% in the net ion acceleration energy, $e(V_o - V_p)$. For the ion source voltage employed of 2.5 kilovolts, this 10% range corresponds to a possible range of $\sim$ 250 volts in the potential of the plasma relative to the neutralizer. In the experiments described in Section II, this plasma potential has been determined by emissive probe measurement to $\sim$ 0.5 volt, so that the space flight data, though it provides an assurance

that the neutralization is perfect within, at most, effects of second order, does not act as a direct check against the laboratory measurements of plasma potential. Instruments which will provide such a direct check for in-flight performance are discussed in Section V.

A further check upon the effectiveness of the ion beam neutralization is provided by the hot-wire power density probe measurements. This probe, described in Reference 10, provides a two dimensional map of the ion beam power density in the ion thrust beam. The total beam power measurements from this probe agree with the calculated total beam power, assuming perfect neutralization and correcting for spurious circulating currents, within $\sim$ 5%. Again, this technique provides a measurement of the effective ion acceleration potential, $(V_o - V_p)$, and, confirms that, to within second order effects, the ions acquire the energy that they would attain for perfect neutralization. The accuracy of the measurements does not, however, provide a check of the measured quantity, $V_p - V_N$, described in Section II.

The diagnostic measures reviewed thus far are not regarded as sensitive to particular conditions of the space environment. The signals from the rotating-vane E-field meter are, however, sensitive to some of these influences. These space conditions and the E-meter signals are discussed in the section which follows.

IV.B. ROTATING VANE ELECTRIC FIELD STRENGTH METER

1. General Considerations

The rotating-vane E-field meter consisted of 3 stationary vanes which were alternately shielded and exposed by a set of 3 similar vanes which rotated at 8000 rpm. The instrument is similar to that described in Reference 11. The induced

current which flows to the surface of the stator vanes if an electric field is present on the surface of the vehicle provides a 400 cps signal which is amplified by a solid state AC amplifier and then commutated into the telemetry unit. For this vane rotation speed, the induced current density is 3.5×10^{-11} amperes/cm^2 for an imposed electric field strength of 1 volt/cm. For the amplification provided on the most sensitive scale, the minimum field strength that may be detected is $\sim$ 2 volts/cm.

The rotating vane E-meter is sensitive to some effects which may occur even in the laboratory environment. One such effect arises if a contact potential difference exists between the forward surface of the stator vanes and the back surface of the rotor vanes. For a vane spacing of 3 mm, a contact potential of 1 volt between these two surfaces would produce an effective field strength of $\sim$ 3 volts/cm when the stator vanes are shielded by the rotor. For the SERT-I E-field meter, these vanes are gold plated to minimize such contact potential fields. However, it is possible for these fields to exist, and conditions under which they have been generated are described in Section IV.B.4.

Of more general concern is the difficulty in relating the potential of an isolated vehicle to the surface field strength indicated by the meter, if the vehicle is within the dilute plasmas near the earth. If a vehicle is within a perfect vacuum, the vehicle potential is $V_s = E_s r_s$, where E_s is the surface field strength and r_s is the radius of the (spherical) vehicle. If the vehicle is in a dilute plasma, the near termination of lines of electric force upon plasma particles, rather than at infinity as in the perfect vacuum case, causes a higher electric field strength to exist for a given vehicle potential. The correction factor for this effect may be almost

an order of magnitude for small vehicle potentials and relatively dense ambient plasmas, such as those encountered in the F2 layer. Values of this correction are given in Reference 12 for a series of densities and kinetic temperatures in the ambient plasma. For large vehicle potentials, the sheath region surrounding the vehicle becomes very large, and the correction terms diminish.

A further difficulty created by the presence of the ambient plasma occurs when the velocity of the vehicle begins to exceed the thermal velocities of the ions in the space plasma. For vehicles in the lower portions of the ionosphere, the condition $v_s >> v_+|_{thermal}$ generally exists. For such a circumstance, a wake structure exists about the vehicle and the sheath dimensions and electric fields may vary significantly from one portion of the vehicle to another. This condition is illustrated in Figure 7. Under such a condition, an E-meter on

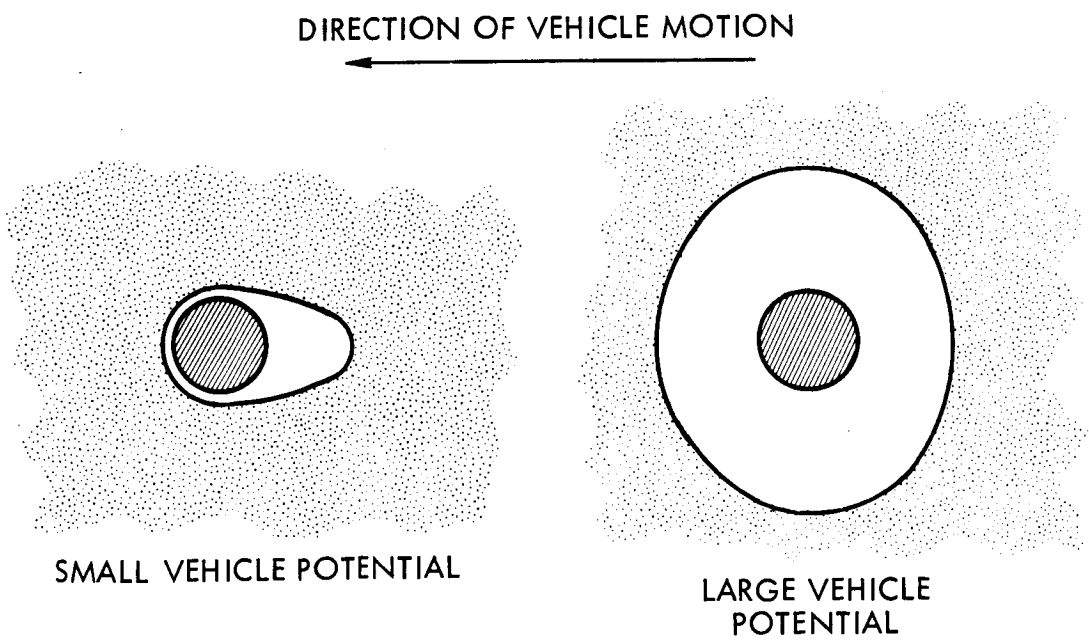

Figure 7. Sketch of vehicle sheath configuration for "small" and "large" vehicle potentials.

a vehicle which possesses both a spin and a motion through the plasma, would sense a time-varying electric field, even for a fixed vehicle potential. Examples of these sheaths and electric fields are also given in Reference 12.

A final effect from the presence of a dilute space plasma is the current of charged particles which may flow from the plasma to the vehicle skin. These currents are complicated functions of the vehicle potential, plasma density, plasma thermal energies, and vehicle motions relative to the plasma (Reference 12). For small negative vehicle potentials, the current density of ions from the plasma to the forward portions of the vehicle is $\sim \rho_+ v_s$, where ρ_+ is the space plasma density and v_s is vehicle velocity. This would lead to currents of 10^{-7} amps/cm^2 for the denser regions of the F2 layer. In this same F2 region and for small positive vehicle potentials, the current of electrons may be $\sim 10^{-6}$ amps/cm^2, because of the greater electron mobility. Large vehicle potentials relative to the space plasma tend to increase the magnitudes of these currents still further. It is important to note that, under particular conditions, these particle currents from the ambient plasma may exceed, by many orders of magnitude, the induced current density due to electric fields of the order of a few volts/cm. For this reason, a signal from the E-meter may be, predominantly, the result of real particle currents and not the result of the displacement currents associated with the surface electric field. For the SERT-I E-field meter, the sensitivity to these particles was diminished by a factor of $\sim$ 10 through the use of gridded stator vanes. Tests relating to the E-meter behavior when particle currents are being delivered to the stator vanes are reviewed in Section IV.B.4.

One further environmental factor which may affect the E-meter behavior is the solar ultra violet radiation. Any photoelectrons liberated from the stator vanes would contribute to the overall current signal treated by the amplifiers. For a solid stator and rotor vane construction, this photoelectric signal should be easily describable, being suppressed for a positive vehicle potential, being present for a negative vehicle potential, and being absent from any areas of the stator vanes in the rotor vane shadow. The circumstances for a gridded stator vane placed before a solid backing plate and with a gridded rotor vane are much more involved as is illustrated in Figure 8. Because of these complications, the E-meter response to UV radiation was examined experimentally. These tests are also reviewed in Section IV.B.4.

IV.B.2. OBSERVED E-METER SIGNALS: FLIGHT DATA

There are four particular periods during the SERT-I space test in which the E-meter signal will be discussed. These are:

1. Thrust beam off.
2. Thrust beam on, no neutralizer bias, upper part of trajectory.
3. Thrust beam on, neutralizer biased positive with respect to vehicle skin, upper part of trajectory.
4. Thrust beam on, no neutralizer bias, re-entry portion of trajectory.

The E-meter signal from these four periods is shown in Figure 9. Several features are prominent. During the first period there is, essentially, no signal from the E-meter. During the second period the signal is observable and is periodically fluctuating. During the third period the E-meter signal is non-fluctuating

SOLID VANE

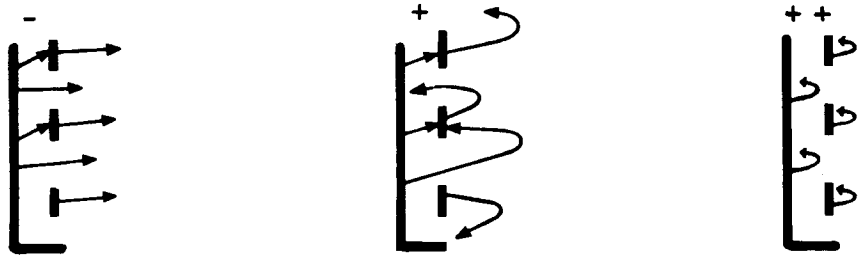

GRIDDED VANE

Figure 8. Possible photoelectric currents from solid and gridded stator vanes for positive and negative vehicle potentials. Strongly positive potentials indicated ++.

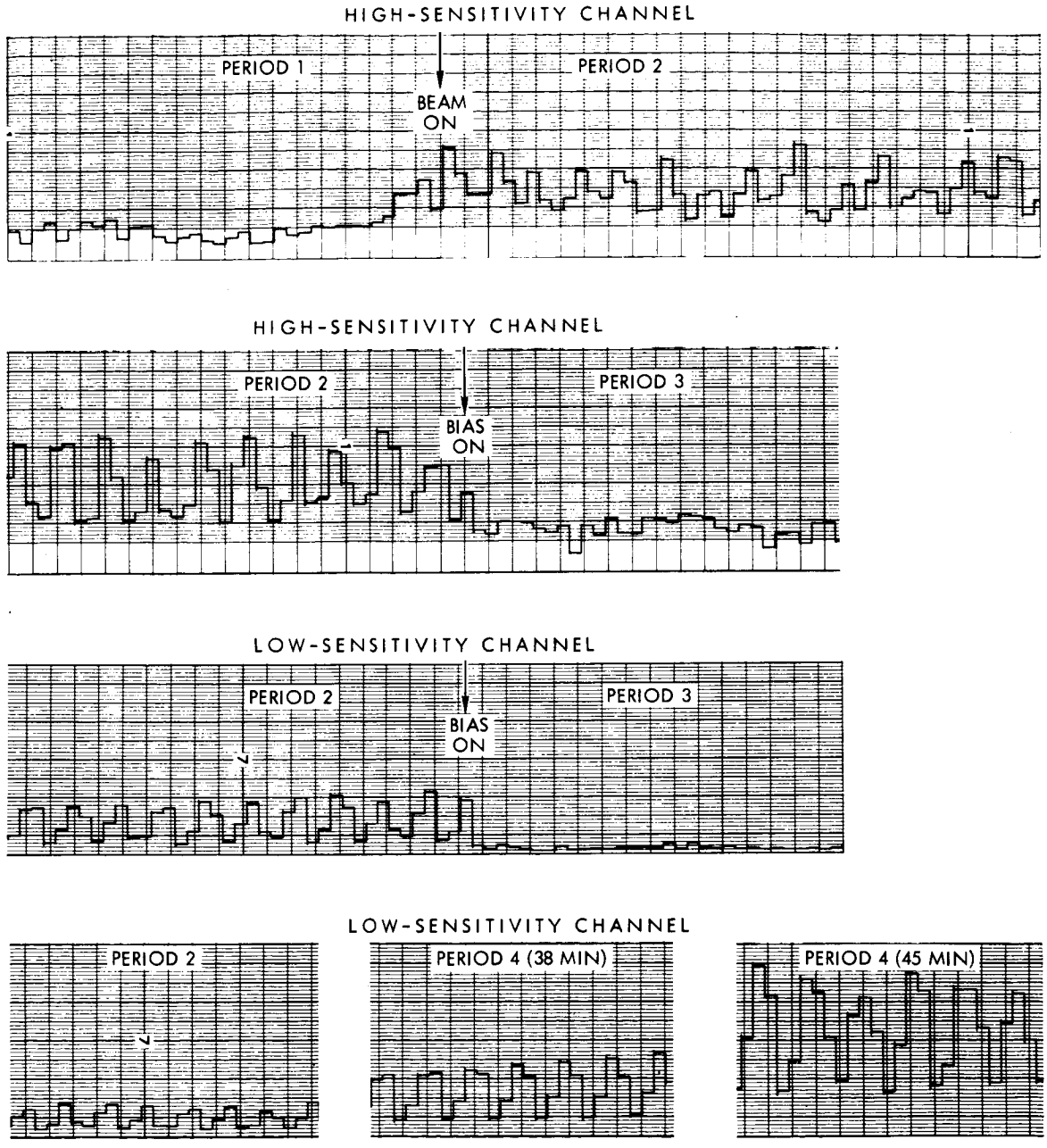

Figure 9. E-field meter signals during periods 1 to 4 of the SERT-I space flight test. One horizontal division equals 1 second. Full scale is 10 vertical divisions. Indicated times in period 4 are measured from launch. Data in period 2 are at approximately 20 minutes after launch.

at ~ 0.1 of full scale amplitude on the high sensitivity scale. Finally, in the fourth period, the signal is again fluctuating and is increased in its magnitude from that of the second period.

When the E-meter signal is examined relative to the rotation of the vehicle, it is found that the fluctuating signals in the second and fourth periods have a component of the same period as the vehicle rotation (Reference 13). The dependence of this signal as a function of the orientation of the vehicle is shown in Figure 10. From these data the E-meter signal may be characterized as "beam dependent," being in existence for those periods when a thrust beam is generated by the thrustor, and, for those periods in which no neutralizer bias exists, as "spin dependent," also, having the period of the vehicle rotation.

IV.B.3. ENVIRONMENTAL EFFECTS: FLIGHT OPERATION

The environmental effects discussed in IV.B.1 may now be examined as they may have contributed to the flight data from the E-meter. In addition, there are other factors, due to the presence of the thrust beam, that should be considered. These several effects are listed in Table I. The vehicle rotation period is indicated there as T_s.

Table I.

Effect	Spin Dependent Signal	Period
Solar photoelectric	Yes	T_s
Variations in sheath thickness	Yes	T_s
Plasma collection currents	Yes	T_s
$\vec{V}_+ \times \vec{B}$ forces	Yes	$0.5\ T_s$
Thrust beam-resident plasma interaction	No	--

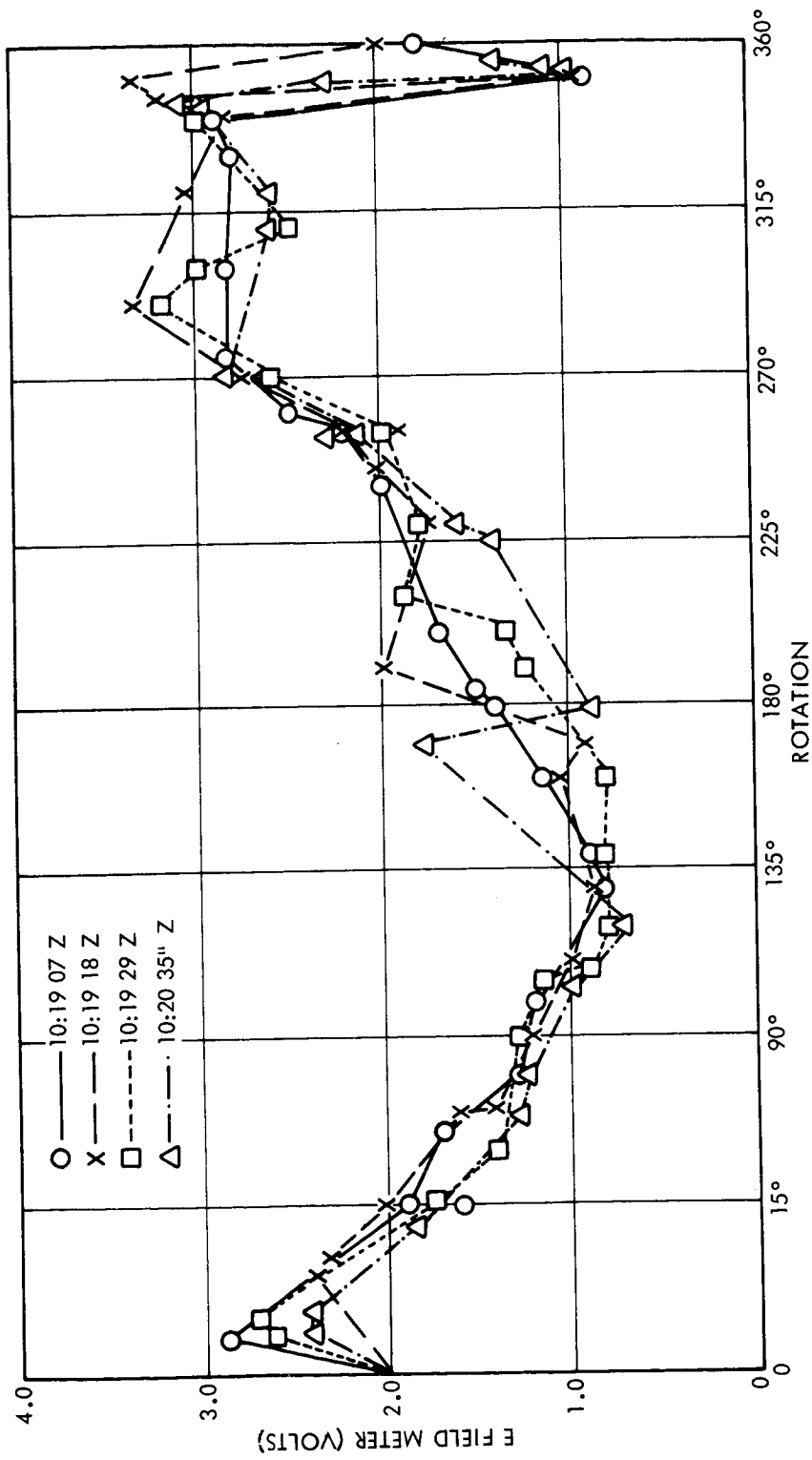

Figure 10. E-field meter signal (4V = full scale) for high sensitivity channel as a function of vehicle orientation. Rotation angle = 0° for solar sensor facing toward the sun. The E-meter faces toward sun at rotation angle of ~ 160°. Indicated sampling periods are indexed by Greenwich time and correspond to period 2 of the SERT-I flight.

The solar photoelectric currents would produce a spin dependent signal with a definite phase relationship to the solar sensor signal from which the vehicle rotation speed is determined. Particular conditions of vehicle potential could suppress these photoelectric currents, thus eliminating the solar UV as a contributor to the spin dependent signals that have been observed. Variations in the sheath thickness would appear for small vehicle potentials and for vehicle speeds in excess of the ion thermal velocities in the ambient plasma. These variations in sheath dimensions would diminish for increased vehicle potentials and for diminished plasma densities. Plasma collection currents would increase for increased vehicle potentials, but the variations in these currents to an E-meter for a vehicle with a large potential would tend to diminish as the sheath dimensions increased and became more symmetric about the vehicle.

The remaining effects have not been previously discussed, and are, for the most part, conjectural. One of these possible interactions is denoted as "$\vec{v}_+ \times \vec{B}$ forces." In the experiments in Reference 14, potential gradients along the axis of the plasma stream were observed when the beam was directed against a transverse magnetic field. In the vehicular experiment, these gradients could result in a fluctuating potential at the injection region of the column (assuming that the far downstream portions of the plasma column must match to the potential of the ambient plasma), which, in turn, could cause the vehicle potential to exhibit a spin-dependent fluctuation. The period for the fluctuation in this instance would be $0.5\ T_S$.

A final possible interaction, between the thrust beam and the resident plasma, should not cause any spin-dependent fluctuations in vehicle potential, since the ambient plasma

should be isotropic except in the very near neighborhood of the vehicle. A spin-dependent E-meter signal could result from the interaction between the thrust beam and the ambient plasma, however, if that interaction resulted in the collection, at the vehicle surface, of currents from the ambient plasma. Such a condition might arise, for example, if currents of secondary electrons from the ion accelerator plate enter the plasma thrust beam. Because of their large energy (several keV), these electrons are not "bound" to the plasma column as the electrons from the neutralizer are, and they very rapidly leave the thrust beam and are lost in the adjoining ambient plasma. Thus, even though the neutralizer might be capable of perfect neutralization of the thrust beam, an imbalance in the overall currents leaving the vehicle could result. The resultant small positive shifts in the vehicle potential would extract a net current of electrons from the space plasma in order to balance this extraneous current of fast secondaries leaving the accelerator plate. Indeed, any condition which results in a vehicle potential other than the floating potential for the passive vehicle could result in a spin-dependent current collection signal from the E-meter.

Throughout the discussion it has been assumed that there are no direct currents between the ion engine and the E-meter. This has been assumed because the ion engine and the E-meter are well removed from each other on the spacecraft, and because the thrust beam is directed at 180° to the normal to the E-meter.

Of the several possible effects presented in the table above, the photoelectric currents and plasma collection currents could be tested in laboratory experiments. These are reviewed in the section which follows.

IV.B.4. E-FIELD METER TESTS

An E-field meter, identical to that instrument flown on the SERT-I flight, was subjected to a series of laboratory tests. These tests included the response of the meter to static and time-varying electric fields, to plasma particle currents, and to ultraviolet radiation. The experiments are described in Reference 15, and will be reviewed, in part, in this section.

The dc field response was similar to that which was supplied with the flight instrument, providing a full scale output signal for ~ 30 volts/cm and ~ 90 volts/cm on the high sensitivity and low sensitivity channels, respectively, Primary attention was directed, however, toward the response to time varying fields. Small amplitude fields, from 0.05 cps to 15 cps were imposed on the meter, with circuit gain and phase lag determined. Roll-off in gain began at ~ 0.5 cps and was down ~ 3 db at 1.5 cps, the spin frequency of the SERT-I vehicle. Above this point the response fell off at ~ 20 db/decade. Phase lag at 1.5 cps was ~ 40°. The E-meter signal from effects that are correlated with vehicle spin, would, then, possess a phase lag of ~ 40° and a reduced gain of ~ 3 db for the first harmonic component of 1.5 cps, with further reductions in gain and greater phase lags for the higher harmonics. Other tests with time-varying fields investigated the response to step functions, linearly increasing and decreasing fields, and to "rectified" sine waves.

Another series of tests examined the meter sensitivity to particle currents. The instrument was placed in a "plasma wind tunnel" as described in Reference 16 and as illustrated in Figure 11. The argon ion plasma stream in this tunnel simulates the plasma density and relative motion for a vehicle moving in the regions of the ionosphere below the protonosphere. The particle current density was varied and the sensitivity of the meter to currents of both ions and electrons was examined.

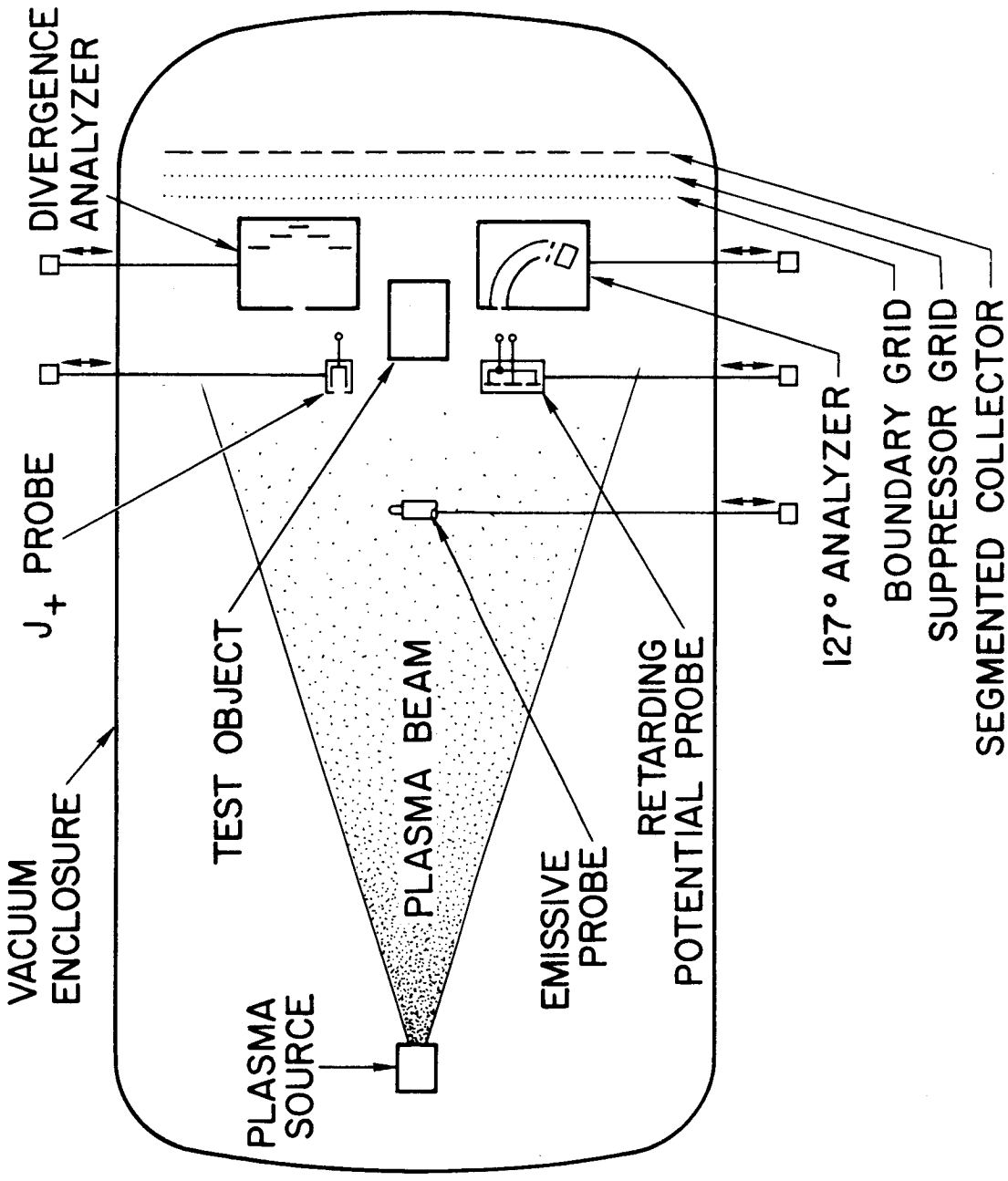

Figure 11. Test configuration in the plasma wind tunnel experiments. The E-meter position is indicated by the test object.

When the overall meter potential was placed negative with respect to the streaming plasma, only ions could be collected by the vanes. For this condition, ion particle current densities of $\sim 3 \times 10^{-9}$ amps/cm^2 were required to produce meter outputs of the general magnitude observed during the second period of the flight described in IV.B.2. For this same plasma density, placing the overall meter potential positive with respect to the plasma produced even larger E-meter signals because of the higher mobility of the plasma electrons. Increasing the ion particle current density to 10^{-8} amps/cm^2 was sufficient to drive the E-meter signal into saturation, for either positive or negative potentials of the meter relative to the plasma stream.

The final series of tests examined the meter sensitivity to ultraviolet radiation. The source of this UV light was a Hinteregger-type source operating, in the ac mode, with hydrogen gas at $\sim$ 10 Torr. The lamp provides a broad molecular hydrogen continuum with its maximum energy in the range from 3000 Å to 1700 Å, with strong illumination in the spectral region between the photoemission threshold for gold and the point of maximum quantum yield. While the lamp does provide a substantial UV output, it is not identical to the solar illuminance which was present at the vehicle surface during the SERT-I flight. This is not of principal concern, however, since the photoemission of surfaces is such an involved phenomenon and is so critically dependent upon surface conditions that the response of the present E-meter may very well not be the same as that of the flight E-meter, even if the two were exposed to identical UV spectra. The general behavior of the E-meter under UV radiation may be tested, though, and this was the intent of the present series of experiments.

The E-meter did exhibit sensitivities to the UV radiation. These effects could be suppressed by placing strong retarding potential fields upon the E-meter. The signals also diminished when strong accelerating fields were placed on the E-meter. While this is not the behavior to be expected for photoelectrons liberated from a simple planar surface, the photoelectric currents from gridded structures, placed before solid backing structures may be, as discussed in IV.B.1., complicated functions of the fields imposed on the surfaces.

A second test of the meter under UV light utilized an Osram HBO 200 mercury source with a spectral cutoff at $\sim$ 2500 Å. The quanta here are of insufficient energy to create photoelectrons, but were capable of inducing short-lived E-meter signals which may be interpreted as contact potential shifts.

IV.B.5. E-METER FLIGHT DATA: DISCUSSION

In the discussion of the E-meter data, the approach will be to consider a definite model of the vehicle in-flight condition, and to examine the consistency of this model against the observed E-meter signals. The model to be discussed is based upon five specific aspects in the observed behavior of these neutralized ion beams. These are:

1. The close coupling of the neutralizer to the plasma in the pulsed beam tests in the small chamber experiments, in which $V_p - V_N$ is only of the order of a few volts.

2. The invariance in the coupling and in the general plasma behavior for increasing lengths of the plasma column as demonstrated in the 25-meter chamber tests.

3. The in-flight demonstration of measured thrust within a few percent of the calculated thrust, assuming perfect neutralization, which provides assurance that unusual behavior, if any, in the

vehicular environment produces only small perturbations.

4. The small measured axial potential decrements along the axis of these thrust beams, being of the order of a few volts for well neutralized beams, with diminishing potentials in moving downstream from the electron injection region.

5. The general behavior that in the region in which the thrust beam plasma density merges into the ambient plasma, the only potential decrements that may be sustained are of the order of a few $\frac{k\ T_e}{e}$ where T_e is the electron temperature.

This model leads to the potentials sketched in Figure 12. The potential in the space plasma is chosen as the zero of the potential and is assumed to be everywhere constant.

For the period before ion beam turn-on, the vehicle has been placed at a small negative potential to reject the bulk of the electrons which diffuse to the sheath region surrounding the vehicle. This corresponds to period 1 in IV.B.2. After ion beam turn-on, this model would place the vehicle at a slight positive potential, if there is no bias of the neutralizer relative to the vehicle skin. This corresponds to periods 2 and 4 of IV.B.2. The remaining period 3 of IV.B.2., in which the vehicle skin was biased several hundred volts negative with respect to the neutralizer, is indicated in Figure 12c.

The first effect to be interpreted in terms of this model is the surface field strength, the quantity nominally measured by an E-field meter. If the E-meter signal were due to a surface electric field, that signal should be virtually absent in period 1, should be present with a small amplitude and with possible spin-frequency variations in periods 2 and 4,

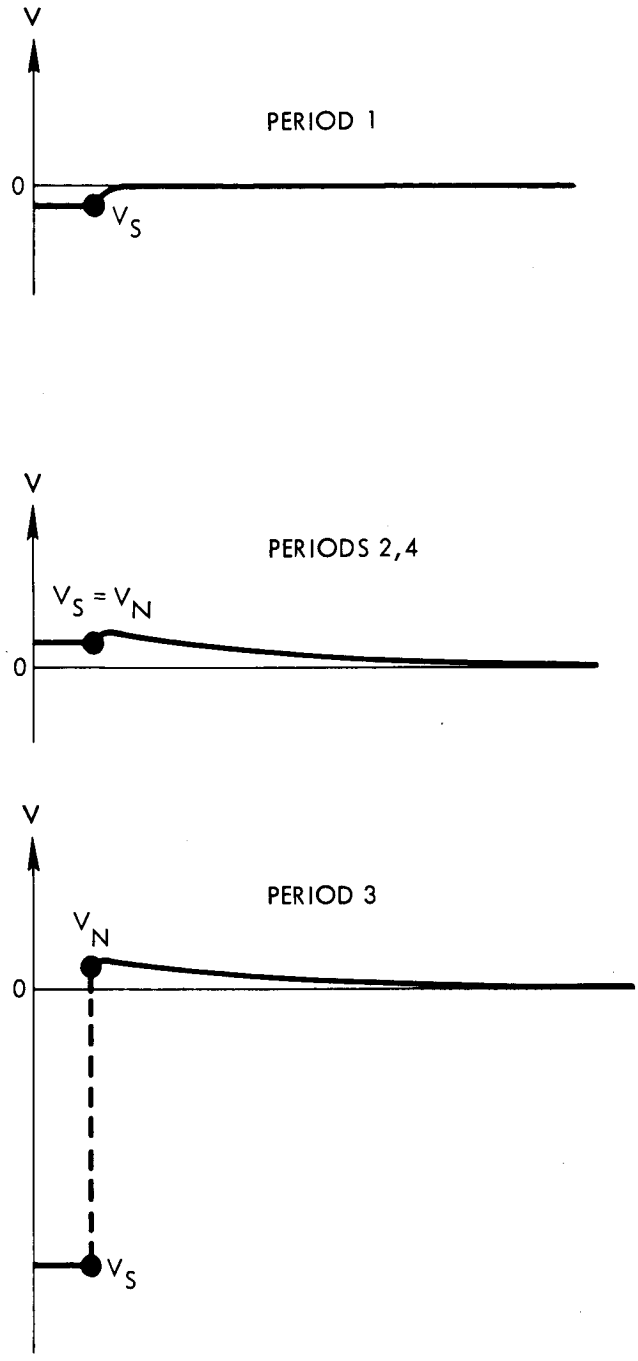

Figure 12. Model of potential configuration during the flight test. The plasma thrust beam is indicated by the curve from the dot outward to the potential of the ambient plasma (V = 0). Vehicle potential, V_S, is indicated by the short horizontal bar.

and should be larger and essentially steady in period 3. The observed data are consistent with these predictions in periods 1 and 3, but the large fluctuating signals observed in periods 2 and 4 are not consistent with the model in Figure 12 if the signals are to be generated by only surface electric fields.

The second effect to be considered in terms of the model is the generation of E-meter signals by particle currents from the ambient plasma. In period 1, these signals should be small, as the "passive" vehicle is receiving equal ion and electron currents at this floating potential. In periods 2 and 4 the collection currents should be (for the most part) electrons, should be spin dependent (in general), and should have a substantial magnitude compared to currents of ions. These electron currents should be larger in period 4 than in period 2 because the vehicle in this later period had returned to denser portions of the ionosphere. In period 3 the only collection currents should be ions, with a magnitude reduced considerably compared to the electron currents, and should be reasonably independent of the vehicle spin. The predictions of the model are consistent with the observed E-meter signals. Further, by a combination of particle collection currents and surface electric field effects, the E-meter behavior predicted by the model is consistent with the observed E-meter signals in all periods.

The final effect to interpret in terms of the model is photoelectric currents due to the solar ultraviolet. If photocurrents were present and were contributors to the E-meter signals, these contributions should be present in periods 1 and 3 as a spin-dependent signal and absent in periods 2 and 4. The observed signals differ from this predicted behavior in several respects. This lack of agreement can be interpreted either as an inconsistency between the specific model and the

possible solar photoeffects, or as a portion of a more general body of evidence from the flight data against the influence of photocurrents. The several aspects of this larger body of evidence against photoemission effects are:

1. The absence of an E-meter signal in period 1.
2. The absence of a spin dependent signal in period 3.
3. The growth of the signal in period 4 from its level in period 2.
4. The phase of the E-meter signal relative to the solar detector.

Apart from the specific model in Figure 12, it is difficult to postulate a positive vehicle potential for periods 1 and 3. This is particularly true of period 3. For negative vehicle potentials photoelectrons are accelerated away from the surface, and a photoelectric effect, if present, should be observable. Further, a photoeffect, if present, should not be of increasing magnitude, so that photosignals in period 4 should not differ from those in period 2. Finally, the phase of the E-meter signal might be expected to have the peak of the signal when the meter is facing the sun. However, the observed phase (Figure 10) shows that the peak of the signal occurs when the E-meter is facing almost directly away from the sun and the minimum occurs when the meter is facing the sun (the discussion here takes into consideration the phase lags of $\sim 40°$ at the 1.5 cps frequency of the vehicle spin). A photoeffect with these phase relationships can only be explained as being in addition to, but opposing, a larger signal.

While the several aspects listed are evidence against photoelectric effects, it should be emphasized that this discussion was based upon photoemission from a planar surface. For gridded surfaces in the near neighborhood of solid surfaces,

the possible exchange of photocurrents becomes so involved that no firm conclusions may be made regarding these signals. The laboratory tests, for example, displayed photosignals only for relatively weak electric fields upon the E-meter surfaces. It is possible, thus, that photoeffects do contribute to the overall E-meter signal in periods 2 and 4.

In summary, the model of Figure 12 is consistent with the observed E-meter signals assuming these signals to result primarily from particle collection currents in periods 2 and 4 (with some possible photoeffects in these same periods), and primarily from surface electric fields in periods 1 and 3. The response of the meter in the laboratory tests and the magnitude of the particle currents to be expected at the altitudes of the flight test are, in turn, consistent with the observed signals.

V. ADDITIONAL DIAGNOSTIC TECHNIQUES

V.A. Surface Field Measurements

In IV.B.1., some of the limitations in surface field measurements for ion engine diagnosis have been detailed. The primary limitation is that the vehicle potential and the surface electric field strength are not simply related if the vehicle is within the dilute plasmas in the near neighborhood of the earth, while additional complications result if the vehicle speed exceeds the thermal velocities of the ions in this ambient plasma. At greater altitudes, the plasma densities diminish, ion thermal velocities increase (because of the lighter ion masses at these altitudes), vehicle potential becomes more nearly equal to $E_s\ r_s$ (for a spherical vehicle) and the use of the vehicle surface field becomes, in general, less subject to environmental perturbations. The operation of the

rotating-vane E-field meter, as a specific technique for determining the surface field strength, is also less subject in these higher altitude regions to the environmental effects of plasma particle currents. Solar photoeffects and possible contact potential shifts would remain as possible perturbations to the rotating-vane meter.

A second technique for surface field measurements is the "button" type E-meters (Reference 17). These devices function by means of small emitted and collected currents ($\sim 10^{-3}$ amperes or less), but the emitting areas are also small (~ 0.1 cm^2) so that the current density contributing to the meter signal is large compared to any background currents due to photoemission or particle currents from the ambient plasma. As such, the button E-meters are less subject to environmental perturbations.

The surface field measurement does not, however, provide a direct determination of the potential in the plasma thrust beam. Indeed, though the relationship between surface field and vehicle potential is a simple one for the distant regions of space, the further relaxation of the vehicle surface field to the thrust beam potential may be quite difficult to make for a vehicle in the almost perfect isolation of these very dilute plasmas. Even further, the nature of those remaining environmental factors is uncertain, being complicated by the behavior of the solar winds and their interactions with the magnetic fields and ambient plasmas in the region in question. For these several reasons, other diagnostic techniques, which provide a direct determination of thrust beam potential, should be considered.

V.B. EMISSIVE PROBE MEASUREMENTS

The plasma potential data given in Figure 2 were obtained with conventional emissive probe technique with an accuracy of $\sim$ 0.5 volts in this application. If the probes are operated in the floating condition, the accuracy of measurement is $\sim$ 1-2 volts. A probe suitable for vehicular use and utilizing a driven shield cathode follower circuit for greater frequency response is described in Reference 18. This emissive probe does provide a direct measurement of the potential in the plasma and possesses a bandwidth capable of detecting potential fluctuations, if these are present in the vehicular operation of an ion engine, of up to the hundred kilocycle range. Because the probe requires immersion in the plasma beam for best operation, its operating lifetime is limited unless provisions are made for its withdrawal and protection except during sampling periods.

One further use of emissive probes is the determination of the potential of vehicles that are still within regions near the earth. In this configuration the probe is immersed in the ambient plasma, and measures the potential of the plasma relative to the vehicle. Special considerations which apply to the probe operation in these dilute plasmas are discussed in Reference 5.

VI. SUMMARY

The effective neutralization of ion thrust beams has been demonstrated in both controlled laboratory experiments and in the NASA SERT-I space test of a mercury electron bombardment ion thrustor. In the laboratory experiments the exhaust beam potential was 5 to 10 volts positive with respect to the neutralizer depending upon the specific neutralizer configuration.

The accuracy of this emissive probe measurement is ~ 0.5 volt. In the SERT-I space flight test the measured thrust agrees with the calculated thrust, assuming perfect neutralization, within 5%. This demonstrates that the ions attain the acceleration energy they would achieve under perfect neutralization to within, at most, second order effects. The absence of unusual behavior in the SERT-I space flight test as compared to the laboratory test when properly conducted, is assurance that controlled laboratory tests of neutralization systems do provide an adequate examination of the neutralization process.

The diagnostic techniques by which the ion beam thrust was determined were not subject to any particular perturbations of the vehicular environment. The evidence from the flight data and from the subsequent laboratory tests of the rotating-vane electric field strength meter, however, has shown that environmental effects were contributing factors to the signals from this instrument. A second diagnostic technique for surface field strength measurements, the E-meter button, should possess a reduced sensitivity to environmental factors because of the higher current density condition in the operation of the meter.

The interpretation of vehicle potential from the surface field strength measurement requires significant corrections because of the ambient plasma in the near neighborhood of the earth. For regions more distant from the earth these perturbations should diminish. In both regions, however, surface field strength measurements do not provide a direct determination of the potential in the thrust beam plasma and supplementary diagnostic techniques should be considered. Emissive probes possess a capability of measuring this exhaust

beam potential within a fraction of a volt, and of following any fluctuations in this potential for frequencies of up to $\sim$ 100 kilocycles. The probes would require withdrawal from the plasma column except for the measurement periods.

ACKNOWLEDGEMENTS

The authors wish to acknowledge the interest and helpful discussions of J. H. Childs and J. T. Kotnik of Lewis Research Center, NASA and R. F. Kemp and R. K. Cole of TRW Space Technology Laboratories.

REFERENCES

1. Kemp, R. F., Sellen, J. M., Jr., and Pawlik, E. V., "Beam neutralization tests of a flight model electron bombardment engine," AIAA Preprint 2663-62 (November 1962).

2. Kemp, R. F., Sellen, J. M., Jr., and Pawlik, E. V., "Neutralizer tests on a flight-model electron bombardment ion thrustor," NASA TN D-1733 (July 1963).

3. Sellen, J. M., Jr. and Kemp, R. F., "Cesium ion beam neutralization in vehicular simulation," ARS Preprint 61-84-1778 (June 1961).

4. Ward, J. W. and Hubach, R. A., "Neutralization of ion beams from engines of annular geometry," ARS J 32, 1730 (November 1962).

5. Sellen, J. M., Jr. and Kemp, R. F., "Emissive probe characteristics in dilute plasmas," APS 6th Annual Meeting of the Division of Plasma Physics (November 1964).

6. Sellen, J. M., Jr. and Kemp, R. F., and Hieber, R. H., "Observations of neutralized ion thrust beams in the 25-meter NASA testing chamber," Section III.G of NASA Final Report Contract NAS8-1560 (April 1964).

7. Hanson, W. B., "Structure of the ionosphere," Satellite Environment Handbook, edited by F. S. Johnson (Stanford University Press, Stanford, California, 1961), Chap. 2.

8. Gold, H., Rulis, R. J., Maruna, F. A., Jr. and Hawersaat, W. H., "Description and operation of spacecraft in SERT I ion thrustor flight test," NASA TM X-52050, (1964).

9. Cybulski, R., Shellhammer, D., Lovell, R., Domino, E., and Kotnik, T., "Results from the SERT I ion rocket flight test," NASA TN (1965).

10. Baldwin, L. V. and Sandborn, V. A., "Theory and application of hot-wire calorimeter for measurement of ion beam power," Electrostatic Propulsion, edited by D. B. Langmuir, E. Stuhlinger, and J. M. Sellen, Jr., (Academic Press, New York, N. Y., 1961), pp. 425-446.

11. Waddel, R. C., "An electric field meter for use on airplanes," Rev. Sci. Instr. 19, 31, (January 1948).

12. Hall, D. F., Kemp, R. F., and Sellen, J. M., Jr., "Plasma-vehicle interaction in a plasma stream," AIAA J. 2, 1032 (June 1964).

13. Kotnik, J. T. and Hawersaat, W. H. (private communication).

14. Sellen, J. M., Jr., and Bernstein, W., "Interactions of collisionless plasma streams with transverse magnetic fields," Phys. Fluids 7, 977 (1964).

15. Kemp, R. F., Cole, R. K., Hall, D. F., and Sellen, J. M., Jr., "Sensitivity tests on a flight-model rotating-vane E-meter," TRW Space Technology Laboratories report No. 4137-6017-KU-000 (January 1964).

16. Hall, D. F., Kemp, R. F., and Sellen, J. M., Jr., "Generation and characteristics of plasma wind tunnel streams," TRW Space Technology Laboratories, report No. 4137-6012-KU-000, (Submitted to AIAA J.).

17. Forbes, S. G., Kemp, R. F., Sellen, J. M., Jr., Shelton, H., and Slattery, J. C., "Ion engine testing techniques," ARS Preprint 2183-61 (October 1961).

18. Crosby, J. K. and Fulton, A. S., "Design, development, and fabrication of a floating emissive probe for ion beam diagnostics," TRW Space Technology Laboratories, final report Contract NAS3-2517 (June 1963).

SECTION II.D.

SENSITIVITY TESTS ON A FLIGHT-MODEL ROTATING-VANE E-METER

4137-6017-KU-000

"SENSITIVITY TESTS ON A FLIGHT-MODEL ROTATING-VANE E-METER"

by

R. F. Kemp, D. F. Hall and J. M. Sellen, Jr.
TRW Space Technology Laboratories, Inc.
Redondo Beach, California

and

R. K. Cole
University of Southern California
Los Angeles, California

4 January 1965

PHYSICAL ELECTRONICS LABORATORY
Physical Research Division

TRW Space Technology Laboratories
Thompson Ramo Wooldridge Inc.
One Space Park, Redondo Beach, California

SENSITIVITY TESTS ON A FLIGHT-MODEL ROTATING-VANE E-METER

I. INTRODUCTION

Several series of tests have been performed on a rotating-vane electric field meter of the type flown in the SERT I vehicle.* The purpose of the tests was to determine experimentally the sensitivity of the instrument to various aspects of the space environment which were encountered in the flight. The tests involved subjecting the instrument to electric field signals--both static and time-varying, illumination by ultraviolet light (to simulate this effect in solar radiation), and exposure to a low-density streaming plasma in a "plasma wind tunnel."

II. DESCRIPTION OF E-METER

The transducer element of the electric field meter is depicted in the sketch and schematic drawing, Figure 1. It consists of two metallic vanes, one rotating and one stationary, within a recess in the vehicle surface. Both vanes and the interior surface of the recess are gold plated. The material of the vanes is cut away, except for six spokes and the grid mesh (as shown) which forms three "blades." In its principles of operation, the instrument is similar to that described in Ref. 1, and used for studies of "precipitation static" on airplanes.

The E-meter has two output amplifiers, one each for high- and low-sensitivity, 4-volt (nominal) full scale telemetering channels. The amplifiers have a common input connection, and are identical, except for the size of the gain-controlling

*E-meter constructed by Hughes Aircraft Co. The electric field strength meter was located in the control package for the Hughes contact ionization thrustor on the SERT I spacecraft.

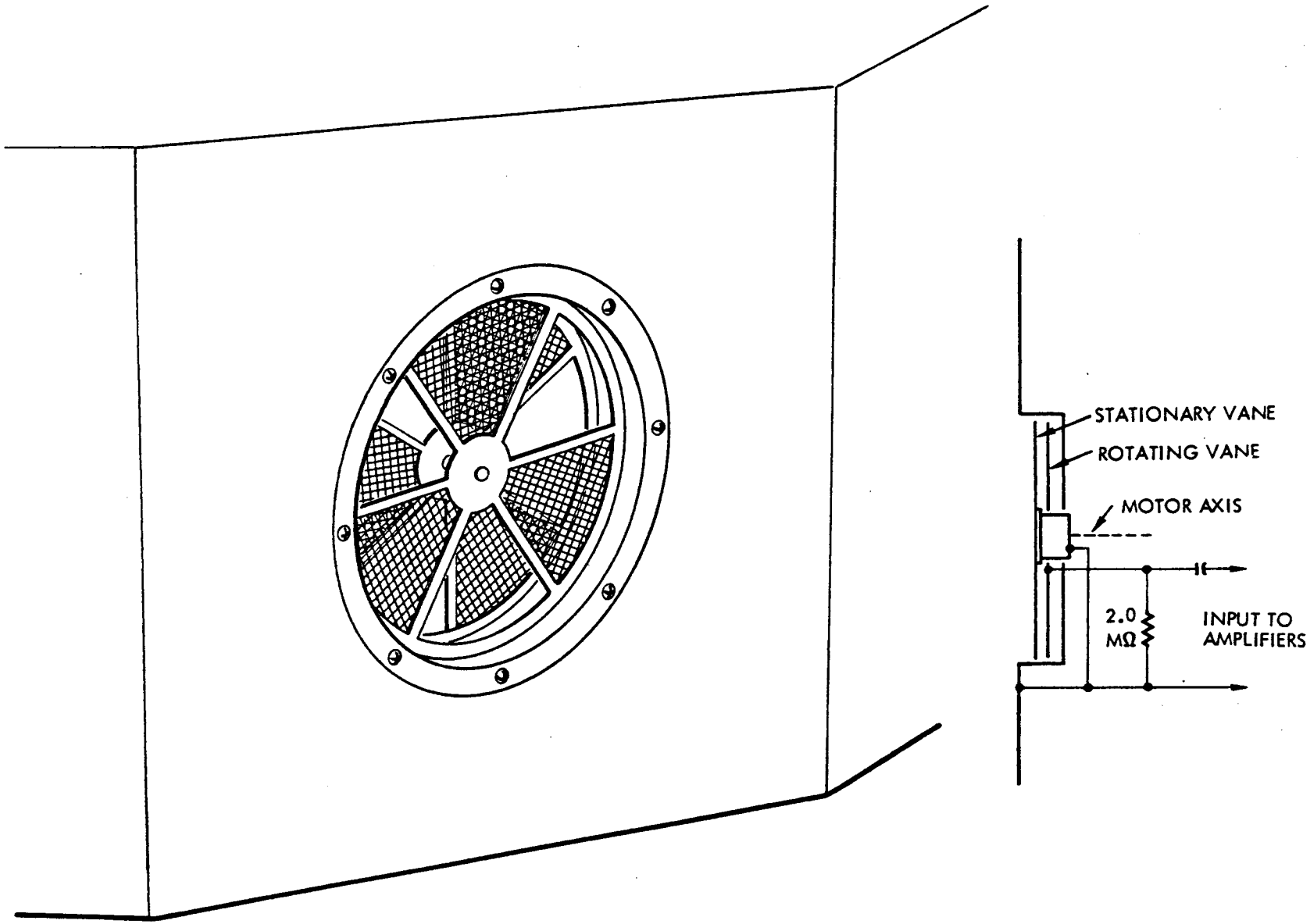

Figure 1. The SERT I electric field meter transducer. The sketch at left depicts the gridded structure of the vanes.

resistor, and inclusion in the high-gain channel of a diode limiter. Both outputs were examined in some, but not all, of the tests described below.

III. ELECTRIC FIELD ONLY

A. Zero-Frequency Calibration

To measure the sensitivity of the instrument to external electric fields, a copper plate, sufficiently large to effectively eliminate edge effects, was placed parallel to and about 3.3 cm from the stationary vane. The output voltages of both amplifiers were measured as functions of positive dc voltages applied to the plate. These results are shown in Figure 2. The values of field strength shown are 30 times the applied plate voltages. Approximate maximum values of output signals are 4.5V for a field strength of 3000 V/m and 5.8V for 9000 V/m for the high-sensitivity and low-sensitivity channels, respectively. The middle of the most linear portion of each curve occurs at $\sim$ 1000 V/m or $\sim$ 3000 V/m. The high-sensitivity channel has a zero offset of $\sim$ 0.2V at zero field. In later tests this value ranged up to over 2 volts. This is possibly a contact-potential effect, or it could be due to internal noise pick-up, or to a combination of these effects. In the figure, the low-sensitivity channel shows a small E-field threshold below which the output is zero. Later, this channel also developed a positive offset.

B. Time-Dependent Signals

Time-varying signals with a variety of waveforms were applied to the plate in front of the E-meter, and, except for the small-signal frequency response, the response waveforms of

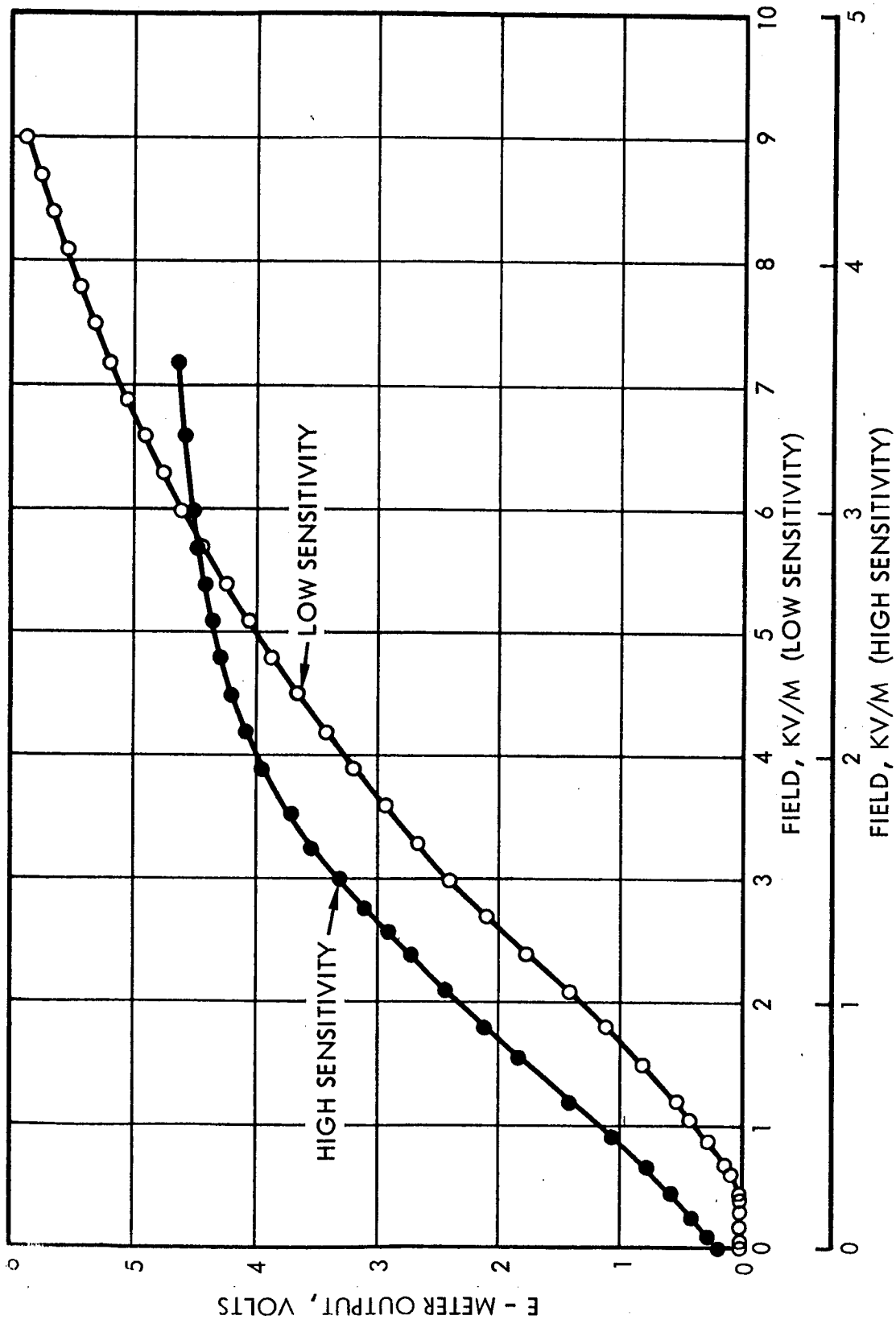

Figure 2. Zero-frequency calibration curves for the SERT I E-meter.

the instrument were recorded photographically from oscilloscope traces. In order to measure the frequency response of the instrument, a dc potential was applied to the plate such that the output (low-sensitivity channel) was biased to 0.8V. Then to this plate potential was added a small ac signal which gave rise to sinusoidal oscillations of the output having, at the lowest frequency, a peak-to-peak amplitude of about 300 mV. The input amplitude was maintained constant, and the ac output amplitude measured as the frequency was varied from 0.05 to 15.0 cps. Results of this test are shown in the db versus log frequency plot, Figure 3. The straight line drawn on the curve is that line at a slope of -20db/decade (typical of a single-time-constant circuit) that best fits the data points. This line intersects the zero-db line at a frequency of about 1.5 cps. Consequently, the E-meter output can be expected to exhibit $\sim 45°$ phase lag at the spin frequency of the SERT I vehicle.

C. Large-Signal Response Tests

Results of the large-signal response tests are shown in Figures 4 and 5. For these tests, the copper plate was moved much closer to the E-meter so that large electric fields could be imposed on the instrument by voltages within the range of laboratory signal generators.

1. Triangular Waveforms

The series of photographs shown in Figure 4 depicts the response of the instrument to triangular waveforms (magnitude of dV/dt = constant) of varying frequency. In all these photographs, the oscilloscope horizontal amplifier was connected to the voltage on the plate. The zero-volts position of the sweep is at the center of the screen, and the horizontal

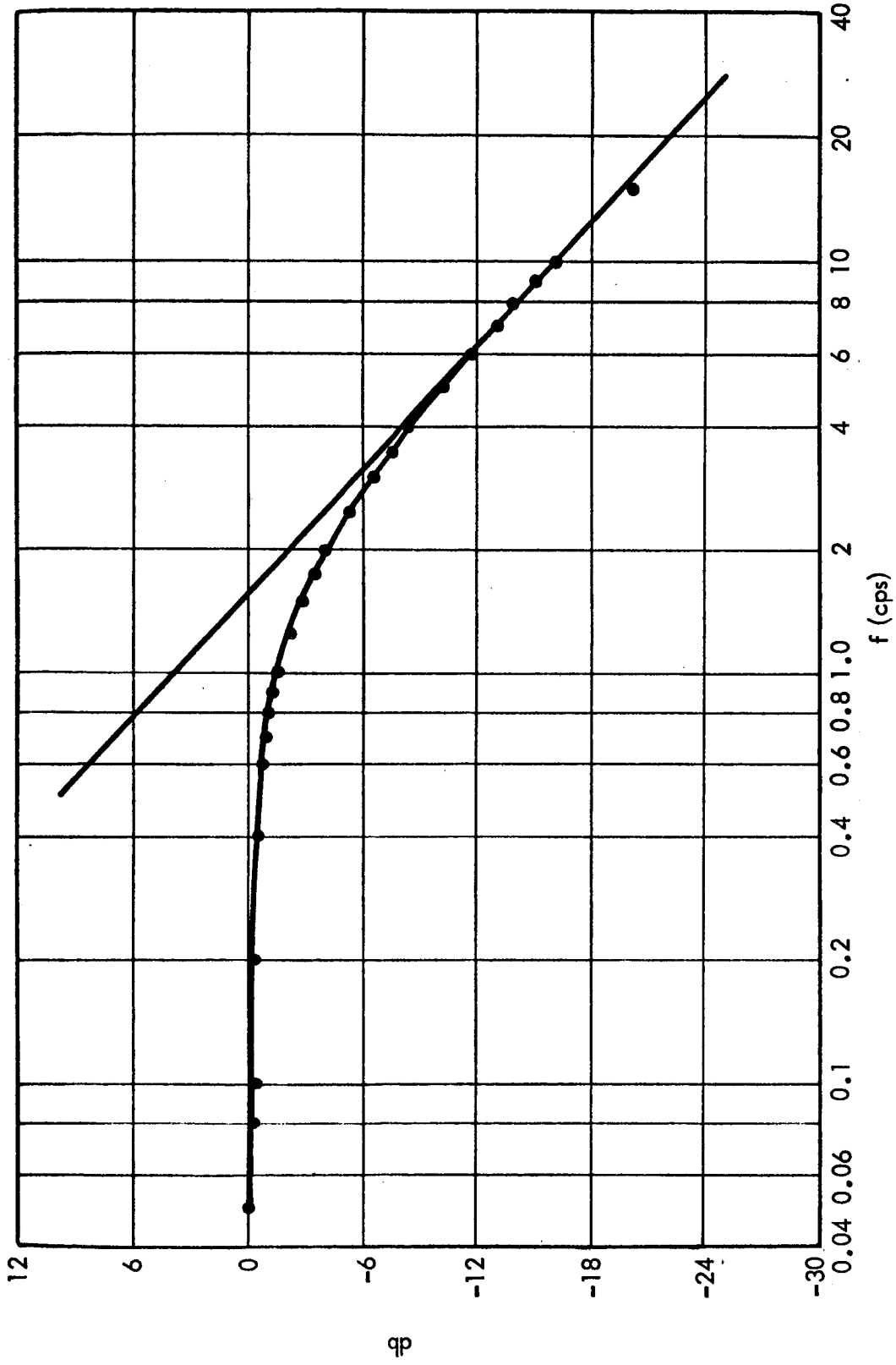

Figure 3. Small-signal frequency response curve of the E-meter amplifier.

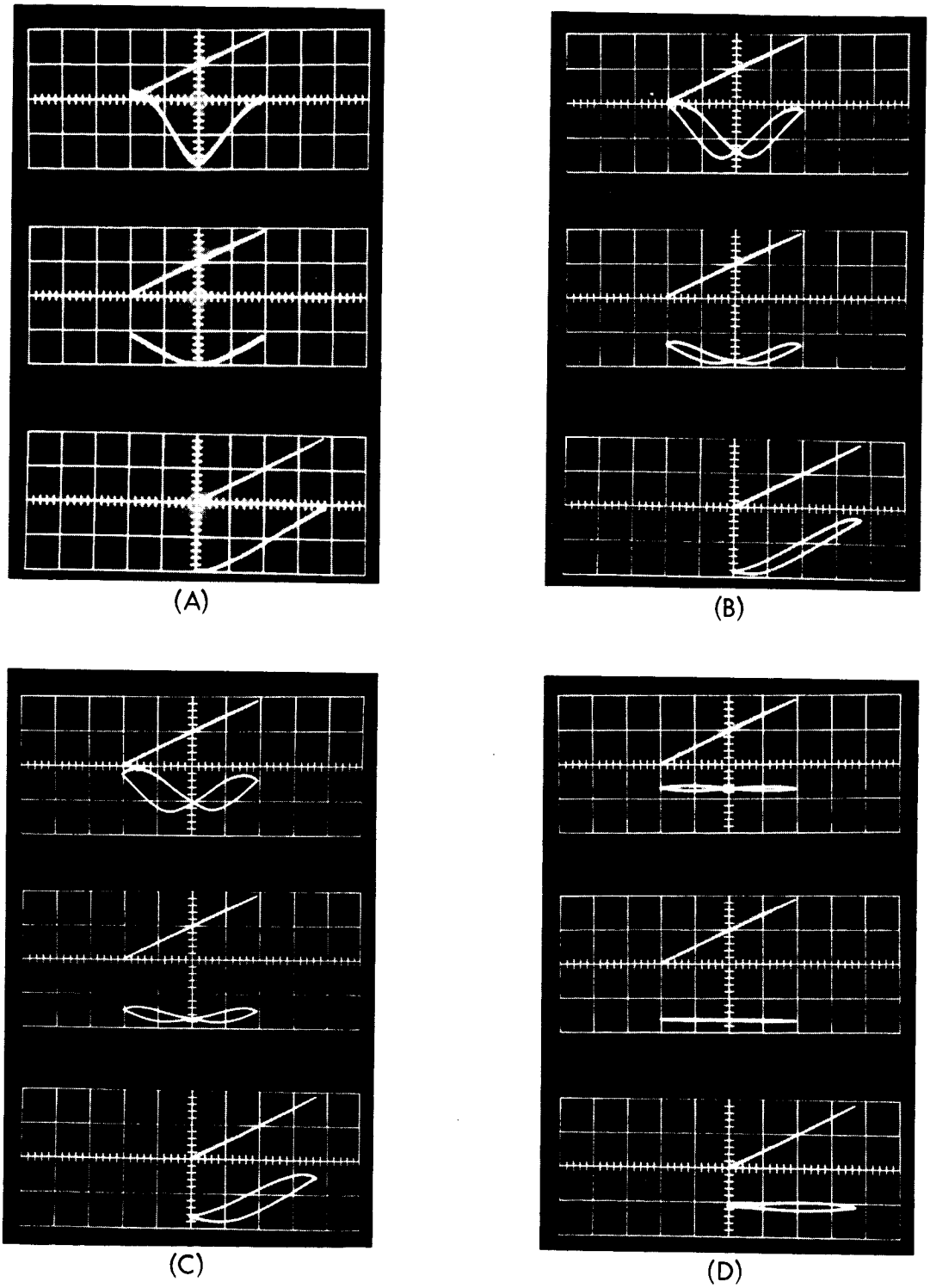

Figure 4. Response of the E-meter to electric field signals of triangular waveform and various frequencies. Horizontal: plate voltage (10V/div., zero at center). Vertical: upper trace in all photos is plate voltage (20V/div., zero at horizontal center of frame); lower trace, top frame--E-meter output high sensitivity (2V/div., zero at bottom), middle and bottom frames--E-meter output low sensitivity (2V/div., zero at bottom). Frequency of triangle waveform: (a) 0.05 cps, (b) 0.5 cps, (c) 1.0 cps, (d) 10.0 cps.

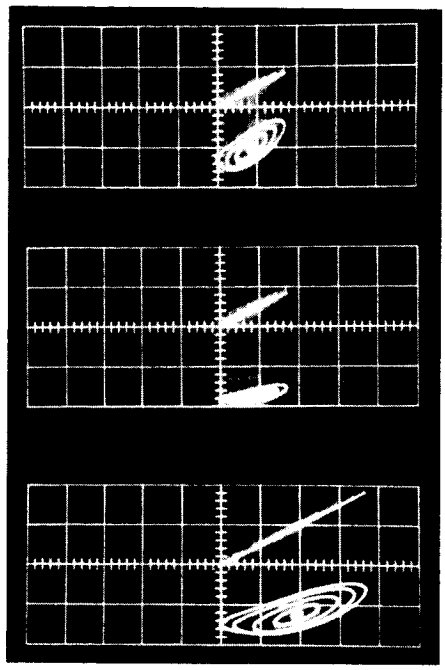

(A)

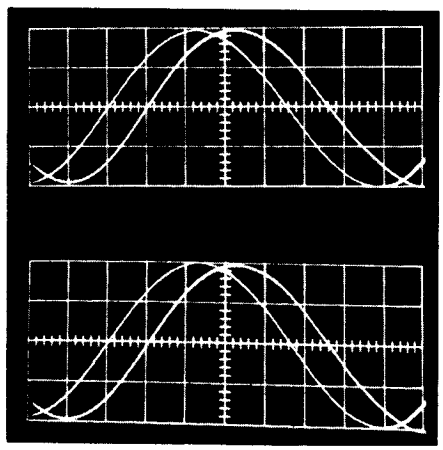

(B)

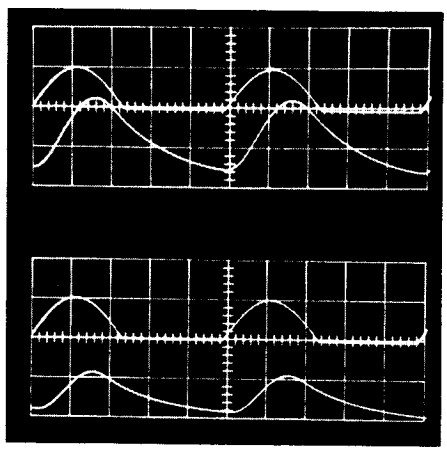

(C)

Figure 5. Response of the E-meter to electric field signals of various waveforms at 1.5 cps., approximately the spacecraft spin frequency. Calibrations in (a) are the same as for Fig. 4. Photo (b) is a measure of phase lag in high- (upper) and low-sensitivity (lower) channels. Photo (c) is response to half-wave rectified signal (see text).

amplifier sensitivity is 10 volts per large division of the reticle. For each of four frequencies, a set of three photographs is shown, each containing two traces. In the uppermost picture, the upper trace is plate voltage at 20V/div., (zero, one division from the top), and the lower trace is the output of the high-sensitivity channel of the E-meter at 2.0V/div. (zero at bottom). In the middle frame, upper trace is plate voltage and lower trace is low-sensitivity channel output at 2.0V/div., (zero at bottom). In the bottom frame, the inputs are the same as for the middle frame. Thus, in Figure 4a, one sees that the plate voltage is sweeping linearly between about -20 volts and +20 volts in the upper and middle frames, and from 0 to about +38 volts in the bottom frame. The lower traces show that at a frequency of 0.05 cps, the instrument is tracing out most of the calibration curves of Figure 2, giving a positive output for E-fields of either positive or negative sign. At higher frequencies, (b, c, d) the output traces are loops because of the effect of phase lag in the instrument. Finally, at 10 cps, the output signals are smoothed out to values corresponding to the average value of the magnitude of the applied electric field.

2. Signals at the SERT I Vehicle Spin Frequency

The three photographs shown in Figure 5 were all taken at the frequency of 1.5 cps, which corresponds closely to the spin frequency of the SERT I vehicle. In Figure 5a, the calibrations are the same as in Figure 4. Again, top frame is high-sensitivity channel, middle and bottom, low-sensitivity channel. What is shown is the response of the instrument to sinusoidal oscillations of various amplitudes about dc values of electric field. Departure of the response signals from

straight lines (formation of loops) is the result of phase shift in the response; departure of the shape of the loops from ellipses at the higher amplitudes is the result of non-linear distortion. Figure 5b is a phase-shift measurement of both the high- and low-sensitivity channels at 1.5 cps. The figure is a display versus time of a small-amplitude sinusoidal voltage which was added to a dc bias on the plate, and the response signal of the E-meter. It is essentially, a display versus time of the small ellipses shown in Figure 5a. Vertical scales for both signals were adjusted to give the same deflection, and the horizontal sweep was adjusted to display one complete cycle in 9 divisions, (or 40 degrees per division). This measurement shows the phase shift at 1.5 cps to be almost exactly 40 degrees.

One of the possible input signals to the E-meter on the SERT I flight was a photoelectric signal due to solar illumination. The waveform of the intensity of this illumination would most likely be one-half of a 1.5-cps sine wave as shown in the upper traces in the two frames of Figure 5c. That is, the solar illumination would be zero when the E-meter was on the dark side of the vehicle, and would be proportional to the cosine of the angle between the solar direction and the surface normal when the E-meter was on the illuminated side. The response of the two channels of the instrument to this waveform of electric field signal is shown in the lower traces of Figure 5c. The decay time-constant of the amplifiers is sufficiently long to prevent the output from returning to zero during the off-time of the input signal.

3. Amplifier Time Constant

The output of each amplifier is simply the voltage across a filter capacitor. This capacitor is charged

through the output impedance of the final stage of the amplifier circuit, and discharged through a shunt resistor. Consequently, the charging and discharging time constants may be expected to differ from each other. A careful measurement of these time constants using very low frequency square waves showed that the e-folding time constant for an increasing step function is ~ 90 milliseconds, and that for a decreasing step ~ 200 msec, in both amplifiers.

IV. ULTRA-VIOLET ILLUMINATION

The waveform of possible solar uv illumination encountered by the electric field meter in the course of the SERT I space flight was discussed in Section III.C.2, above, and, in one of the tests, an electric field signal of that waveform was used. The tests described in this section measured the response of the instrument to light signals from two different uv sources, in the presence of dc applied electric fields.

The E-meter was first illuminated with light from a high pressure mercury arc lamp.* Initially the light produced a photoelectric signal and altered the response of the E-meter to an applied electric field. The magnitude of the E-meter response to the mercury lamp illumination decreased with time and became unmeasurable after some tens of minutes. Thereafter the E-meter showed no response to the mercury lamp light. The initial response is believed to be due to the presence of surface contamination. Once this surface contamination disappeared under intense illumination in a vacuum, the cleaner surface could not emit photoelectrons since the work function became higher than the energy equivalent, in volts, of the impinging

*Osram Lamp No. HBO-200W

photons. The work function of a clean gold surface is about 4.9V, and the lamp enclosed in a quartz bulb has its intensity cut-off at 2500Å or 4.96 eV.

Photoelectric signals were observed, however, when the E-meter was illuminated with light from a hydrogen discharge. The lamp used was a Hinterreger-type light source, operating in the ac mode with hydrogen gas at 8 to 10 mm Hg pressure. A large portion of the radiation from this source is due to the dissociative molecular hydrogen continuum ($1s\sigma\ 2s\sigma\ ^3\Sigma_g^+ \rightarrow 1s\sigma\ 2p\sigma\ ^3\Sigma_u^+$). The other major contribution is from the "many-lines" spectrum of molecular hydrogen. The continuum has its maximum intensity in the 3000Å to 1700Å, with a broad peak at around 2500Å. This lamp may be expected to be a source of relatively strong illumination in the spectral region between the photoelectric threshold for gold and the point of maximum quantum yield. It should be pointed out that the light from this lamp is not equivalent in either frequency distribution nor intensity to the solar irradiation at the SERT I vehicle surface. In order to shield the E-meter from electric fields and streams of charged particles emanating from the lamp, the light was made to pass into the vacuum chamber containing the E-meter through a calcium fluoride window. This single crystal, 7.6 mm thick, is transparent to ultraviolet light down to about 1200 Å.

Figure 6 shows the shift in E-meter readings on the low-sensitivity channel which was due to illumination by the hydrogen-discharge lamp. The effect is small (never greater than 5% of full-scale), and diminishes to negligibly small values in the presence of applied electric fields of either polarity. A discussion of photoelectric effects as they relate to the E-meter on the SERT I space flight is given in Section VI, below.

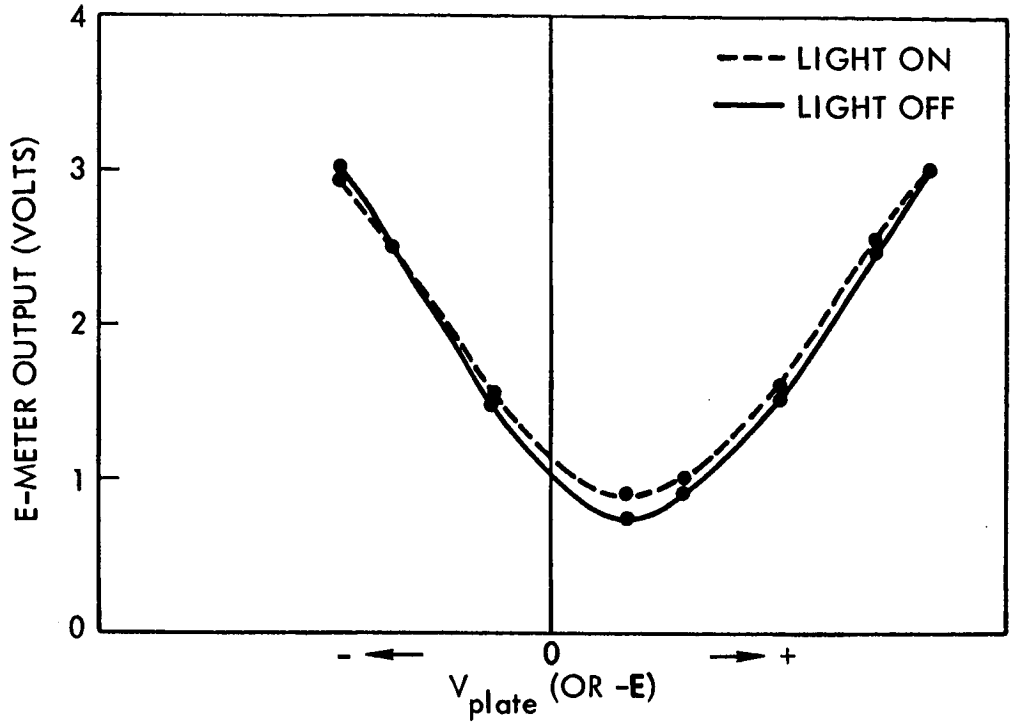

Figure 6. Photoelectric variation in E-meter response observed under uv illumination

Included in the curves of Figure 6 is another effect not related to photoelectric effect. At about this point in the experimental program, the internal connection opened up between the transducer element case and the common ("ground") point on the amplifier input. It was possible to restore the instrument to operating condition by making this connection externally (the instrument is potted in styrofoam), but in such cases, the likelihood of introducing extraneous noise signals is increased. From this point on, both output channels have shown positive dc offset voltages, and the minimum values of the output signal occur at positive or negative values of applied field, depending on the phase angle at which the synchronous motor locks onto its power supply voltage. (At least four distinct locking modes have been observed.)

V. PLASMA WIND TUNNEL TESTS

Figure 7 shows the plasma wind tunnel experimental arrangement which was used during tests in which the E-meter was subjected to currents of charged particles from a plasma stream. The plasma source was an electron bombardment ion thrustor of the same type as that flown on the SERT I experiment, operating on argon gas instead of mercury. A moveable plate was installed in front of the E-meter in approximately the same position as the copper plate used in the electrical tests (Section III, above). In this case, however, the plate could be moved aside, exposing the E-meter to the plasma stream, or a second plate containing a gridded aperture of the same diameter as that of the E-meter transducer could be positioned in place of the solid plate. The E-meter was electrically isolated from its mounting inside the vacuum chamber so that its potential relative to the plasma stream could be varied.

When the plate is in position, the instrument responds only to electric fields imposed by the plate; when the grid is in place, it can be biased so that only ion currents impinge on the E-meter transducer. When both plate and grid are removed, the E-meter is exposed to both ion and electron currents, and its response is strongly dependent on the potential between the E-meter and the plasma. These effects are seen in Figures 8 and 9. In Figure 8, the trace is E-meter output (high-sensitivity channel) at a vertical oscilloscope calibration of 2 volts/division, zero at bottom. Horizontal sweep is at the rate of one division/second. The E-meter, the plate, and the grid are all at ground potential; the potential of the plasma is about +10 volts. At about the middle of each frame a change in conditions was made--the photos qualitatively

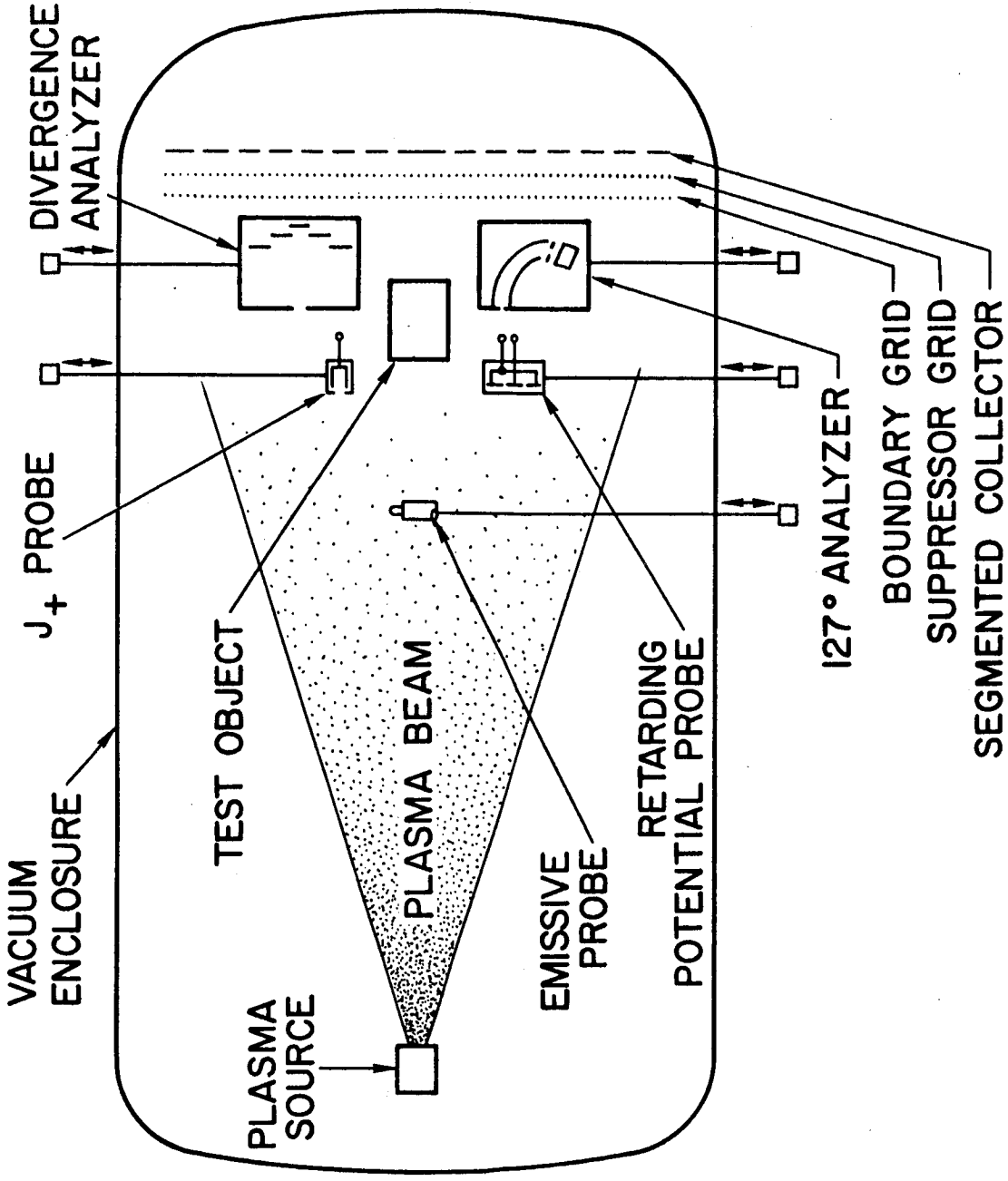

Figure 7. Test configuration in the plasma wind tunnel experiments. The E-meter position is indicated by the test object.

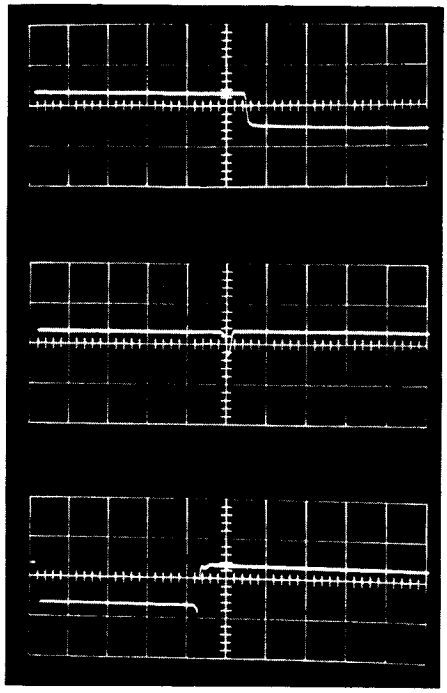

(A)

Plate removed: Beam on/off.

Beam on: Open/grid.

Beam on: Plate/open.

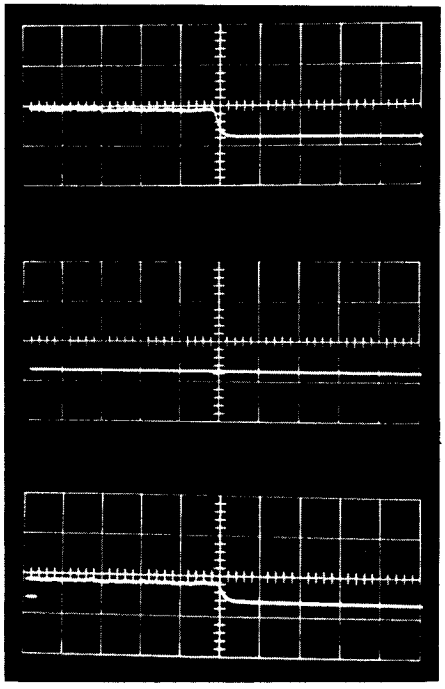

(B)

Grid (-8V): Beam on/off.

Plate (-8V): Beam on/off.

Open: Beam on/off.

Figure 8. E-meter response in first plasma wind tunnel test. In all frames, vertical: E-meter high-sensitivity output (2V/div., zero at bottom) (Note: dc offset is about 2.4V.); horizontal sweep, 10 seconds full frame. Notes beside each frame indicate nature of change made as trace passed center of frame.

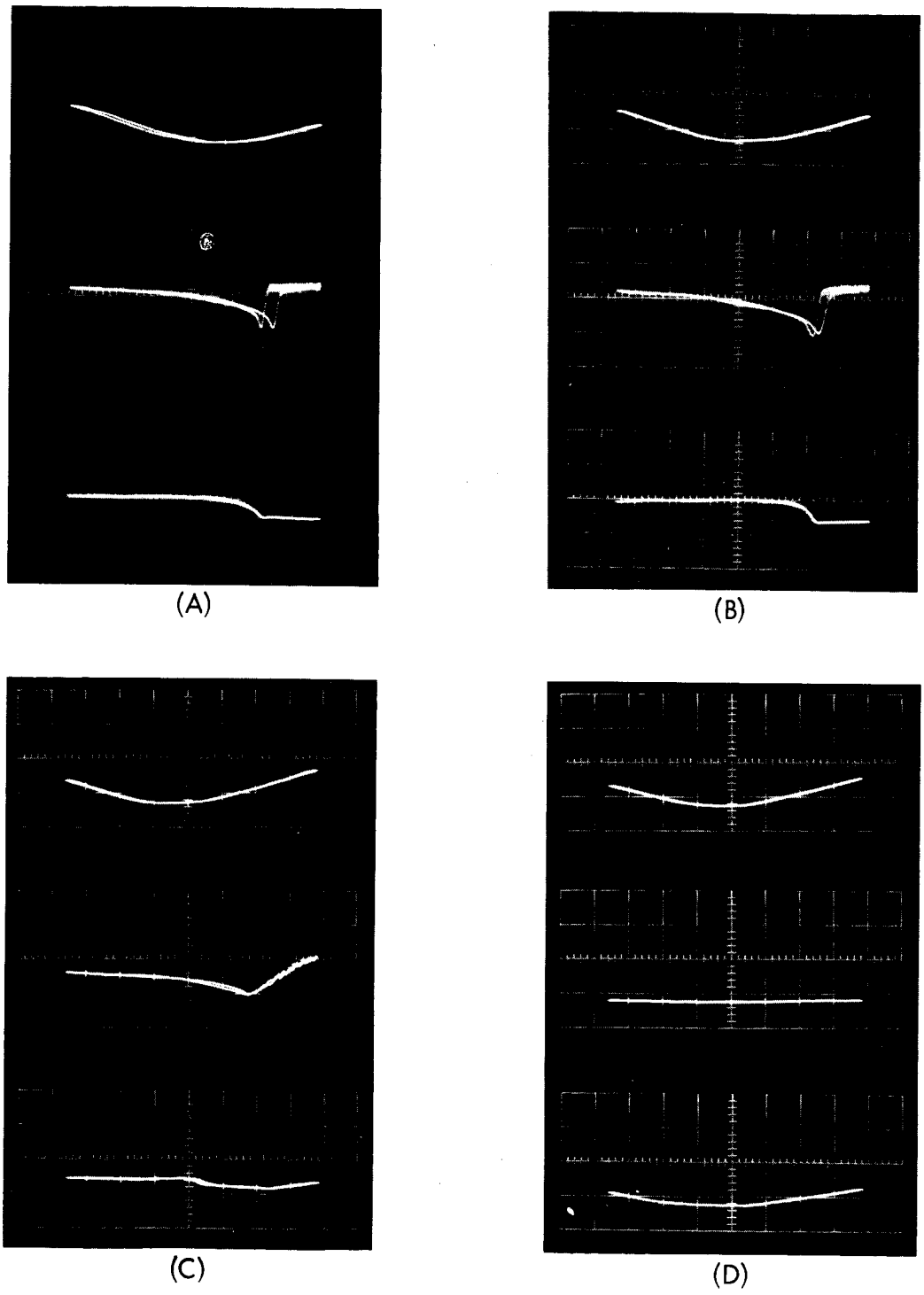

Figure 9. E-meter response in second plasma wind tunnel test. Horizontal: E-meter potential (5.0V/div., zero at center). Vertical: E-meter output, high-sensitivity (2V/div., zero at bottom). In each top frame, plate is in position; for middle frame, E-meter is exposed to plasma stream; in bottom frame, grid is in place. Plate and grid are at V = 0; plasma potential is +10V. Ion current densities at E-meter location are (a) 6.6, (b) 5.0, (c) 3.3, all times 10^{-9}A/cm^2. In (d) beam is off.

indicate the effect as follows: In a, top frame, the plate has been turned aside; as the sweep moves past the middle of the screen, the beam is turned off. The output signal goes from saturation (over 4 volts) due to ion current to the current value of the dc offset. In the middle frame, again, at the start, the plate has been turned aside. At the middle, the grid is put in place. The E-meter sees the same ion current signal through the grid as it does in the open condition. In the bottom frame, the plate is in front of the E-meter at the start; it is turned aside at the middle of the sweep. The effect is essentially the reverse of the top frame. For the b group of frames, the plasma density was reduced so that the ion signal would not quite saturate the output amplifier (ion current density at the E-meter location was about 5×10^{-4} A/cm^2). In all three frames, the beam is turned off at the center of the sweep. Top frame--grid at -8 volts, middle frame--plate at -8 volts, bottom frame--open. In this case it can be seen that the negatively biased grid excluded some of the electron current which managed to find its way to the E-meter surface in the open (bottom frame) case.

The curves shown in Figure 9 show the effects of changing the potential of the E-meter relative to the plate, the plasma beam, and the grid (reading top to bottom in each set of frames). Horizontal deflection of the oscilloscope in these pictures is proportional to E-meter potential. The calibration is 5 volts/division, zero at center; hence, the photos show the responses of the instrument as its potential is swept through the range $\pm$18 volts.

The parameter which is varied from one picture to another is plasma beam ion current density at the E-meter location. The values are 6.6, 5.0, and 3.3, all times $10^{-9} A/cm^2$ in a, b, and c

respectively; in d the beam was off. The value of beam current density in c corresponds to the plasma density encountered by the SERT I spacecraft at an altitude of a few thousand kilometers. The effect previously mentioned, increased dc offset potential, and displacement of the minimum output signal from the applied field zero, is evident in the top frames of these pictures. (Note that the E-meter was restarted for each picture so that in a the displacement is to the right, in c to the left, etc.) In the middle frames (E-meter exposed to the plasma stream), it is seen that for the first two pictures, a and b, the E-meter output is at its full-scale value for all negative values of E-meter potential. As the E-meter potential goes positive, the output decreases toward a sharp minimum at the plasma potential, then rises steeply as a current of electrons in excess of the ion current is drawn from the beam. The slope of the curve away from the minimum decreases as the current density is reduced. The bottom frames show the effect of excluding electrons from the E-meter (only ions can penetrate the grid because of the +10-volt plasma potential). An interesting feature of these frames is the cut-off of a large fraction of the ion current as the E-meter potential is raised above that of the plasma. Because of the way in which this beam is generated, it is possible for it to contain a large fraction of slow (charge-exchange) ions. It is this component of the ion current which cuts off at the plasma potential. The remaining ion current would not be repelled until the E-meter potential had increased to a point above the net accelerating potential for ions in this beam (about 50V). Another interesting feature of the bottom frames is that in a and b, when the E-meter is above plasma potential, the output signal is constant, whereas in c and d, the low- and zero-density cases, the instrument responds to the field due to the potential difference

between the meter and the grid. This effect is undoubtedly due to shielding of the E-meter from the grid field by the space charge of ions in the meter-to-grid interspace.

VI. PHOTOELECTRIC EFFECTS

In the SERT I space flight the E-meter was exposed periodically to direct illumination from the sun with the possibility that light, particularly ultra-violet radiation, may have affected the response of the E-meter. Photoemission of electrons from the surface of the stator vane of the E-meter may produce a signal mistakenly attributed to an electric field. Electrons from other parts of the meter and nearby surfaces also may possibly reach the stator vane.

Before an electron can escape from a metal surface it must gain a sufficient amount of energy to overcome the surface barrier potential. The electrons in the conduction band are the most energetic and require the least additional energy. The minimum value of the potential barrier is called the work function ϕ. Light quanta absorbed by the surface may provide this additional energy with the emission of electrons provided that $h\nu \geq e\phi$. The work function of most metals is about 4.0V.[2,3] The surface photoelectric emission of electrons increases rapidly from the threshold frequency to a maximum yield at approximately twice the threshold frequency. Surface contamination and impurities as well as the surface structure itself strongly effect photoelectric emission by lowering the work function and increasing the yield. Clean metal surfaces yield of the order 10^{-4} to 10^{-3} electrons for each incident photon.[3] Surfaces contaminated by absorbed gases may have photoelectric yields over ten times greater than a corresponding

carefully cleaned surface. Composite surfaces have photoelectric yields increased by factors up to 100 or more and usually lower threshold frequencies.

In addition to the surface photoelectric effect, there is the volume effect which has a threshold around 9 eV and electron yields roughly 100 times greater than the surface yield. The volume photoelectric effect is important only in the extreme ultra-violet light region for pure metals.

Measurements of the solar radiation above the Earth's atmosphere show that the spectral intensity in the ultra-violet region differs from that of a black body source due to the presence of strong resonance lines.[4,5,6] The Hydrogen Lyman α radiation (1216Å) is the most prominent line in the solar uv spectrum with an intensity of about 2.5×10^{11} photons/cm^2 sec. In this region (1216Å corresponds to 10.2 eV) a clean gold surface may have a photoelectric efficiency of the order of 10^{-2} electrons/photon. This corresponds to a photoelectric current of 4×10^{-10} amp/cm^2 of illuminated surface and would produce a rather large, 0.8 mv/cm^2 signal (through 2×10^6 Ω) at the input of the E-meter amplifier. Unclean surfaces could exhibit initially much stronger signals.

The magnitude and frequency distribution of the solar radiation above the photoelectric threshold indicate the possibility of a strong response to this radiation by the E-meter. Laboratory tests using a hydrogen lamp tend to confirm this expectation. Quantitative results could not be obtained without a source of ultra-violet radiation which reproduces the solar radiation. Such a lamp was not available. In addition, any surface contaminants may greatly increase the photoelectric yield.

This work was supported by NASA Lewis Research Center, Cleveland, Ohio, under Contract NAS3-4114.

REFERENCES

1. Waddel, R. C., "An Electric Field Meter for Use on Airplanes," Rev. Sci. Instr. 19, 31, January, 1948.

2. Maurer, R. J., "Photoelectric effect," Handbook of Physics, edited by E. U. Condon and H. Odishaw (McGraw-Hill Book Company, Inc., 1958), p. 8-66.

3. Weissler, G. L., "Photoionization in gases and photoelectric emission from solids," Encyclopedia of Physics, edited by S. Fluegge (Springer-Verlag, Berlin, 1956), p. 372.

4. Hinteregger, H. E., "Preliminary data on solar extreme ultraviolet radiation in the upper atmosphere," J. Geophys. Res. 66, 2367 (August 1961).

5. Detwiler, C. R., Purcell, J. D., and Tousey, R., "The extreme ultraviolet spectrum of the sun," NRL Report 5608, (U. S. Naval Research Laboratory, July 1961), p. 42.

6. Purcell, J. D., Packer, D. M., and Tousey, R., "The ultraviolet spectrum of the sun," Space Research: Proceedings of the First International Space Science Symposium, edited by H. Kallman Bijl (North-Holland Publishing Company, Amsterdam, 1960), pp. 581-589.